

# **MAGNETORHEOLOGICAL FLUIDS WITH FERROMAGNETIC BINARY ALLOYS AND OXIDES**

*Thesis submitted for the degree of*

**Doctor of Philosophy (Science)**

*in*

**Physics (Experimental)**

*by*

**Md. Injamamul Arief**

Department of Physics

University of Calcutta

December 2015

---

**T**o my parents

## **cknowledgment**

This work was carried out between years 2011-2015 in the Laboratory for Condensed Matter Physics, Department of Condensed Matter Physics and Material Sciences at S. N. Bose National Centre for Basic Sciences, with financial support in the form of JRF/SRF from the Council of Scientific & Industrial Research (CSIR), India.

First of all I would like to thank my supervisor Prof. P. K. Mukhopadhyay for his guidance and mentorship. During my tenure at S. N Bose Centre, he contributed to a rewarding PhD experience by giving me intellectual freedom in my work, supporting my participation at various national and international conferences, engaging me in challenging ideas, and demanding a qualitative contribution in all my endeavors. I am forever indebted to him that he allowed me to proceed to his laboratory during my difficult period. Furthermore, thanks to his continuous effort to accept challenging yet achievable goals while giving me considerable freedom in workspace that made this uphill task possible.

I am thankful to Prof. Indranil Manna, erstwhile Director of Central Glass & Ceramics Research Institute, Kolkata, India for helping us with magnetorheological measurement. We barely started research on field-induced rheological properties at that time and his kind assistance indeed helped us to bolster our effort in understanding the magnetorheological properties better. I also gratefully acknowledge Prof. R. V. Upadhyay, Principal of P. D. Patel Institute of Applied Sciences, CHARUSAT, Gujarat for helping us with magnetorheological measurements and valuable suggestion during my visit. My thankful acknowledgment also goes to Ms. Rasmita Sahoo and Dr. Surajit Dhara of School of Physics, Central University of Hyderabad, India for assisting us with various magnetorheological measurements.

I would like to thank S. N. Bose National Centre for Basic Sciences for providing the research fellowship during my period of extension and facilities. I would also like to thank Department of Science and Technology (DST) for providing me financial support

during my visit to 13<sup>th</sup> International Conference on Electrorheological Fluids & Magnetorheological Suspensions (ERMR-2014) held in Granada, Spain.

I would like to extend my thanks and appreciation to all the members of the LCMP with whom I had the opportunity to work. First of all, I am thankful to our senior colleague Dr. Sandeep Aggarwal, who helped me during the manuscript preparation. I am also grateful to the LCMP members and colleagues Tanmoy Ghosh, Md. Sarowar Hossain, Dipanjan Samanta, Dr. B. Rajini Kanth and Abhishek Bagchi for providing a friendly and cooperative atmosphere at work and also useful feedback on my work.

I am grateful to all the friends and well wishers I have met along the way and have contributed to the development of my research. I would never forget all the chats and beautiful moments I shared with some of them. I extend gratitude to my best friend and former colleague Urbashi for her continuous support and enthusiasm during my tenure at SNB. I would also like to thank Rabeya, Rishi, Samik and Pratik for their cooperation and encouragement during these stressful and critical moments.

Needless to say, this entire exercise would be at most a dream if it was not for my family. My parents and sister have been a great source of encouragement during all these years. They have always been supportive of my academic endeavors and proved yet again this time, with unflagging love and invaluable emotional support.



Md. Injamamul Arief

Salt Lake, Kolkata

December 2015.

# List of publications

---

1. Fabrication and viscoelastic properties of PVC-coated magnetite agglomerates in magneto-rheological suspension, Injamamul Arief et al. *Magneto hydrodynamics*, **49** (2013), No. 3-4, 479–483.
2. Preparation of spherical and cubic  $\text{Fe}_{55}\text{Co}_{45}$  microstructures for studying the role of particle morphology in Magnetorheological suspensions, Injamamul Arief et al. *Journal of Magnetism and Magnetic Materials*, **60** (2014) 104–108.
3. Synthesis of dimorphic MR fluid containing NiCo nanoflowers by polymer assisted polyol method and study of its magnetorheological properties, Injamamul Arief et al. *Physica B*, **448** (2014), 73–76.
4. Amphiphilic triblock copolymer-assisted synthesis of hierarchic NiCo nanoflowers by homogeneous nucleation in liquid polyols, Injamamul Arief et al. *Journal of Magnetism and Magnetic Materials*, **372** (2014), 214–223.
5. Dynamic and rate-dependent yielding behavior of  $\text{Co}_{0.9}\text{Ni}_{0.1}$  microcluster based magnetorheological fluids, Injamamul Arief et al. (*Journal of Magnetism and Magnetic Materials*, **397** (2016) 57–63).
6. Steady shear magnetorheology in  $\text{Co}_{0.9}\text{Ni}_{0.1}$  microcluster-based MR fluids at elevated temperatures, Injamamul Arief et al. (Submitted).
7. Magnetorheological Payne effect in bidisperse MR fluids containing Fe-nanorods and  $\text{Fe}_3\text{O}_4$  nanospheres: a dynamic rheological study, Injamamul Arief et al. (Submitted).
8. Two-step yielding in novel CoNi nanoplatelet-based magnetic fluids under oscillatory rheology, Injamamul Arief et al. (Submitted).

# List of Abbreviations/nomenclature

MR, MRF	Magnetorheological, magnetorheological fluid
MVE	Magnetoviscous effect
$R_e, M_n, P_e$	Reynold's number, Mason number, Peclet number
$\eta_r, \eta_s$	Relative apparent viscosity, suspension viscosity
$\phi, \phi_m$	Volume fraction, maximum volume fraction
$k_B$	Boltzmann constant
$\mu_0$	Permeability of vacuum
$\tau, \tau_y$	Shear stress, yield stress
$\tau_{ys}$	Static yield stress
$\tau_{yd}$	Dynamic yield stress
$\gamma, \dot{\gamma}$	Shear strain, shear strain rate
PVC	Poly-vinylchloride
CTAB	Cetyl-trimethylammoniumbromide
PAA	Poly-acrylic acid
EG, PrG, TEG, PEG	Ethylene glycol, Propylene glycol, Tetraethylene glycol, polyethylene glycol
FESEM	Field emission scanning electron microscope
EDAX	energy dispersive x-ray analysis
fcc, hcp	Face-centred cubic, hexagonal close-packing
bcc	Body-centred cubic
XRD	X-ray diffraction
FWHM	Full-width-half-maxima
ICDD	International Centre for Diffraction data
JCPDS	Joint Committee on Powder Diffraction Standards
DSC	differential scanning calorimeter
VSM	Vibrating sample magnetometer
H	Magnetic field intensity
M	Magnetization
$M_s$	Saturation magnetization
$H_c$	Coercive field
$M_r$	Remnant magnetization
M-H	Isothermal magnetization as a function of field

ZFC	Zero-field-cooled
FC	Field-cooled
TEM	Transmission electron microscopy
HRTEM	High-resolution transmission electron microscopy
HAADF	High angle annular dark field
FFT	Fast-Fourier transform
SAED	Selected area diffraction
EELS	Energy electron loss spectroscopy
$G'$ , $G''$	Storage modulus, loss modulus
CSR	Controlled Shear rate
CSS	Controlled Shear Stress
$\tan \delta$	Loss factor
LVE, LVR	Linear viscoelastic, linear viscoelastic regime
SAOS	Small angle oscillatory strain
LAOS	Large angle oscillatory strain
$\gamma_c$ , $\gamma_{cr}$	Critical strain amplitude, cross-over strain

## Table of Content

<b>Acknowledgment.....</b>	<b>i</b>
<b>List of publications.....</b>	<b>iii</b>
<b>List of Abbreviations .....</b>	<b>iv</b>
<b>Table of Content.....</b>	<b>vi</b>
<b>Chapter 1 Introduction.....</b>	<b>1</b>
1.1 Overview .....	2
1.2 Magnetorheological fluids .....	2
1.3 Magnetic properties of dispersed phase particles .....	5
1.4 Magnetic particles for MR fluids .....	7
1.5 Rheological properties of fluid systems .....	8
1.6 Motivation of the thesis .....	10
<b>Chapter 2 Fundamentals of rheology and magnetorheology.....</b>	<b>13</b>
2.1 Flow properties of suspensions under simple shear.....	14
2.2 Volume fraction and shape & size dependence of particles on viscosity .....	15
2.3 Linear viscoelasticity .....	19
2.3.1 Steady shear.....	19
2.3.2 Dynamic measurements.....	21
2.4 Rheology of magnetorheological (MR) fluids .....	22
<b>Chapter 3 Experimental procedures.....</b>	<b>26</b>
3.1 Synthesis of alloyed nano/microparticles of Fe, Co and Ni .....	27
3.1.1 Synthesis of Fe <sub>55</sub> Co <sub>45</sub> microparticles by borohydride reduction .....	27
3.1.2 Synthesis of Ni <sub>x</sub> Co <sub>1-x</sub> micro- and nanoparticles by polyol reduction.....	28
3.1.2.1 Ni <sub>x</sub> Co <sub>1-x</sub> flower like microstructures.....	28
3.1.2.2 Ni <sub>0.1</sub> Co <sub>0.9</sub> microcluster.....	29
3.1.2.3 NiCo nanoplatelets .....	30
3.1.3 Synthesis of Fe <sub>3</sub> Ni microstructures by hydrazine reduction.....	30
3.2 Synthesis of Fe <sub>3</sub> O <sub>4</sub> and Fe microparticles .....	30
3.2.1 Fe <sub>3</sub> O <sub>4</sub> microsphere by thermal decomposition of organometallic precursor ..	30
3.2.2 PVC-Fe <sub>3</sub> O <sub>4</sub> agglomerate by coprecipitation method .....	31
3.2.3 Iron (Fe) microrod by hydrothermal reduction .....	31
3.3 Characterization .....	32
3.3.1 X-Ray Diffraction .....	32
3.3.2 Scanning electron microscopy & Energy dispersive x-ray analysis .....	33
3.3.3 Transmission electron microscopy (TEM).....	35
3.3.4 Vibrating sample magnetometer (VSM).....	39
3.4 Magnetorheometry.....	40
<b>Chapter 4 Investigations on Fe<sub>55</sub>Co<sub>45</sub>-based fluids: structure and magneto-</b>	
<b>rheology.....</b>	<b>43</b>
4.1 Introduction .....	44
4.2 Results and discussions.....	44

4.2.1 Morphological characterization of dry powder .....	44
4.2.1.1 SEM and EDAX .....	44
4.2.1.2 TEM .....	46
4.2.1.3 X-ray diffraction .....	47
4.2.2 Structure and growth mechanism .....	48
4.2.3 Magnetization studies .....	51
4.2.4 Magnetorheological characterization .....	52
4.2.4.1 Preparation of MR fluids .....	52
4.2.4.2 Steady shear magnetorheology: particle shape and size dependence .....	52
4.2.4.3 Sedimentation stability of MR fluids .....	57
4.3 Conclusions .....	58
<b>Chapter 5 NiCo nanoflowers and nanoplatelets: structure, morphology and rheology .....</b>	<b>59</b>
5.1 Introduction .....	60
5.2 Structure and morphology of particles .....	61
5.2.1 SEM and TEM studies .....	61
5.2.1.1 Ni <sub>x</sub> Co <sub>1-x</sub> flower-like microparticles .....	61
5.2.1.2 NiCo nanoplatelets .....	63
5.2.2 X-ray diffraction studies of NiCo nanoflowers and nanoplatelets .....	65
5.2.3 Evolution of particles: growth mechanism .....	67
5.2.3.1 NiCo hierarchical nanostructures .....	67
5.2.3.2 NiCo nanoplatelets .....	74
5.2.4 Magnetic characterization .....	75
5.3 Magnetorheological studies .....	79
5.3.1 NiCo-flower based MR fluids: role of ferrofluid in MR effect .....	79
5.3.2 Magnetorheology in NiCo nanoplatelet-based suspensions .....	80
5.3.2.1 Oscillatory magnetorheology: strain-thickening in loss modulus .....	80
5.4 Conclusion .....	82
<b>Chapter 6 Structure and magnetorheology in NiCo microcluster based systems .....</b>	<b>84</b>
6.1 Introduction .....	85
6.2 Structure and morphology of microclusters .....	85
6.2.1 SEM and TEM studies on Ni <sub>0.1</sub> Co <sub>0.9</sub> microclusters .....	85
6.2.2 X-ray diffraction studies of NiCo microclusters .....	86
6.2.3 Magnetic characterization .....	87
6.3 Magnetorheological studies .....	88
6.3.1 Ni <sub>0.1</sub> Co <sub>0.9</sub> microcluster-based MR fluids .....	88
6.3.1.1 Role of particle conc. in steady shear and magnetoviscous effect .....	89
6.3.1.2 Magnetosweep measurement and field-dependent relaxation .....	91
6.3.1.3 Static and dynamic yield stress .....	92
6.3.1.4 Oscillatory magnetorheology .....	95
6.3.1.5 Temperature-dependent magnetorheology: introduction to scaling parameters .....	97
6.4 Conclusion .....	106

<b>Chapter 7 Investigations on Fe<sub>3</sub>Ni based fluid systems: structure, morphology and magnetorheology .....</b>	<b>107</b>
7.1 Introduction .....	108
7.2 Structure and morphology of particles .....	109
7.2.1 SEM, x-ray diffraction studies and VSM.....	109
7.3 Magnetorheological studies .....	111
7.3.1 Steady shear magnetorheology in PAA-Fe <sub>3</sub> Ni based fluid.....	112
7.3.2 Temperature-dependent oscillatory rheological studies .....	114
7.4 Conclusion.....	115
<b>Chapter 8 Investigations on Fe<sub>3</sub>O<sub>4</sub>-based MR fluids.....</b>	<b>117</b>
8.1 Introduction .....	118
8.2 Structure and morphology of particles .....	119
8.2.1 SEM and TEM studies .....	119
8.2.2 FTIR spectra .....	120
8.2.3 X-ray diffraction.....	121
8.2.4 Magnetic characterization.....	122
8.3 Magnetorheological studies .....	123
8.3.1 Magnetorheology in PVC-Fe <sub>3</sub> O <sub>4</sub> based MR fluids.....	123
8.3.2 Magnetorheological Payne effect in Fe-microrod containing MR fluids.....	126
8.4 Conclusion.....	132
<b>Chapter 9 Summary and Conclusion.....</b>	<b>133</b>
9.1 Summary .....	134
9.2 Future works.....	137
<b>Bibliography .....</b>	<b>138</b>

# 1

## **Chapter 1**

### **Introduction**

*In this chapter we introduce the topic and give the motivation for the work undertaken in the thesis. We provide a literature survey for the background.*

## **1.1 Overview**

The rapid evolution of smart or intelligent material systems over conventional materials is consistent with the progress in science and technology. A smart material is a functional material whose properties can be significantly and reversibly changed by external stimuli such as temperature, pressure, electric field, magnetic field, light etc. The advantage of smart materials over conventional materials is that in addition to usual properties (mechanical, thermal, electrical, magnetic), they display additional functional capabilities (sensing, actuating) in controlled fashion. The degree of smartness or intelligence of these materials is expressed in terms of the large amplitude changes in properties in response to the external stimuli and fast response time. The application of these materials can largely be found in sensing and actuating devices. Sensors are classified as the materials that respond to external physical stimuli (temperature, pressure, illumination) and transmit resulting signal for monitoring and operating purpose. An actuator, on the other hand, responds to stimulus in the form of change in mechanical properties, such as change in viscosity or dimension. One of the finest examples of these materials includes magnetorheological fluids where external magnetic field directly couples with the change in mechanical properties, i.e. field-induced viscosity. Fast response and large amplitude change in mechanical stress are the main advantages of these materials.

## **1.2 Magnetorheological fluids**

Since the discovery by Rabinow (1949), magnetorheological (MR) fluids have gained considerable interest in terms of their field-dependent rheological properties and widespread application [1,2]. MR fluids are suspensions of magnetically soft particles with supra-colloidal dimension ( $0.1-10\mu m$ ) in organic or mineral carrier fluids. The advantages of using these MR fluids over conventional materials are associated with the ability to achieve wide range of magnetic field-induced viscosity of up to several orders of magnitude almost instantaneously (in a few milliseconds) [3]. This unique feature of MR fluids provides an efficient way to control force or torque transmission applications that has already been utilized in far-ranging engineering and robotics applications such as automotive suspension, high precision MR polishing and finishing, prosthetic legs and

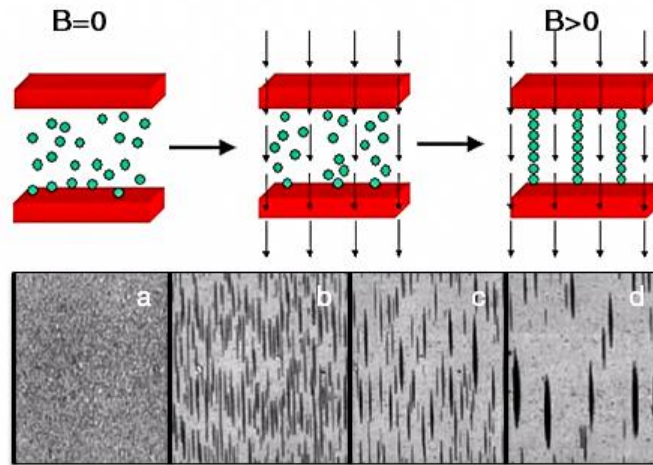


**Figure 1.1** At the top, schematic illustration of the behavior of an MR fluid under magnetic field (©Innovent Technologieentwicklung, Jena). For a dilute MR fluid, optical microscope images (a-d) of field-induced structures at various intervals are shown at bottom.

haptic devices, automotive clutch, actively-controlled damper for cable bridge suspension, helicopter rotor, automated seat suspension, oil and gas drill bits, vibration controller in washing machine etc [4-9] to name a few. The basic phenomenon in magnetorheology is to form the transient, field-dependent chain-like aggregates in biphasic fluids, owing to the change in flow behavior [10-12]. The field-induced structuration in an MR fluid is illustrated schematically in Fig. 1.1. The structural evolution in presence of magnetic field in a dilute MR fluid is explored with the help of optical microscope images taken at various time intervals (Fig. 1.1). In absence of hydrodynamic forces originating from bulk flow field, the microstructures formed mostly due to magnetostatic forces. Flow is possible only when the percolated aggregates started breaking under shear forces. In the ‘off-state’ when there is no applied magnetic field, MR fluids behave like a liquid with insignificant apparent viscosity (0.1-1 *Pa.s* at low shear rate) [13]. However, magnetic field polarizes the dispersed magnetic phase within milliseconds and thus viscosity rapidly changes. This is a completely reversible process, i.e. upon removal of field, liquid-like behavior prevails. Macroscopically speaking, the solid-like elastic behavior of MR fluids under magnetic field can be retained up to a critical shear stress, beyond which materials flow is initiated [14]. This critical stress is defined as yield stress,  $\tau_y(H)$  where  $H$  is the magnitude of local field strength. When

yield stress is exceeded, materials start flowing. The strength of MR fluid can also be expressed in terms of magneto-viscous effect or MR effect, defined as change in shear viscosity at a prescribed magnetic field and shear rate, in comparison to its zero field viscosity [15]:

$$MR \text{ effect} = \frac{\eta(H, \dot{\gamma}) - \eta(H = 0, \dot{\gamma})}{\eta(H = 0, \dot{\gamma})} \quad (1.1)$$

Where  $\eta(H, \dot{\gamma})$  and  $\eta(H = 0, \dot{\gamma})$  are the constant shear rate ( $\dot{\gamma}$ ) viscosities of MR fluid at a specified magnetic field and zero magnetic field, respectively. The relative increment of MR effect can also be studied quantitatively by Mason number ( $Mn$ ). It is defined as the ratio of magnetic to viscous forces [16]:

$$Mn = \frac{36\eta_0\dot{\gamma}}{\mu_0 M_p^2} \quad (1.2)$$

where  $\eta_0$ ,  $\dot{\gamma}$ ,  $\mu_0$  and  $M_p$  are the suspension viscosity, shear rate, vacuum permeability and particle magnetization, respectively. The impact of inertia is governed by particle's Reynold's number and defined as,

$$Re = \frac{\rho_0 a^2 \dot{\gamma}}{\mu_0} \quad (1.3)$$

where  $\rho_0$ ,  $a$ ,  $\dot{\gamma}$  and  $\mu_0$  are the density of carrier fluid, particle radius, shear rate and vacuum permeability, respectively. Since Reynold's number in a suspension of average micron-sized particles is normally low ( $Re \approx 10^{-1} - 10^{-2}$ ) at low shear rates, viscous force on a particle can be estimated by Stoke's drag on a sphere:  $f_d = 6\pi\eta a^2 \dot{\gamma}$  (1.4) where,  $\eta$ ,  $a$  and  $\dot{\gamma}$  are viscosity at high shear rate, radius of particle and shear rate, respectively. Another dimensionless parameter can be expressed as the ratio of magnetic to Brownian forces [17]:

$$\lambda = \frac{\pi\mu_0 a^3 M_p^2}{6k_B T} \quad (1.5)$$

Where,  $k_B$  is Boltzmann constant ( $1.38 \times 10^{-23}$ J/sec) and T is absolute temperature. It is evident that magnetic forces dominate well over Brownian energy even at elevated temperature at which typical MR devices are operating [17].

Particle size, shape, density, particle size distribution, saturation magnetization and coercive field are important factors that affect MR fluid's performance, i.e. apparent yield

stress and MR effect. In addition to magnetic disperse phase, carrier fluids, surfactants and anticorrosion additives are important factors that affect the rheological properties, stability and redispersibility of the MR fluid.

### **1.3 Magnetic properties of dispersed phase particles**

Magnetization in materials arises due to orbital and spinning motion of electrons. However, magnetic moments in an atom are distributed in such a way that either there is a cancellation of individual moments giving rise to no net magnetization or, atom acquires magnetization due to partial cancellation of moments. For a diamagnetic material, susceptibility is negative owing to the fact that sole contribution comes from orbital electronic motion but there is no net magnetic moment residing on each atom. For paramagnetic materials, although each atom carries moment but due to thermal energy, the net magnetization is zero in the absence of external magnetic field. However, the susceptibility is slightly positive and follows the familiar Curie-Weiss law. The magnetization in ferromagnetic materials is caused by the unfilled 3d/4d/4f orbitals. The dipoles can be aligned by an applied magnetic field. The theory of ferromagnetism was first postulated by Weiss [18]. His hypothesis was based on two assumptions: a) spontaneous magnetization, b) domain magnetization. A ferromagnetic material in the demagnetized state is composed of a number of small regions known as domains. Each domain is spontaneously magnetized but the direction of magnetization is such that the total moment is zero due to cancellation, resulting in no net magnetization. Upon the application of the magnetic field, the domains with the magnetization parallel to the applied field grow while the sizes of other domains not parallel to the field shrink. In antiferromagnetic substances, there are also unquenched magnetic moments but these moments align in regular pattern with neighboring directions pointing opposite, giving rise to no net magnetization in the absence of temperature fluctuations. Ferrimagnetic materials are a subset of antiferromagnetic materials where incomplete cancellation due to unequal moments gives rise to non-zero net magnetic moment.

The magnetic interaction of two particles carrying magnetic moments can be expressed as [18],

$$U_{int.} = \frac{-m^2}{4\pi\mu_0 a^3} (3\cos^2\theta - 1) \quad (1.6)$$

Where  $a$  is interparticle distance,  $\mu_0$  is permeability of free space ( $4\pi \times 10^{-7} H/m$ ),  $m$  is magnetic dipole moment and  $\theta$  is angle between the magnetic dipole moment direction and interparticle distance (Fig. 1.2). When particles are in contact, attractive energy predominates and  $\theta = 0$ :

$$U_{int.}^{minimum} = \frac{-m^2}{2\pi\mu_0 a^3} \quad (1.7)$$

In this case, interparticle distance is the diameter of magnetic sphere.

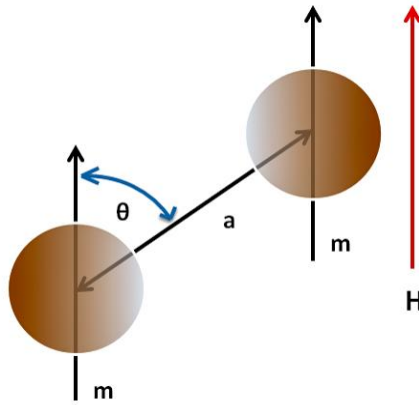


**Figure 1.2** Schematic illustration of magnetic dipole-dipole interaction energy

In magnetization measurement, when magnetic field is reduced to zero from higher magnetic field, magnetization of materials generally reduces to a non-zero value known as remnant magnetization ( $M_r$ ) or remanence. When the field direction is reversed, magnetization will first reach to zero and then decrease. The field corresponds to this zero magnetization is known as coercivity ( $H_c$ ). Therefore, coercivity is the resistance of a material to magnetization reversal. Coercivity and remanence are microstructure sensitive property and are used to determine whether a material is magnetically soft or hard. Usually magnetic material with  $H_c \leq 50 Oe$  are termed as magnetically ‘soft’ and for  $H_c \geq 100 Oe$ , it is regarded as ‘hard’ [19]. Coercivity is a function of magnetic saturation ( $M_s$ ) and anisotropy constant ( $K_1$ ),  $H_c = 2K_1/M_s$  (neglecting demagnetizing correction) [20]. With increasing particle size, coercivity generally decreases. Therefore,  $H_c$  in multidomain particles are smaller than that of single domain as for the former,

rotation of magnetic moments is easier due to domain wall motion. As the particle size is decreased,  $H_c$  goes through a maximum and then decreases to zero. In such a case of zero coercivity, these particles are called superparamagnetic. Due to structural imperfections like crystal defects because of atomic impurity, domain walls can get pinned and hinder the movement of domain boundaries. This increases the coercivity of the material. In addition to low coercivity, higher saturation magnetization and permeability, smaller remanence, narrower hysteresis loop are other characteristics of soft magnetic materials. On the other hand, hard magnetic materials have high coercive field and remanence, large hysteresis loop, and high magnetic permeability.

#### **1.4 Magnetic particles for MR fluids**

For preparation of MR fluids, particles with low coercivity and high saturation magnetization are preferred. Low coercivity ensures that as soon as the magnetic field is taken off, MR fluids return to its demagnetized state in milliseconds. High saturation magnetization is desired in terms of wide range of magnetic field operability. Due to their favorable properties, carbonyl iron particles (CIP) are the most commonly used disperse phase in commercial MR fluids [21]. Mesoscale CIP particles are synthesized by decomposition of iron pentacarbonyl precursor and are roughly spherical. This results in reduced shape anisotropy. Higher purity of samples also ensures reduced mechanical hardness in materials which arises due to resistance to dislocation motion [21]. For MR applications, particles of non-abrasive nature are preferred.

While most of the conventional and commercially available MR fluids utilize CIP and magnetite ( $\text{Fe}_3\text{O}_4$ ), search for alternative magnetic particles in terms of enhanced MR effect and improved stability is also on. Binary ferromagnetic alloys of Fe, Co and Ni are expected to be the excellent materials for MR applications due to their magnetic softness and high saturation magnetization. Fe-Co alloys (composition 1:1) have a saturation magnetization of  $\sim 2.43$  T [22]. The higher density of FeCo, NiCo and FeNi particles, however, can aggravate settling problems. This can be controlled by tuning shape and sizes of these particles in wet-chemistry. Alloys of Fe, Co, Ni are synthesized here by chemical reduction methods and therefore, their properties (magnetic, surface morphology, shape and size) can be accurately tuned in order to get the desired features.

Contrary to conventional magnetic materials like CIP or oxides, alloys of FeCo and FeNi can display significant increase in yield stress and MR effect. High degree of shape anisotropy can also affect MR properties. It was previously shown that field-induced solid-friction in suspensions of rod-like particles produces stronger MR response compared to that of spherical particle-containing suspensions [23]. MR fluids have also been prepared based on ferrimagnetic materials such as ferrite materials of Fe, Ni, Co and Zn. However, the saturation magnetization of spinel ferrites is relatively low (~0.4-0.6 T) and therefore the yield stresses also tend to be smaller [19]. Fe<sub>3</sub>O<sub>4</sub> is widely used in commercial magnetic fluids. For maximum yield stress and sedimentation stability, Fe<sub>3</sub>O<sub>4</sub>-based ferrofluid itself can serve as carrier fluid. The smaller magnetite nanoparticles act as cementing materials in between aggregates of larger magnetic particles under magnetic field, thereby enhancing MR strength [24].

## **1.5 Rheological properties of fluid systems**

Rheology is the study of the flow behavior of materials and the response of materials to applied external stress. The rheological properties of suspension, colloidal dispersion and emulsion are measured by a rheometer which provides critical information about the material properties (stress, shear viscosity, viscous relaxation etc.) that are often deemed crucial in many industrial applications. The rheological fluids are complex formulation of carrier fluids and suspended particles of varying sizes, shapes, compositions and various additives that affect stability. The factors that affect the rheological properties of fluid systems are hydrodynamic forces, Brownian motion, strength of the interparticle interaction, volume fraction of disperse phase, electrostatic forces, size and shape of particles, magnetic properties of particles, gravitational force and steric repulsion. Measuring the rheology of a system provides valuable information of the microstructure properties of the colloidal or suspension states and the interactions that originate from this assembly. Rheological parameters derived from measurements can be utilized to determine the flow behavior of non-Newtonian materials, viscoelasticity as a function of time, the degree of stability of structuration at rest or on shear, and zero shear viscosity or the maximum viscosity of the fluid.

An MR fluid is a field-responsive biphasic fluid system that demonstrates significant increase in viscosity and shear stress upon application of external magnetic field. The complex aggregated network can withstand the stress up to a limit beyond which rupture of aggregated network takes place. Rheology of MR fluids is concerned with the dependence of shear stress with shear strain or rate of shear. It is described schematically by considering 3D rectangular element of fluid in the Fig. 1.3. When a shear force  $F$  applied to the top area, the shear stress is determined by force per unit area, i.e.

$$\text{Shear stress, } \tau = \frac{F}{\text{Area}} = \frac{F}{\delta_x \times \delta_z} \quad (1.8)$$

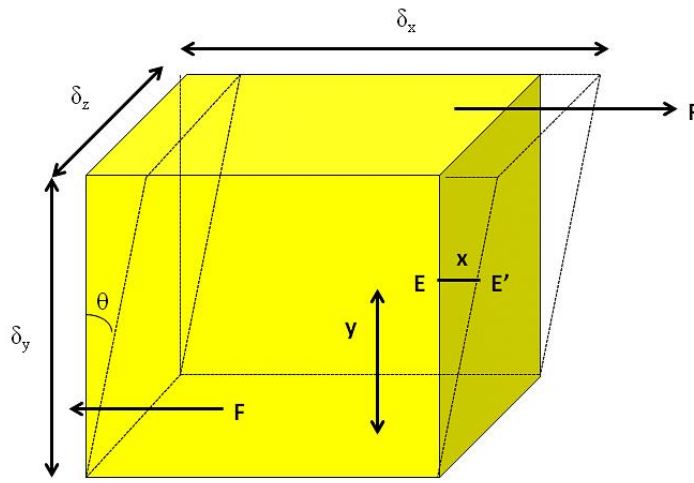


**Figure 1.3** Schematic of the effect of shear force on a material in fluid system

Shear strain is the deformation of the material and is measured by the angle  $\theta$ . For solids, strain is proportional to stress. For fluids, strain increases with increasing stress. According to the schematic, strain is given for a particle from point E to E' as  $\theta = \frac{x}{y}$  (for small deformation). Therefore, strain rate is  $\dot{\gamma} = \frac{x}{yt} = \frac{u}{y}$  where u is the velocity ( $x/t$ ). Since shear stress is proportional to strain rate, we get

$$\tau = \text{Const.} \times \frac{u}{y} \quad (1.9)$$

The proportionality constant is termed as dynamic viscosity  $\eta$ . The term  $\frac{u}{y}$  is the change in velocity with y, and is known as velocity gradient. It can be expressed in differential form, giving

$$\tau = \eta \frac{du}{dy} \quad (1.10)$$

This is known as Newton's law of viscosity.

There are many factors that influence the rheological properties of MR fluids such as volume fraction of fluids, density of dispersed phases, particle size and shape distribution, viscosity and thermal properties of the carrier fluid, additives and stabilizers, strength of applied magnetic field and temperature. The inter-relationships of all these factors are crucial in establishing structure-dynamics correlation to improve efficiency for custom applications. An MR fluid should possess low off-state viscosity that can produce high yield stress in presence of the external magnetic field. The details of fundamentals of rheology and magnetorheology are discussed in chapter 2.

## **1.6 Motivation of the thesis**

Since the discovery, controllable mechanical properties of MR fluids have created a lot of interesting applications in torque transmission and vibration control devices. For these applications, rheological properties of fluids and working mode of the device are crucial parameters. For all 'state-of-the-art' applications, most important features of a good MR fluid are to have high 'turn up' ratio (yield stress output), durability, chemical and temperature stability. The use of MR fluids is found out in more and more new devices, in addition to the traditional uses for the last three decades. However, they still do not satisfy all the diverse and stringent commercial requirements. The response, despite being quick (milliseconds), is restricted by number of factors. The maximum MR effect is a function of saturation magnetization of disperse phase. Additionally magnetic phase exhibits remanence, therefore, system is magnetized slightly even after field is removed. This reduces the typical relaxation time of MR fluids and limits the usage. Furthermore, bulk density of magnetic phase is significantly higher than carrier fluid. This is associated to sedimentation problem in conventional MR fluids. To address the difficulties described, material science oriented approach, i.e. surface chemistry and polymer physics is followed to synthesize stable and redispersible MR fluids with desired stress outputs.

As discussed in section 1.4, ferromagnetic carbonyl iron particles are normally used in magnetic suspensions for their higher magnetic saturation, permeability and monodispersity. In contrast to conventional carbonyl iron particles (CIP), ferromagnetic

binary alloys provide a better alternative for their higher saturation magnetizations, low coercivity and remanence and excellent control of shapes and sizes. In the last few years, a great deal of researches has been published on ferromagnetic carbonyl iron and surface enhanced iron oxide particle-based MR fluids. However, a thorough and organized approach to study field-dependent rheology of MR fluids containing binary ferromagnetic alloys with wider range of particle shapes and sizes has not been done. The high magnetic saturation and permeability, low coercivity and remanence of binary ferromagnetic alloys of Fe, Ni and Co make them a suitable choice for MR fluidic applications. This thesis focuses on this important aspect of binary metallic alloy nano-/microstructures that MR fluidic systems containing the bimetallic alloys of Co, Ni and Fe are the most promising alternative to that of the CIP-based fluids.

The important factors that affect magnetorheology are particle volume fraction, shape and interactions between particles, spatial arrangement of particles and nature of bulk flow [25]. Most researches had concentrated on suspensions of spherical particles, however, particle anisometry offers several additional effects, notably: (a) local flow around a non-spherical particle is different than that around a spherical one, therefore, contribution of non-spherical particles to viscosity and stress parameters is also different, (b) non-spherical particles are orientable and the contribution also depends on their orientation in suspension upon shearing and (c) inter-particle interaction among the anisotropic particles are higher than that of spherical particles, owing to stronger field-induced chain-like structuration. The present thesis also looks critically at the role of shape anisotropy of dispersed magnetic phase in MR suspensions. Furthermore, an MR fluid in a device dissipates energy in the form of heat during use and therefore, increases the temperature [26]. So, operability of MR fluids at elevated temperature is crucial to predict the effect of temperature on the MR effect and the mechanisms that influence the outcome. While most of the publications concentrate on enhancement of material properties and yield stress, very few of them actually deal with temperature-dependence of MR fluids. We investigate the mechanisms that govern non-equilibrium size distribution of internal chain structures with increasing temperature. We also deduce experimental scaling parameters to correlate magnetic field and temperature-dependent shear properties. Scaling laws are

introduced to rationalize the experimental observations, the dependence of one physical parameter to multiple variables or factors, therefore, provide a useful insight to the internal mechanism that governs interactions within the magnetorheological fluids.

The dissertation is organized as follows: chapter 1 is a general description of the research background and literature review concerning the magnetic materials, magnetorheological fluids and stability of MR fluids. The research motivations and objectives of thesis work are also stated. In chapter 2, some important fundamental aspects of fluid mechanics, rheology and magnetorheology are discussed. Chapter 3 describes the wet-chemical synthesis and characterizations of nano and microstructures of binary alloys and oxides and under variable reaction condition. Chapter 4, 5 and 6 describe the detailed structural and morphological characterization of FeCo, NiCo and FeNi nano and microstructures. The MR studies of the suspensions based on the alloyed microstructure-based MR fluids are also performed under transient shear and oscillatory rheometry. In addition to room temperature, MR responses at elevated temperatures are also thoroughly discussed. Chapter 7 focuses on structure and morphology of Fe-oxides anisometric particles. The magnetorheology of Fe-oxide based MR fluids and structure-dynamic correlation is also established. In chapter 8, we summarize all the findings and conclude. We also discuss some of the areas where further research work can also be performed.

# 2

## Chapter 2

### **Fundamentals of rheology and magnetorheology**

*In this chapter, important fundamental aspects of fluid mechanics and rheology were discussed. We looked at stress-strain rate relationships for simple shear flows of viscoelastic fluids. The description of the complex flows was extended to magnetorheological suspensions. Furthermore, the fluid behavior was modeled and explained using the analytical and phenomenological equations.*

## 2.1 Flow properties of suspensions under simple shear

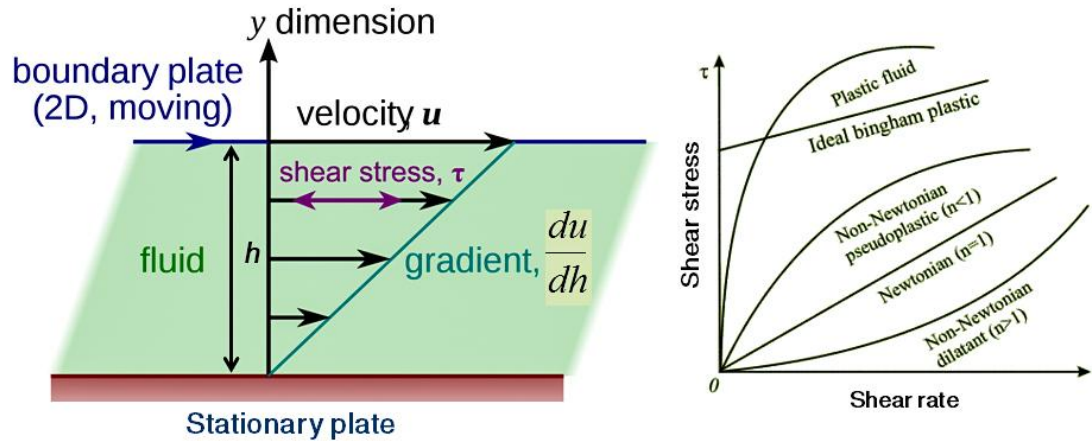


**Figure 2.1** The linear velocity profile in a flowing Newtonian fluid under simple shear. On the right, shear stress vs. shear rate profiles for Newtonian and non-Newtonian fluids.

Rheology is the study of flow and deformation of fluids. The first notion of viscosity of a fluid was defined by Newton's equation as a constant of proportionality between the shear stress ( $\tau = F/A$ ) and resulting velocity gradient perpendicular to the flow direction. According to generalized Newton's law, velocity gradient is shear rate so that  $\tau = \eta \dot{\gamma}$  where,  $\eta$  is viscosity coefficient and  $\dot{\gamma} (= v/h)$  is shear rate. Here  $A$  is the surface area of the sheared fluid volume on which the shearing force  $F$  is acting and  $h$  is the height of the volume element over which the fluid layer velocity  $v$  varies from its minimum to maximum value (Fig. 2.1). Newtonian behavior is characterized by time-independent flow and instantaneous relaxation of shear stress upon cessation of shear rate. However, deviation from linear to nonlinear time-dependent behavior is evident when flow history of a fluid is taken into account. For most of the suspensions and polymer melts, non-Newtonian behavior is observed in which apparent viscosity is either decreasing or increasing with rate of shear, giving rise to shear-thinning or shear-thickening behavior, respectively. Shear thinning properties arise primarily due to the breakdown of the flocculated structures, loss of junctions in polymer solution, rearrangement of microstructures in suspensions and alignment of rod-like particles in the flow directions [27]. On the other hand, temporary aggregation of particles due to strong interparticle interaction gives rise to shear thickening behavior [28]. In both cases, the behavior is reversible, i.e. materials revert to its pre-shear state when the stress is removed. In non-

Newtonian fluids, the relationship between shear stress ( $\tau$ ) and shear rate ( $\dot{\gamma}$ ) is often expressed in terms of a power-law Ostwald-de Waele model:  $\tau = K\dot{\gamma}^n$  (2.1) where  $K$  is consistency index (viscosity) and  $n$  is power-law exponent, indicating the extent of deviation from Newtonian behavior ( $n = 1$ ). For  $n > 1$ , system is shear-thickening and  $n < 1$ , it behaves as shear-thinning [29]. For example, most of the biological systems as well as magnetic suspensions show shear thinning behavior, i.e. doubling the shear stress will yield more than double the shear rate, therefore, easier to induce strain at high shear rates. For aqueous silica suspensions, shear thickening behavior is reported beyond a critical particle volume fraction ( $\phi \geq 0.3$ ) and shear rate ( $\dot{\gamma} \sim 10^3 \text{ s}^{-1}$ ) [29]. At equilibrium, system is stationary due to inertia. With increasing shear rate, particle association becomes more organized along the force field, therefore, hinders the flow. At very high shear rate, hydrodynamic interactions dominate over stochastic ones, giving rise to transient fluctuation in particle concentrations. The hindered flow of particles around each other at high shear rate accounts for the higher rate of energy dissipation. This gives rise to stronger viscosity [29].

## 2.2 Volume fraction and shape & size dependence of particles on viscosity

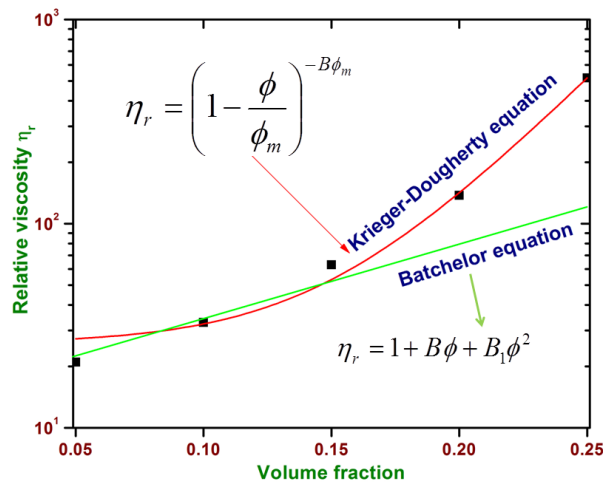


**Figure 2.2** Relative viscosity ( $\eta_r$ ) vs. particle volume fraction curve is shown for MR fluids containing  $\text{Fe}_3\text{O}_4$  agglomerates. The Krieger-Dougherty and Batchelor fits are also illustrated.

A rheological suspension consists of randomly distributed particles in a matrix fluid. In order to establish the relationship between relative viscosity ( $\eta_r$ ) and particle volume fraction ( $\phi$ ), Rutgers defined three regimes of  $\eta_r(\phi)$  [30]: (i) dilute regime for  $\phi \leq 0.02$ , where  $\eta_r(\phi)$  is approximately linear with respect to  $\phi$  and rheology is Newtonian. (ii) A semi-dilute region for  $\phi \leq 0.25$ , where higher order relationship is observed but behavior is still approximately Newtonian. (iii) A concentrated suspension ( $\phi \geq 0.25$ ) is characterized by rapid increase in apparent viscosity with particle volume fraction and behavior is seen to be non-Newtonian (shear thinning). Suspension behavior in the dilute limit was first theoretically developed by Einstein (1906, corrected 1911) [31]. His analytical equation considering hydrodynamic drag on particle in suspension yields:  $\eta_r = \frac{\eta_s}{\eta} = 1 + B\phi$  (2.2) where,  $\eta_s$  and  $\eta$  represent apparent suspension viscosity and carrier fluid viscosity,  $B$  is referred to as Einstein coefficient or intrinsic viscosity [31]. For dilute fluid,  $B$  was expected to be 2.5, however, different experiments suggested that  $B$  lies in the range  $1.5 \leq B \leq 5$ , instead of a single  $B$  value [32]. For semi-dilute regime, the higher order terms in  $\phi$  can be included:  $\eta_r = 1 + B\phi + B_1\phi^2 + \dots$  (2.3) with  $B = 2.5$  and  $7.35 \leq B_1 \leq 14.1$  by taking into account the interparticle interactions [33]. Polynomial equation, however, fails to contain data points beyond a critical concentration limit ( $\phi \geq 0.3$ ). It predicts finite viscosity value even when  $\phi \rightarrow 1$  which is unphysical as maximum packing fraction ( $\phi_m$ ) achievable for monodisperse spherical particles is 0.74. For disordered suspension system,  $\phi_m$  is even lower. For suspension under shear,  $\phi_m$  was found to be 0.68, most likely due to shear-induced structuration in suspension compared to random close-packing [34]. Therefore, for more accurate fitting of experimental results in high concentration regime,  $\phi_m$  was included as a parameter. By considering the contribution of successive packets of suspension to particle volume fraction and viscosity, Krieger & Dougherty (1959) derived the following relationship [35]:

$$\eta_r = \left(1 - \frac{\phi}{\phi_m}\right)^{-B\phi_m} \quad (2.4)$$

where  $B$  is Einstein coefficient. The Krieger-Dougherty equation better fits the experimental data. For the fitting,  $B$  and  $\phi_m$  are taken as fitting parameters. A typical Krieger-Dougherty equation fitting for  $\text{Fe}_3\text{O}_4$  agglomerate-based MR fluids is shown in

Figure 2.2. A similar type of relationship with same functional form was proposed by Maron & Pierce (1956) [36]:

$$\eta_r = \left(1 - \frac{\phi}{\phi_m}\right)^{-2} \quad (2.5)$$

This form can be used when there is a requirement for only one fitting parameter as  $B\phi_m$  is taken as 2. The influence of Brownian motion and inertia in flow characteristics of suspensions is governed by the Peclet number ( $P_e$ ) and Reynolds number ( $R_e$ ), respectively [37]:

$$P_e = \frac{6\pi\mu_0 a^3 \dot{\gamma}}{k_B T} \quad (2.6)$$

$$R_e = \frac{\rho_0 a^2 \dot{\gamma}}{\mu_0} \quad (2.7)$$

where  $k_B = 1.38 \times 10^{-23} JK^{-1}$  is Boltzmann constant,  $T$  is absolute temperature and  $a$  is particle radius.

Particle size distribution has a strong effect on viscosity of concentrated suspensions. The packing of the particles can be significantly affected by introducing smaller sized particles into larger spheres or by employing a wide particle size distribution in suspensions. The smaller particles act as ball bearings among the larger particles which accounts for a decrease in the viscosity. According to Chong et.al, at a fixed volume fraction of smaller particles, there is a particle size ratio below which the viscosity does not drop significantly [38]. The limiting particle size ratio of small to large spheres is about 1/10. If the ratio is smaller than 1/10, then the small spheres appear to behave like a fluid toward the larger spheres.

Non-spherical particles in a Newtonian fluid when subjected to shear rotate about the vorticity vector of flow. Its rotation is partly responsible for the bulk strain that the suspension experiences, so a rotating particle contributes to the suspension viscosity by smaller amount than a particle that cannot [25]. In order to determine the contribution of particles orientation in viscosity, we consider rotational motion of an ellipsoidal particle in simple shear flow (Fig. 2.3).

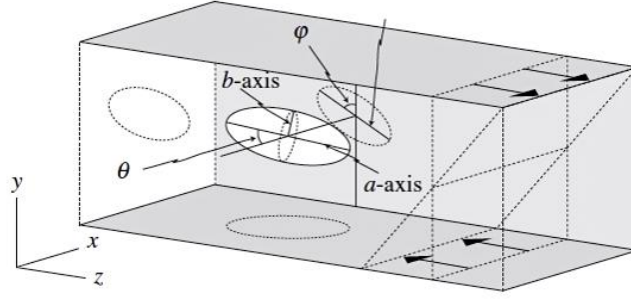


**Figure 2.3** Motion of spheroid in a shear flow.  $\theta$  is the angle between a-axis and vorticity vector;  $\phi$  is angle between ax and xy-plane. [37]

There are two cases of motion that can arise: (i) when particle's major axis is parallel to the vorticity vector ( $\theta = 0^\circ$ ), particle rotates with constant rotation rate  $\dot{\psi}$ . (ii) If particle rotates such that it's major  $a$ -axis is perpendicular to shear direction ( $\theta = 90^\circ$ ), it tumbles around its axes. For a simple shear flow, tumbling rate was given by Jeffery et.al [39],

$$\dot{\phi} = \dot{\gamma} \frac{1}{r_p^2 + 1} (r_p^2 \cos^2 \phi + \sin^2 \phi) \quad (2.8)$$

Where,  $\dot{\gamma}$  is shear rate and  $r_p$  is the aspect ratio of the particle. The period of rotation of particle about vorticity vector is found to be:

$$T = \frac{2\pi}{\dot{\gamma}} \left( r_p + \frac{1}{r_p} \right) \quad (2.9)$$

The relationship between  $\theta$  and aspect ratio  $r_p$  can be derived as follows:

$$\tan \theta = \frac{C r_p}{(r_p^2 \cos^2 \phi + \sin^2 \phi)^{1/2}} \quad (2.10)$$

where  $C$  is termed as 'Orbit constant' and can be determined from the above relation provided initial particle orientation is known. Now, rate of work ( $\dot{W}_p$ ) owing to the presence of particle phase in suspension of a volume  $V_p$  is related to relative viscosity as,

$$\eta_r = 1 + \frac{\dot{W}_p}{\eta \dot{\gamma}^2 V_p} \phi \quad (2.11)$$

where  $\phi = \frac{V_p}{V}$  is particle volume fraction. From the expression of  $\dot{W}_p$  derived by Jeffery et.al and the above equation, we can determine particle's orientational contribution to

viscosity. Qualitatively, when particle's major axis is parallel to flow, fluids have to perform extra work to flow around the particle, giving rise to smaller viscosity contribution [25]. When particle's major axis is perpendicular to flow, it rotates most rapidly and similarly viscosity will be minimal. However, when particle rotates in between, i.e. at  $45^\circ$ , particles contact area is large against the flow but moving slower than before. So, viscosity will be highest.

## 2.3 Linear viscoelasticity

### 2.3.1 Steady shear

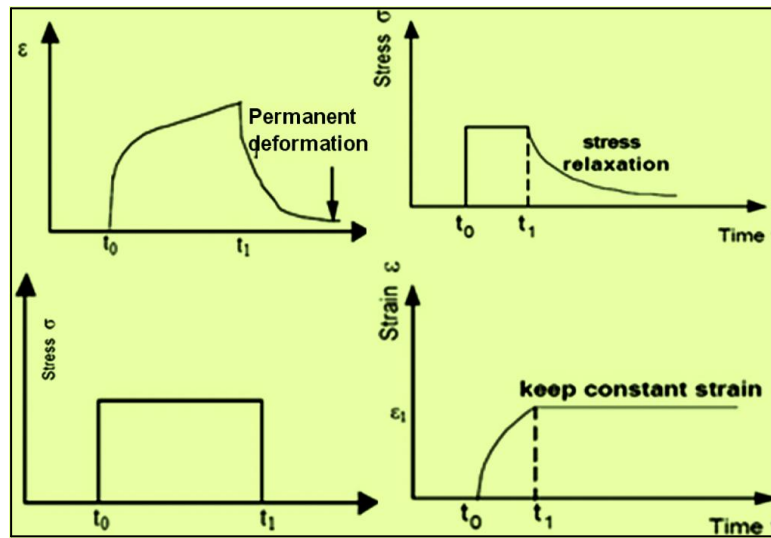


**Figure 2.4** Schematically illustrated plots for creep recovery (left) and stress relaxation experiment (right) in rotational rheometry [58].

Viscoelastic materials possess both elastic as well as viscous properties; hence stress-strain relationship is time-dependent. For a perfectly elastic material for small strain, Hooke's law of linear elasticity is obeyed, i.e. stress ( $\sigma$ ) is proportional to applied strain ( $\epsilon$ ):  $\sigma = E\epsilon$  where  $E$  is elastic modulus. This can also be expressed in terms of compliance ( $J$ ):  $\epsilon = J\sigma$  where  $J = 1/E$ . There is no energy loss during the loading-unloading cycle. For viscous materials, Newton's law is obeyed: shear stress,  $\tau = \eta\dot{\gamma}$  where  $\eta$  is viscosity coefficient and  $\dot{\gamma}$  is shear rate. Under constant strain, viscoelastic materials retain parts of the input energy and dissipate the rest. The stress-strain curve for loading-unloading cycle demonstrates hysteresis and area of the hysteresis loop determines the energy loss during the cycle. The behavior of viscoelastic materials can be explained by transient or, steady shear experiments, i.e. creep and stress relaxation (Fig.

2.4). Creep is slow and continuous deformation under constant stress. Upon removal of stress, strain relaxes with time exponentially. For stress relaxation, a constant strain is applied and stress decays exponentially with time. The explanation of linear viscoelasticity comes from Boltzmann superposition principle, which is often regarded as integral representation. The theory may be stated as:

- (a) The creep in a material is a function of entire loading history
- (b) Each change of load will make an independent and additive contribution to the total deformation

The first condition is related to memory effect, i.e. response of material is connected to the deformation history. Second condition means as follows: if a material is loaded and is creeping under load, then the addition of an extra load will produce exactly the same additional creep as if that total load had been applied to the unloaded material and the material is allowed to creep for the same amount of time. This is known as linear or additive response. Mathematical formulation according to Boltzmann theory states that the total strain at a time  $t$  is given by [40]:

$$\varepsilon(t) = \Delta\sigma_1 J(t - \tau_1) + \sigma_2 J(t - \tau_2) + \sigma_3 J(t - \tau_3) \quad (2.12)$$

where  $J$  is compliance and  $J(t - \tau_n)$  is creep compliance function. This introduces time factor to the expression. The integral form of the equation gives:

$$\varepsilon(t) = \int_{-\infty}^t J(t - \tau_n) d\sigma(\tau_n) \quad (2.13)$$

which can be rewritten by separating the time-dependent integral part from time-independent function as:

$$\varepsilon(t) = \left[ \frac{\sigma}{G_u} \right] + \int_{-\infty}^t J(t - \tau_n) \frac{d\sigma(\tau_n)}{d\tau_n} d\tau_n \quad (2.14)$$

where  $G$  is unrelaxed stiffness. Similarly, stress relaxation modulus can also be expressed as,

$$\varepsilon(t) = [G_r \varepsilon] + \int_{-\infty}^t (t - \tau_r) \frac{d\varepsilon(\tau_r)}{d\tau_r} d\tau_r \quad (2.15)$$

### 2.3.2 Dynamic measurements

According to the linear response theory, viscoelastic materials when subjected to sufficiently small deformation produce linear response. This applies to dynamic rheological measurements also. In this measurement, sample is subjected to a sinusoidal (cyclic) strain varying with time at an angular frequency  $\omega$ . For a Hookean solid, resulting stress is proportional to applied strain, therefore, stress and strain appear as *in-phase* components. For pure viscous materials, stress induced by sinusoidal strain is proportional to changes in acceleration of strain which is the first differential. Hence, there will be a phase difference of  $90^\circ$  (*out-of phase*). For viscoelastic materials, stress will oscillate sinusoidally with applied strain ( $\varepsilon = \varepsilon_0 \sin\omega t$ ) at a same frequency, but there will be a phase difference ( $\delta$ ) which effectively lies between 0 to  $90^\circ$ , i.e. stress,  $\sigma = \sigma_0 \sin(\omega t + \delta)$ , where  $t$  denotes time (Fig. 2.5).

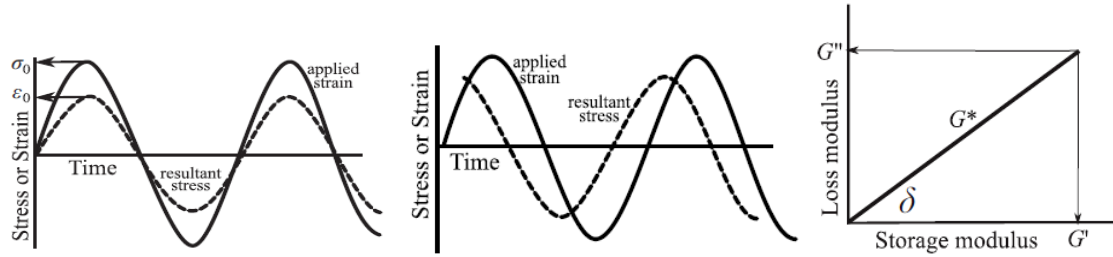


**Figure 2.5** Schematic illustrations of stress-strain relationship for Hookean solids and viscoelastic materials in oscillatory rheology. At right, vector representation of storage ( $G'$ ) and loss ( $G''$ ) modulus. The angle  $\delta$  denotes ratio of the two [reprinted from: Structural Biomaterials, J. Vincent, ©Princeton University press, 2012.]

In linear viscoelastic material, the stress component can be resolved into two stress waves— one is *in-phase* and the other is *out-of-phase* component such as:

$$\sigma_1 = \varepsilon_0 G'(\omega)$$

$$\sigma_2 = \varepsilon_0 G''(\omega)$$

Where  $\sigma_1$  and  $\sigma_2$  are stress components that are *in-phase* and *out-of-phase* with strain, respectively.  $G'$  and  $G''$  represent storage (in-phase) and loss (out-of-phase) modulus (Fig. 2.5).  $G'$  is the measure of recoverable energy whereas,  $G''$  is the measure of energy dissipated during a cycle. The ratio of imaginary (loss) and real part of complex modulus [ $G^*(\omega) = G'(\omega) + iG''(\omega)$ ] is defined as loss tangent such that:

$$\tan \delta(\omega) = \frac{G''(\omega)}{G'(\omega)}$$

The real ( $\eta'$ ) and imaginary ( $\eta''$ ) part of viscosity can also be deduced from the complex moduli as follows:

$$\eta'(\omega) = \frac{G''(\omega)}{\omega} \quad (2.16)$$

$$\eta''(\omega) = \frac{G'(\omega)}{\omega} \quad (2.17)$$

The *in-phase* component or real-part of complex viscosity is known as dynamic viscosity. At very low frequencies, dynamic viscosity is numerically equal to zero shear viscosity ( $\eta_0$ ).

## 2.4 Rheology of magnetorheological (MR) fluids

The relation between shear stress post-yield point and shear rate can be best approximated by the framework of generalized Newtonian fluid model which describes a linear relationship between shear stress and shear rate. The most commonly used empirical model is Bingham equation, proposed by Eugene Bingham (1926) considering viscoplastic behavior under simple shear [41]:

$$\begin{aligned} \tau &= \tau_y(H) + \eta_{pl}\dot{\gamma}, \tau > \tau_y(H) \quad (2.18) \\ \dot{\gamma} &= 0, \tau < \tau_y(H) \end{aligned}$$

where  $\eta_{pl}$  is plastic viscosity which is often independent of external magnetic field. For  $\tau < \tau_y(H)$ , MR fluids retain strongly elastic nature, therefore, no flow is initiated and  $\dot{\gamma} = 0$ . However, since MR fluids exhibit shear thinning behavior, the description of constant apparent viscosity with shear rate is incomplete and can be better explained by power-law models, such as Herschel-Bulkley and Casson equations [42, 43]. In Herschel-Bulkley viscoplastic equation, constant viscosity is replaced with a power-law term with shear rate [42]:

$$\tau = \tau_y(H) + k\dot{\gamma}^n \quad (2.19)$$

Where  $k$  is consistency parameter,  $n$  is power law index and describes whether the fluid behavior is shear-thinning ( $n < 1$ ) or shear-thickening ( $n > 1$ ). The Casson model predicts that

$$\sqrt{\tau} = \sqrt{\tau_y(H)} + \sqrt{\eta_c\dot{\gamma}} \quad (2.20)$$

where  $\eta_c$  is Casson viscosity.

The power-law models are used widely for medium range of shear rates. However, model prediction falls short at very low shear rates when power-law exponent  $n \leq 1$ . In this case, apparent viscosity approaches infinity, therefore, no flow is observed. It is experimentally observed that for dilute suspension, apparent viscosity is constant at low shear rate and Newtonian behavior is observed at higher shear rate. To overcome the shortcoming of power-law models, Cross (1965) developed an expression for experimentally observed viscosity variation under simple shear flow [44]:

$$\frac{\eta - \eta_\infty}{\eta_0 - \eta_\infty} = \frac{1}{1 + \lambda\dot{\gamma}^{1-n}} \quad (2.21)$$

For very low shear rates, apparent viscosity approaches to zero value ( $\eta_0$ ) and for high shear rates, it reaches a steady-state value of  $\eta_\infty$ . In between, Cross model predicts a power-law behavior.  $\lambda$  is a constant parameter with the unit of time and power law slope is  $(1 - n)$ . Careau-Yasuda model (1979) is an extension of Cross model and is expressed as difference between the apparent viscosity at a given shear rate to its zero shear rate value, instead of high shear rate [45]:

$$\frac{\eta - \eta_0}{\eta_\infty} = [1 + (\lambda\dot{\gamma})^a]^{(n-1)/a} \quad (2.22)$$

The parameter  $\lambda$  is a constant with units of time, the power law slope is  $(n - 1)$  and the parameter  $a$  represents the width of the transition region between  $\eta_0$  and the power-law region.

The theoretical prediction of field-dependent yield stress of an MR fluid is rather difficult to perform. Ignoring hydrodynamic contribution to flow, Lemaire and Bossis [46] modeled the static yield stress of magnetic fluids containing monodisperse particle network of equally spaced chains or networks. The restoring force of alignment is given as:

$$F_r = 3\mu_f a^2 \beta^2 H^2 f \quad (2.23)$$

Where  $a$  is the diameter of the particles,  $\mu_f$  is the permeability of the suspension,  $H$  is the effective field,  $\beta = \frac{\mu_p - \mu_f}{\mu_p + 2\mu_f}$  and function  $f$  depends on the separation between two spheres and on the ratio of  $\frac{\mu_p}{\mu_f}$ . Once  $\mu_p(H)$  and  $\mu_f(H)$  are known, the restoring force can be calculated and its maximum value  $F_r^m$ , will give the yield stress:

$$\tau_s = n_s F_r^m \quad (2.24)$$

where  $n_s$  is the number of chains per unit surface. Considering the macroscopic approaches, Bossis further developed a model for high particle volume fraction ( $\phi$ ) and ellipsoidal particles [46]. The stress parameter is calculated using mean field approximation for non-interacting ellipsoidal particles immersed in suspending medium of permeability  $\mu(\phi)$ :

$$\frac{\tau}{\mu_f H^2} = \frac{\phi \mu(\phi)}{2 \phi_a \mu_f} \mu_m^* \frac{\partial}{\partial y} \left( \frac{1}{(1 + \gamma^2)(1 + \mu_m^* n_{\parallel})} + \frac{\gamma^2}{(1 + \gamma^2)(1 + \mu_m^* n_{\perp})} \right) \quad (2.25)$$

Where  $\mu_m^* = \frac{\mu_s(\phi)}{\mu(\phi)} - 1$  and  $n_{\parallel}$  and  $n_{\perp}$  are demagnetizing factors for ellipsoid particle. The effective field is given by  $H = \frac{H_0}{\mu(\phi)}$  and  $\mu_s(\phi)$  and  $\phi_a$  are permeability of the disperse phase and internal volume fraction, respectively. Rosensweig (1995) also developed a model for yield stress considering the unsymmetrical stress states [48]. According to the model, yield stress ( $\tau_x$ ) is related to anisotropic susceptibility ( $\chi$ ) and defined for parallel layers as:

- for particles without demagnetization:  $\frac{2\tau_x}{(\mu_0 H_0^2)} = \frac{\phi(1-\phi)\chi^2}{2[1+(1+\phi)\chi]} \quad (2.26)$

- for particles with demagnetization:  $\frac{2\tau_x}{(\mu_0 H_0^2)} = \frac{\phi(1-\phi)\chi^2}{2\sqrt{(1+\chi)(1+\phi\chi)[1+(1-\phi)\chi]}} \quad (2.27)$

However, the models discussed are based on linear approaches and the yield stress, shear stress are found to be proportional to  $\phi \mu_0 H_0^2$ . Furthermore, these models don't consider particle magnetic saturation under field. In experiments, the trend is often non-linear. Therefore, a model was developed by Ginder and Davies (1994) by taking into account the particle magnetic saturation [49] and is valid beyond a certain magnetic field. They considered static yield stress as maximum shear stress and is a component of tensile stress along the direction of shear of a linear chain consisting of spherical particles. According to Ginder *et al.*, at intermediate field range, yield stress is dependent to field sub-quadratically:

$$\tau_y = \sqrt{6} \phi \mu_0 M_s^{1/2} H^{3/2} \quad (2.28)$$

Where,  $M_s$  is saturation magnetization and  $H$  is external magnetic field.

When the magnetic field is sufficiently high, particles saturate magnetically and thus can be treated like a dipole. For this, yield stress is independent of applied magnetic field ( $H$ ) and can be expressed as:

$$\tau_y^{sat} = \frac{4}{5} \xi(3) \phi \mu_0 M_s^2 \quad (2.29)$$

Where  $\xi(3) = 1.212$  and is a constant. However, a more accurate fitting of experimental results are reported when applied magnetic field is replaced by particle's magnetization ( $M$ ) data from M-H hysteresis curve. Klingenberg *et al.* (2007) reported a better fitting for yield stress curves when magnetic field was replaced by particle magnetization, i.e.  $\tau_y \propto \langle M_p^2 \rangle$ , where  $M_p$  is particle magnetization [50].

The stability of MR fluids against gravitational settling has been one of the most important issues. For dilute systems, the dependence of the sedimentation velocity ( $v$ ) of a spherical particle can be obtained from Stoke's law as follows:

$$v = \frac{2}{9} \frac{a^2 (\rho_s - \rho_l) g}{\eta} \quad (2.30)$$

where  $a$  is the particle radius,  $\rho_s$  and  $\rho_l$  are the density of the magnetic phase and carrier liquid,  $\eta$  is the viscosity of the carrier liquid and  $g$  is the gravitational acceleration ( $9.8 \text{ m/s}^2$ ). Since, less viscous fluids accelerate the settling of the particles more rapidly, it is suggested that suspensions with viscoplastic matrix (e.g., grease) can prevent sedimentation. However, for most of the applications it is customary to choose carrier fluid with off state viscosity as small as possible to maximize the stress output [51].

3

## Chapter 3

### Experimental Procedures

*In this chapter, we described various methods for synthesizing binary ferromagnetic alloys of Fe, Ni and Co along with Fe oxides by chemical co-reduction of respective metal salt precursors. We further discussed the experimental techniques that were used to characterize particles' morphology, crystal structures and magnetic properties such as scanning electron microscopy (SEM), energy-dispersive X-ray (EDX), transmission electron microscopy (TEM), X-ray diffraction (XRD) and vibrating sample magnetometry (VSM). Bulk rheology of the MR fluids under magnetic fields were conducted using commercial Anton Paar Physica MCR series Rheometer<sup>®</sup> with MR attachment MRD-170<sup>®</sup>. The rheometer design and operating principle under different configurations were also outlined.*

### 3.1 Synthesis of alloyed nano/microparticles of Fe, Co and Ni

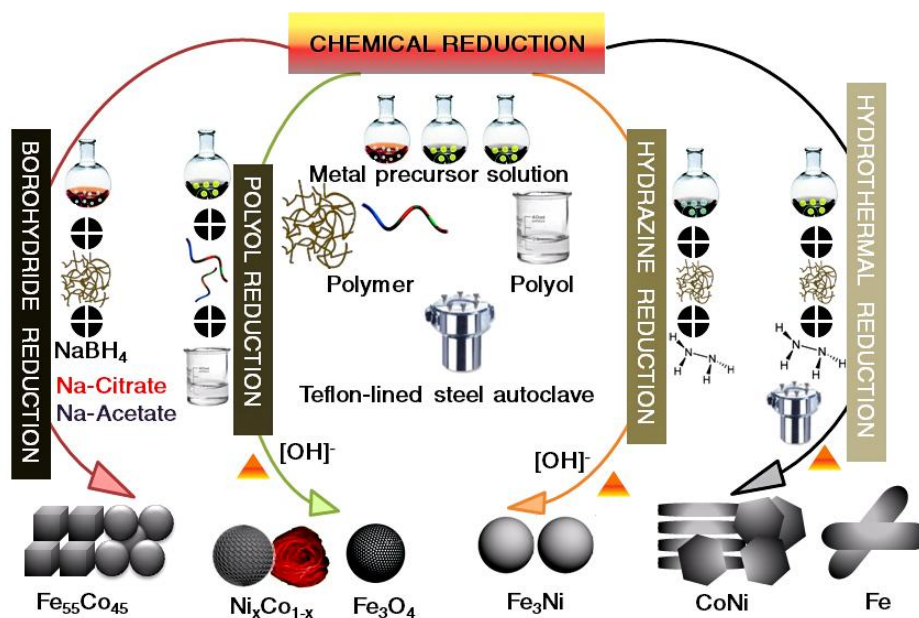


**Figure 3.1** Schematic of various chemical reduction methods for synthesizing nano-/microparticles of metal alloys and oxides with different shapes, sizes and compositions

Micron-sized particles of ferromagnetic binary alloys of Fe, Co and Ni, as well as Fe<sub>3</sub>O<sub>4</sub> with different morphologies, sizes and compositions were synthesized by various chemical co-reduction methods from a precursor of metal salts solution. This is schematically illustrated in Figure 3.1. By careful control of reaction conditions, micron-sized particles with desired properties and morphologies were synthesized.

#### 3.1.1 Synthesis of Fe<sub>55</sub>Co<sub>45</sub> microparticles by borohydride reduction

Sodium citrate (ACS reagent, ≥99.0%) tribasic stabilized Fe<sub>55</sub>Co<sub>45</sub> microparticles were obtained by ultrasonic assisted aqueous borohydride reduction. This particular composition yields structure and morphologically diverse microstructures depending upon the choice of the additives. In addition, compositional homogeneity and monodispersity are also prime reasons for selecting this particular composition. Sodium borohydride (Merck™, ≥95%) was used as reducing agent. [Fe] + [Co] to borohydride ratio was kept at 1:2 and metal to citrate ratio was maintained at 1:8. In a typical experiment, 0.1M Fe (II) chloride (ACS reagent, ≥98%) and 0.088M Co (II) acetate tetrahydrate (ACS reagent, ≥98%) were dissolved in 30 mL Millipore™ water previously purged with argon flow. The precursor solution containing metal salts and sodium citrate

was taken in a three-necked round bottom flask on ultrasonic bath maintained at 15°C. Sodium borohydride (0.376M) was added drop-wise to the mixture kept under constant mechanical stirring and argon (Ar) flow, for about 20 minutes. For sodium acetate (anhydrous, Aldrich™, ≥99.0%)-PEG (PEG-6000, SRL Chemicals™) couple encapsulated Fe<sub>55</sub>Co<sub>45</sub>, 0.3 g PEG 6000 was added to the precursor solution prior to the addition of sodium acetate (1.5M). After the reaction, sedimented particles were separated magnetically and washed multiple times using Millipore® water, acetone and absolute ethanol. These were finally dried in vacuum overnight.

### 3.1.2 Synthesis of Ni<sub>x</sub>Co<sub>1-x</sub> micro- and nanoparticles by polyol reduction

#### 3.1.2.1 Ni<sub>x</sub>Co<sub>1-x</sub> flower like microstructures

The synthesis of Ni<sub>x</sub>Co<sub>1-x</sub> nanoflowers was carried out by one-pot polyol reduction in presence of amphiphilic triblock copolymer O,O'-Bis (2-aminopropyl) poly(propyleneglycol)-*block*-poly(ethyleneglycol)-*block*-poly(propyleneglycol) Jeffamine® ED-600 with approx. mol. wt. M<sub>r</sub> ~600, Sigma Aldrich). In this process, precursor solutions were prepared by dissolving Ni (II) acetate tetrahydrate (≥98%, Sigma-Aldrich) and cobalt (II) acetate tetrahydrate (≥98.0%, Sigma-Aldrich) in 1, 2-propanediol (PrG, Loba Chemie™) with different molar ratios. A set of five solutions were prepared with a total molar conc. of metals fixed at 0.25M for Ni<sub>x</sub>Co<sub>1-x</sub>, where x = 0.2, 0.4, 0.5, 0.6 and 0.8 respectively. A PrG solution of Jeffamine (5 mL, 0.82 g) was added to each precursor and was sonicated under flowing argon gas for 30 minutes to ensure complete homogeneity and absence of dissolved oxygen. Afterwards aqueous potassium hydroxide (10 mL, 0.75 M), previously purged with argon, was added drop-wise to the precursor under constant stirring. The resulting solution turned bluish-green due to the formation of mixed metallic double hydroxide, i.e. homogeneous solid phase. The suspension was then quickly transferred to a two-necked round bottom flask and boiled. To boil off water, temperature of the suspension was maintained at 130°C for 20 minutes. Afterwards the reaction flask was fitted with a double walled reflux condenser and refluxed for 3 hours. The reacting solution achieved homogeneity at the boiling point of liquid polyol. Following a nucleation and

growth phase, black precipitate formed at the bottom of vessel, indicating formation of NiCo alloy. The purified NiCo suspension was obtained by centrifugation and subsequent washing with Millipore<sup>®</sup> water, acetone and absolute ethanol. In order to obtain NiCo powder, suspension was dried in air at 60°C. To investigate the role of polyol on the growth mechanism of hierarchic NiCo nanostructures, above procedure was repeated using ethylene glycol (EG, Merck) and tetraethylene glycol (TEG, Merck).

In separate experiments, poly-acrylic acid (PAA, avg. mol. wt. ~1800, Sigma-Aldrich) and cetyltrimethylammonium bromide (CTAB, 99%, Loba Chemie)-assisted Ni<sub>50</sub>Co<sub>50</sub> nanoflowers were synthesized by adding 20 wt % and 0.02M of PAA and CTAB solutions into the precursor solution respectively, under the otherwise similar conditions stated above.

#### *3.1.2.2 Ni<sub>0.1</sub>Co<sub>0.9</sub> microcluster*

The synthesis of spherical Co<sub>0.9</sub>Ni<sub>0.1</sub> nanoclusters was carried out by standard polyol reduction method. The Co-rich Co<sub>0.9</sub>Ni<sub>0.1</sub> alloy was selected as preferred composition due to its higher saturation magnetization than 1:1 alloy. Furthermore, cluster-like morphology is more prevalent in Co-rich alloys. In this process, precursor solution was prepared by dissolving nickel (II) acetate tetrahydrate (≥98%, Sigma-Aldrich) and cobalt (II) acetate tetrahydrate (≥98.0%, Sigma-Aldrich) in ethylene glycol (Merck) with 1:9 molar ratios. For the synthesis of Co<sub>0.9</sub>Ni<sub>0.1</sub>, total molar concentrations of the metals were fixed at 0.5M. Ethylene glycol (EG) served both as reducing agent and surface binding material. Afterwards, EG solution of sodium hydroxide (10 mL, 1.5 M), previously purged with argon, was added drop-wise to the precursor under constant stirring. The resulting solution turned bluish-green due to the formation of mixed metallic double hydroxide, i.e. homogeneous solid phase. The suspension was then refluxed under nitrogen blanket at 200°C for 2 hours. The purified Co<sub>0.9</sub>Ni<sub>0.1</sub> suspension was separated by centrifugation and subsequent washing with Millipore<sup>®</sup> water, acetone and absolute ethanol. Afterwards, the suspension was dried in air at 60°C to obtain the powder.

#### *3.1.2.3 NiCo nanoplatelets*

NiCo plate-like nanoparticles were prepared by solvothermal method in aqueous media. For the synthesis, hydrazine was used as reducing agent for the reduction of precursor solution containing Co (II) acetate and Ni (II) acetate in equimolar ratio. CTAB (Cetyltrimethylammoniumbromide, 99%, Loba Chemie) was used as surfactant for directive growth of plate-like hexagonal nanoparticles along the preferred plane. Co (III) acetate (0.05 M), Ni (II) acetate (0.05 M) and CTAB (0.15 M) were dissolved to Millipore® water (30 mL) following stirring using a magnetic stirrer. An aqueous solution of hydrazine hydrate (0.2 M, Ranbaxy™) was added to the precursor dropwise prior to transferring the resulting solution into a Teflon-lined stainless steel autoclave. The autoclave was kept for 21 hours inside a hot-air oven set to 160°C. The supernatant was removed by centrifugation, and the precipitate was vacuum-dried to yield the black powder.

### **3.1.3 Synthesis of Fe<sub>3</sub>Ni microparticles by hydrazine reduction**

Hydrazine reduction of Fe (II) chloride (Merck) and Ni (II) acetate in 1:1 water-ethanol precursor solution is described as follows: Ni (II) acetate, Fe (II) chloride and polyacrylic acid (PAA, avg. mol. wt. ~1800, Sigma-Aldrich) were dissolved in 30 mL 1:1 water-ethanol solution ( $[\text{Ni}^{2+}] = 0.02 \text{ M}$ ,  $[\text{Fe}^{2+}] = 0.06 \text{ M}$ ,  $[\text{PAA}] = 0.1 \text{ M}$ ). Separately, sodium hydroxide (NaOH) and hydrazine hydrate (0.2 M, Ranbaxy™) were dissolved in water-ethanol solution. The two solutions were mixed together under continuous and vigorous stirring in a magnetic stirrer. The temperature was raised to 65°C under constant purging of Argon (Ar) gas into the solution. The reaction was continued for 2 hrs. Afterwards, the resultant product was washed thoroughly with deionized water for removal of reaction residues followed by washing with acetone. Finally, the black particles were soaked in ethanol in a closed container for further characterization.

## **3.2 Synthesis of Fe<sub>3</sub>O<sub>4</sub> and Fe microparticles**

### **3.2.1 Fe<sub>3</sub>O<sub>4</sub> microsphere by thermal decomposition of organometallic precursor**

Spherical magnetite microparticles were synthesized by previously described thermal decomposition method of Fe (III) acetylacetonate (99%, Sigma-Aldrich) in liquid polyol. In this method, organometallic precursor solution in ethylene glycol (EG, Merck) was refluxed for 3 hours in presence of polyacrylic acid (PAA, avg. mol. wt. ~1800, Sigma-

Aldrich). The molar ratio of polymer and Fe (III) acetylacetonate was maintained at 2:1. The appropriate amount of metal salt was stirred to dissolve in EG followed by rapidly heating to boil at 120°C for 30 minutes. Afterwards, the precursor was transferred to a round-bottom flask under steady nitrogen gas flow and refluxed at 200°C for 4 hours. EG acted both as solvent and reducing agent. After the reaction was complete, dark brown precipitate of magnetite was formed by partial reduction of Fe (III) salt. The microparticles were isolated by centrifugation following repeated wash with water and ethanol. The PAA was involved in surface functionalization and structural evolution of Fe<sub>3</sub>O<sub>4</sub> nanospheres. Final shape of the nanoparticles was evolved through LaMer's method of fast super-saturated burst nucleation mechanism followed by aggregation and final growth to nanospheres [52].

### **3.2.2 PVC-Fe<sub>3</sub>O<sub>4</sub> agglomerate by coprecipitation method**

PVC-coated magnetite composite nanoparticles were synthesized by a modified chemical coprecipitation method [53] from a precursor solution of Fe (III) chloride and Fe (II) sulphate in 1: 1.5 molar ratios in 8 mL of distilled water. 10 mL of nearly saturated aqueous solution of poly-vinyl chloride was added to it, along with surfactant and 2 mL of 12N hydrochloric acid (HCl). This slightly acidic solution was collected in a three-necked round-bottom container. 90 mL of 1M aqueous NaOH solution was then added to it and stirred mechanically with a rotating stirrer, while a continuous flow of argon was maintained to create inert atmosphere inside the vessel. The pH of the resulting mixture was adjusted between 7.8 – 8.0. The temperature was raised to 75°C by means of a water bath positioned under the flask. The stirring was continued for 15 minutes at the speed of 3000 rpm. The dark brown precipitate was extracted using a permanent magnet, then centrifuged at 2000 rpm and washed with double-distilled water thrice. Afterwards, it was again washed with 10 mL 0.002M HCl. Finally, the solid was air dried at 60°C for 24 hours. For the above synthesis, oleic acid was used as surfactant.

### **3.2.3 Iron (Fe) microrod by hydrothermal reduction**

Iron (Fe) microrod was prepared by polyol-assisted solvothermal method. For the synthesis of Fe-microrod, EG-hydrazine was used as reducing agents for the reduction of precursor solution. CTAB (99%, Loba Chemie™) was used as surfactant for directive

growth of nanorods along the preferred plane. Fe (III) nitrate (0.02 M, Loba Chemie) and CTAB (0.05M) were dissolved in EG (30 mL) following rapid mechanical stirring. An aqueous solution of hydrazine hydrate (0.05M, Ranbaxy) was added to the precursor dropwise prior to transferring the resulting solution into a Teflon-lined stainless steel autoclave. The autoclave was kept for 7 hours inside a hot-air oven set at 200°C. The supernatant was removed by centrifugation, and the precipitate was vacuum-dried to yield the black powder. Since the relative yield of nanorod was less than 50%, repeated centrifugation of the precipitated black powder was necessary. The supernatant was rejected while heavier microrods were collected at the bottom.

### **3.3 Characterization**

The dried powders of binary alloys and oxides were characterized using various methods. Crystal structures of the alloys and oxides were determined with X-ray diffraction (XRD) performed on the powdered samples. Compositions and morphology of the samples were determined using energy dispersive x-ray (EDAX) analysis, FESEM and TEM. To determine magnetic properties at room temperature, we performed magnetic measurements using a vibrating sample magnetometer (VSM).

#### **3.3.1 X-ray Diffraction**

X-Ray Diffraction (XRD), first observed in 1912 in a crystal, is the first step in determining the phase of the materials. The interaction of X-ray of suitable wavelength with the crystal, results in elastic scattering of the radiation. The periodic arrangement of atoms in crystal leads to definite phase relation between radiations scattered elastically from the atom, leading to constructive and destructive interferences, giving rise to diffraction pattern. Although each atom acts as a scattering center, the pattern can be explained by assuming that a plane of atoms acts as scattering source. If the parallel planes are separated by a distance  $d$ , then the constructive interference takes place only when the angle of incidence ( $\theta$ ) of the incident radiation of wavelength  $\lambda$  is such that it satisfies the relation  $2d \sin\theta = n\lambda$ , where  $n$  is integral (the process is shown in the Fig. 3.2). This is called Bragg's law. The distance between planes and the lattice parameter of

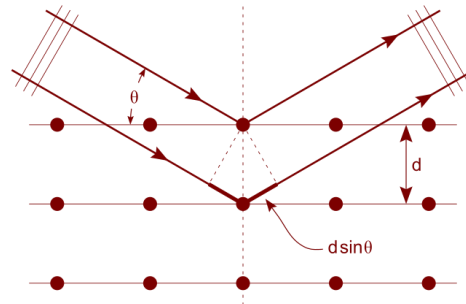


**Figure 3.2** X-ray diffraction from lattice planes with spacing  $d$ . The diffraction maximum appears at an angle  $\theta$  whenever the path difference  $2d \sin \theta = n\lambda$ .

a crystal can be obtained by using Bragg's law from the diffraction pattern obtained from a diffractometer. The X-Ray diffraction measurements were performed with either a RIGAKU<sup>®</sup> MiniFlex<sup>II</sup> diffractometer or a PANalytical X'Pert PRO<sup>®</sup> diffractometer using monochromatic  $Cu - K_{\alpha}$  radiation ( $\lambda = 0.51418 \text{ nm}$ ). The powdered particles were kept in a sample holder and XRD pattern was obtained with scan rate of  $1^{\circ}/\text{min}$  and step size of  $0.02^{\circ}$ . The obtained diffraction patterns were compared with existing databases (ICDD, JCPDS) to predict the composition and crystal structures.

### 3.3.2 Scanning electron microscopy & Energy dispersive x-ray analysis

A Scanning Electron Microscope (SEM) is widely used in nanoparticles imaging and composition analysis techniques in material science. This works due to the fundamental quantum property of matter called wave particle duality. A moving electron has an associated wavelength  $\lambda$  (known as de Broglie wavelength =  $h/p$  where  $h$  is Plank's constant and  $p$  is the momentum of the electron). Under acceleration potential of only  $100 \text{ V}$ , the electron has a  $\lambda = 0.12 \text{ nm}$  that is many times smaller than visible light. The extremely small de Broglie wavelengths make it possible for us to probe into atomic structures using electrons. This is the basic principle of electron microscopy. An additional advantage of extremely short wavelength is enhanced angular resolution, given by Rayleigh's criterion:

$$\text{angular resolution} = \frac{1.22\lambda}{D}$$

where  $\lambda$  is the wavelength of beam and  $D$  is the aperture diameter of the instrument. This is why electron microscopes have extremely high resolving powers.

The SEM also has a very high depth of field, which allows for a large amount of the sample to be in focus at one time and produces an image that is a good representation of

the three-dimensional sample. The combination of higher magnification, greater depth of field and resolution, and localized compositional and crystallographic information makes the SEM one of the most heavily used instruments in academic scientific research areas and industries.

We used a commercial field emission scanning electron microscope (FESEM) Quanta FEG 250<sup>®</sup> (FEI). A schematic of SEM set up is shown in Fig. 3.3A. It works by using a beam of electrons emanating from an electron gun in high vacuum and is accelerated by a high potential difference and finally collimated. The beam is focused onto sample with the help of electrostatic field. Accelerated electrons in an SEM carry significant amounts of kinetic energy and this energy is dissipated as a variety of signals produced by electron-sample interactions when the incident electrons are decelerated in the solid sample. These signals include secondary electrons (that produce SEM images), backscattered electrons (BSE), diffracted backscattered electrons (EBSD that are used to determine crystal structures and orientations of minerals), photons, visible light and heat. Secondary and backscattered electrons are used for imaging samples: secondary electrons are most useful for showing morphology and topography on samples and backscattered electrons are for illustrating contrasts in composition in multiphase samples (i.e. for rapid phase discrimination).

Among the inelastic collision processes, X-ray is also generated by collisions of incident electrons with electrons in discrete orbitals (shells) of atoms in the sample. Since each element emits its own characteristic X-ray, thus by measuring the number of these X-ray photons and the energy of X-ray by using energy-dispersive X-ray (EDAX) detector placed inside the SEM chamber one can also determine composition of sample non-destructively. A typical SEM image and EDAX curve for CoNi nanoplatelets with 1:1 composition are shown in the Fig. 3.3B and 3.3C [54].

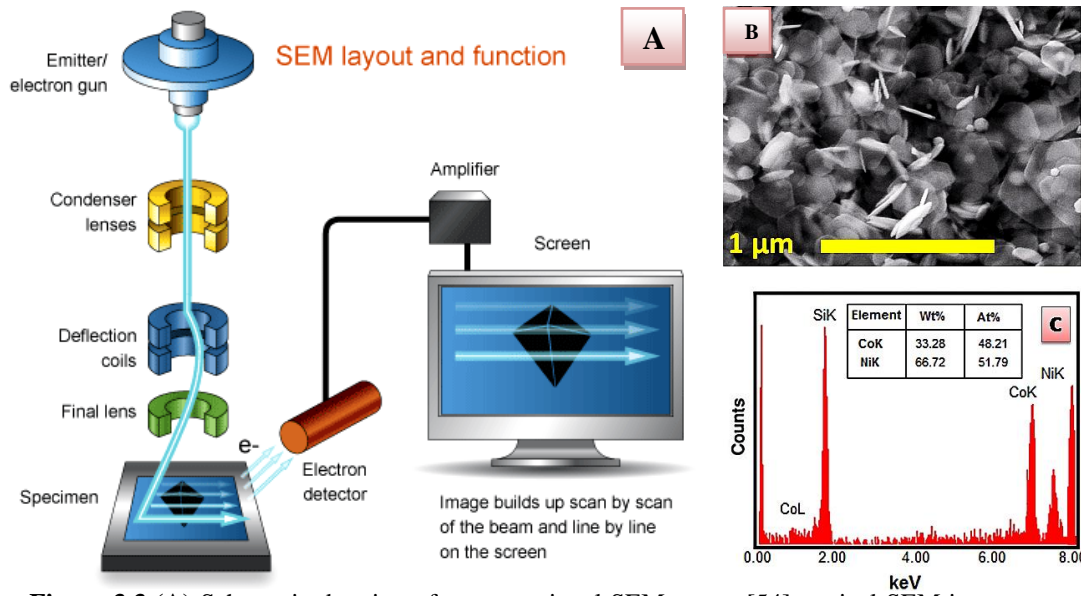


**Figure 3.3** (A) Schematic drawing of a conventional SEM set up [54], typical SEM image and EDAX spectra of CoNi (1:1) nanoplatelets (B & C).

### 3.3.3 Transmission electron microscopy (TEM)

In transmission electron microscopy (TEM), a beam of electrons is transmitted through an ultra-thin sample specimen, interacting with the sample as it passes through it. An image is formed from the interaction of the electrons transmitted through the specimen; the image is magnified and focused onto an imaging device, such as a fluorescent screen, or a CCD camera. The schematic of a standard TEM optical components is shown in Fig. 3.4A [55]. Due to smaller de Broglie wavelength of electron, TEM can produce significantly high resolution images of ultrafine nanoparticles and nanostructured materials. In addition to the basic surface imaging, TEM also offers to observe changes in chemical composition (EDAX), crystal structures and orientation, electronic structures and sample induced electronic phase shifts etc.

For the sample morphology, selected area diffraction and compositional studies, we used Technai F20<sup>®</sup> transmission electron microscope (TEM). The general TEM assembly consists of: (i) electron sources, (ii) lenses and apertures, (iii) vacuum pumps, (iv) grid, sample holders and stages, (v) electronic imaging and recording. The surface of sample is illuminated by parallel or near-parallel electron beams. Two types of electron source generation are reported: thermionic and field emission. In case of thermionic sources, cathode filaments are made of tungsten (*W*) filament or lanthanum hexaboride (*LaB<sub>6</sub>*)

crystals. For thermionic emission, current applied to W filament to heat sufficiently so that electrons come out of the surface. For field-emission (FE) sources, the fine-tip tungsten needle acts as cathode with respect to two anodes. No direct heating is involved in FE-based systems. An extraction voltage is required to pull electrons out of the gun, followed by a beam acceleration made up by a system of electrostatic lenses. For TEM, focusing of electron beam is performed by electromagnetic lens (Fig. 3.4B). It consists of two parts: cylindrical core with a hole in middle is made up of soft magnetic materials such as Fe. It is known as polepiece. A secondary coil of Cu also surrounds the polepieces. The lens system ensures the focusing of the electron beam when the current is passed through the coils. Sample contamination can arise due to the electron scattering in presence of gas in the TEM chamber. Therefore, vacuum system is inevitable for TEM setup. A typical TEM vacuum can reach up to  $10^{-5} - 10^{-7}$  Pa pressure. Finally, sample preparation for TEM visualization is also a very crucial stage. Sample must be electrically 'thin' to let the electrons pass through it when placed on Cu mesh grid covered with thin carbon monolayer (Fig. 3.4C). For all the samples prepared for the thesis were micro- and nanoscale particles dispersed in ethanol. Therefore, a drop of sample dispersions was placed onto the Cu-grid and solvent was evaporated so that particles were fixed on grid surface. After the sample was properly prepared, the grid was placed inside the TEM column, with the help of holder and stage. Holder is a rod that keeps the sample grid attached when it is inserted inside microscope. The holder can also be rotated to adjust the view of sample in different positions on grid. The stage is a platform which contains airlocks so that the holder can be inserted inside the vacuum with minimum increase in pressure. For electron imaging and recording, two different sections are used in TEM: viewing screen and electron detector. Viewing screen is placed at the bottom of TEM, below the projector lens and above electron detector. The electron detector here uses a charge-coupled-device (CCD) which can be useful for recording real-time images and diffraction patterns as well as other techniques such as electron energy loss spectra (EELS).

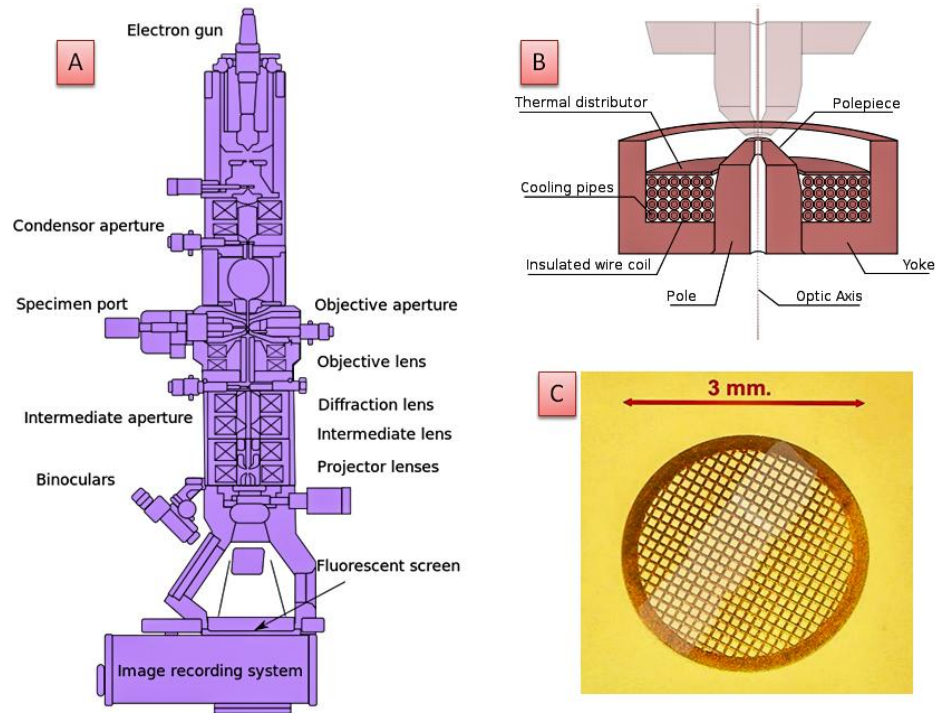


**Figure 3.4** Clockwise from left: schematic of a basic TEM optical component layout (A), diagram of a TEM split polepiece design electromagnetic lens (B), TEM sample support Cu mesh grid (C) [55].

Scattering of electron takes place when electrons hit the sample surface. Two types of scattering are usually observed: elastic scattering where electrons don't lose energy after hitting the surface and inelastic scattering where electrons lose energy after collision process. Scattered electrons are coherent, i.e. they remain in phase step, but for inelastic electrons there is no phase relationship. Elastically scattered electrons are biggest source of contrast in TEM images and diffraction patterns. The most commonly used imaging technique in TEM is bright field TEM (BFTEM) where electron beam transmitted through the sample surface scattered elastically with small angle of deviation and interact with the CCD camera to provide the final image. The resulting contrast image is produced by spatial distribution of elastically scattered electrons emanating from sample. In our work, we used bright field TEM images of microstructures and nanostructured materials to study shape and size distribution. Selected area electron diffraction (SAED) is also carried out in TEM. The technique is analogous to the x-ray diffraction pattern. The interference pattern is generated by angular distribution of small angle ( $< 5^\circ$ ) elastically scattered electrons that hit the CCD. SAED is a great tool to study the

structures of crystalline materials. It also reveals the interplanar spacing in nanocrystalline materials. A typical BFTEM image of FeCo nanoparticle along with SAED pattern is shown in Fig. 3.5A and Fig. 3.5B, respectively.

High angle annular dark field (HAADF) images provide contrast with atomistic details when scattered electrons are of higher angles. This technique operates in STEM mode only. The beams that scattered with high angle ( $> 5^\circ$ ) can generate high quality images with atomic resolution and it depends only on atomic number ( $z$ ) of the atom that conforms the substrate. Depending on the atomic number of the sample element, the image can be bright field or dark field. A typical HRTEM image for FeCo cubic nanoparticle is shown in Fig. 3.5C.

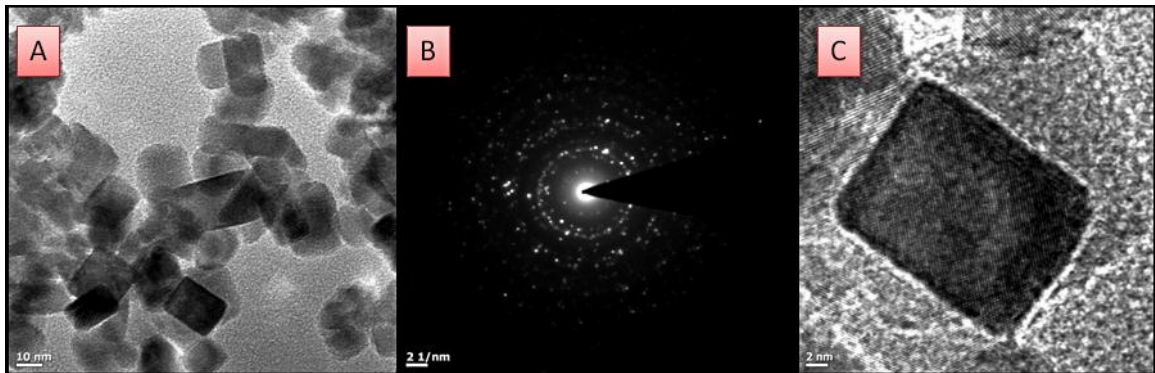


**Figure 3.5** From left: bright field TEM image of FeCo nanocubes (A), SAED pattern (B) and HAADF-STEM image (C) of the same.

Energy electron loss spectroscopy or EELS consists of the electrons that have gone through the substrate and scatter elastically or inelastically. The EELS is very important for analyzing the electronic structure and chemical composition of the sample atoms, in addition to the valence state and chemical environment of the surrounding atoms. EELS can be complimentary to EDAX technique since both of them reveal chemical composition of matter. However, acquiring EELS demands very thin sample specimen. It can also be noted that lighter elements appear in EELS but in EDAX, heavier elements can be detected. A typical EELS spectra plots the number of electron counts as a function of energy loss of electron.

### 3.3.4 Vibrating Sample Magnetometer (VSM)

Vibrating Sample Magnetometer (VSM) systems are used to measure the magnetic properties of materials as a function of magnetic field, temperature and time.

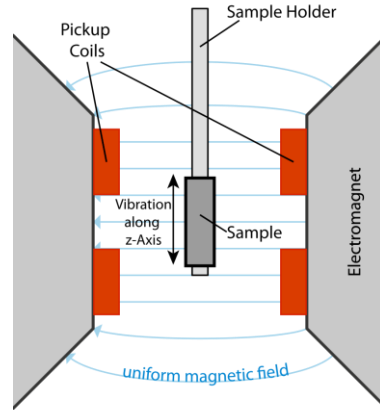


**Figure 3.6** Schematic of vibrating sample magnetometer (VSM).

A magnetic moment  $m$  is induced in the sample when it is placed in a uniform magnetic field  $H$ . In a VSM, a sample is placed within sensing coils under constant magnetic field (generated by an electromagnet), and the sample is given a sinusoidal mechanical oscillation at a fixed frequency. The magnetic dipole moment of the sample will create a magnetic field around the sample, known as magnetic stray field. As the sample is vibrated, the magnetic stray field changes as a function of time and can be sensed by a set of pick-up coils. The alternating magnetic field causes an electric current in the pick-up coils according to Faraday's Law of Induction. This current is proportional to the magnetization of the sample. Therefore, the greater the magnetization, the greater will be the magnitude of induced current. The induction current is measured after suitable amplification circuits. In a VSM, all these various components are hooked up to the computer interface. The schematic of the VSM and detailed configuration near the pick-up coil is given in Fig. 3.6 [56,57].

The magnetic measurement of the samples was performed in a Lake Shore Cryotronics<sup>®</sup>, Inc. made 7400 Series<sup>™</sup> VSM. The maximum magnetic field generated in it was 1.56 T. The field produced had homogeneity of  $\pm 0.1\%$  over a 5 cm diameter circle. The low temperature measurement was performed using Model 74018<sup>™</sup> variable temperature cryostat, which allows measurements from 80 K to 400 K.

### 3.4 Magnetorheometry

The magnetorheometric devices (to measure rheology of MR fluids) can be classified as having either fixed plates (pressure-driven flow mode or valve mode) or relatively

moveable plates (direct-shear mode and squeeze-flow mode). The schematic of these three basic operating modes in standard rheometric devices are shown in Fig. 3.7.

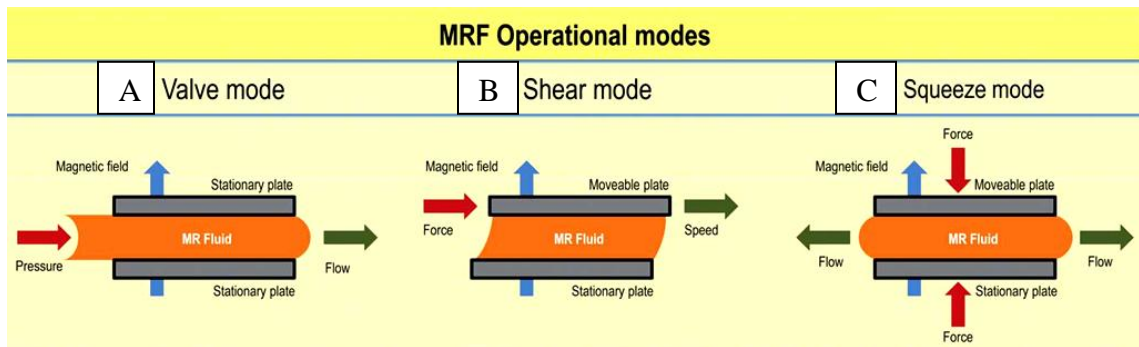


**Figure 3.7** Basic operating modes of MR fluid devices: (A) pressure driven flow mode, (B) direct shear mode, and (C) biaxial squeeze flow mode (*Materials and Design*, A. G. Olabi, A. Grunwald, **28**, 2658 ©Elsevier 2007).

Out of these three operational modes, direct shear mode is most commonly used tool in standard rheometer to investigate MR effect in MR fluids. Almost all commercially available rheometers operate in this mode, either in parallel-plate, cone-plate or concentric-cylinder configurations. The details of these geometries and working formula are illustrated in Table 3-1 [58]. The pressure driven flow mode devices include dampers, shock absorbers etc., however, very limited researches have been reported. The operating shear rate in these devices is much higher ( $\sim 2 \times 10^4 \text{ s}^{-1}$ ) than that of conventional direct-shear devices, which operate at a nominal shear rate of few thousands ( $\sim 10^3 \text{ s}^{-1}$ ). The third mode of operation is known as biaxial elongational flow mode and it is utilized only in high force applications. In this thesis, all magnetorheological measurements under transient shear (rotational) and oscillatory modes were performed in a direct shear mode commercial rotational rheometer (Anton Paar MCR Physica<sup>®</sup> 301 and 501) with magnetorheological attachment (MRD 170<sup>®</sup>). The Parallel plate system with plate diameter of 20 mm and plate gap of 1 mm was used for all measurements. The magnetic field was generated perpendicularly with respect to the direction of flow with the help of

	Shear stress	Shear rate	Strain	Viscosity
Concentric Cylinder	$\frac{M}{(2\pi R_{ave}^2 h)}$	$\frac{2\Omega R_1^2 R_2^2}{r^2(R_2^2 - R_1^2)}$	$\frac{\theta R_{ave}}{R_2 - R_1}$	$\frac{M(R_2^2 - R_1^2)}{4\pi h \Omega R_1^2 R_2^2}$
Parallel Plate	$\frac{M}{2\pi R^3}$	$\frac{\Omega R}{h}$	$\frac{R\theta}{h}$	$\frac{\pi \Omega M R^4}{2h}$
Cone and Plate	$\frac{3M}{2\pi R^3}$	$\Omega / \alpha$	$\frac{\theta}{\alpha}$	$\frac{3\alpha M}{2\pi R^3 \Omega}$

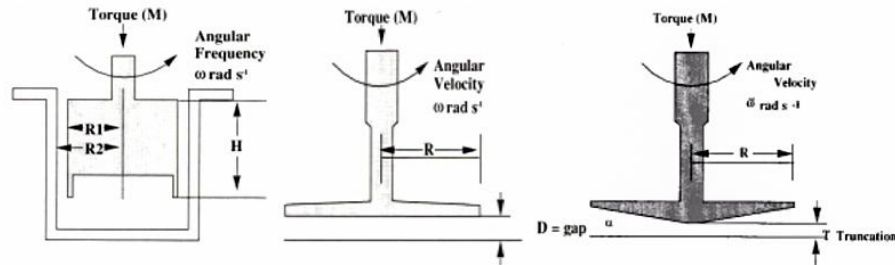


**Table 3-1** (Top) equations of rheological parameters for different geometries:  $M$  is the torque,  $h$  is the height,  $R$  is the radius,  $\Omega$  is the angular velocity,  $\theta$  is the angular displacement and  $\alpha$  is the cone angle. Bottom, types of different geometries: from left, concentric cylinder, parallel-plate and cone-plate [58].

a concentric electromagnet. For our measurements, magnetic field was varied from 0 to 1.2 T, depending upon the requirement. Ramp-up stress controlled or strain-controlled experiments are generally performed under torsional shear flow to measure rheological and MR parameters. The resulting yield stresses are calculated by extrapolation at low-shear rates from shear stress-shear rate flow curves. Time-dependent shear flows have also been investigated in terms of stress increment, stress relaxation under constant shear rate, retardation (creep), strain relaxation and small angle oscillatory strain (SAOS) tests under constant angular frequency. Beyond the yield point, an MR sample shows irreversible plastic deformation in response to the applied stress. Below that yield stress point, a part of time-dependent strain is recovered when the applied stress is pulled out. This measurement provides significant knowledge about elastic behavior of MR fluids under operating conditions. The measuring system of an Anton Paar Physica MCR<sup>®</sup> series rheometer contains three components: the mechanical drive system, electronic data acquisition system and processing and corresponding software packages (RheoPlus<sup>®</sup> Rheometer software).

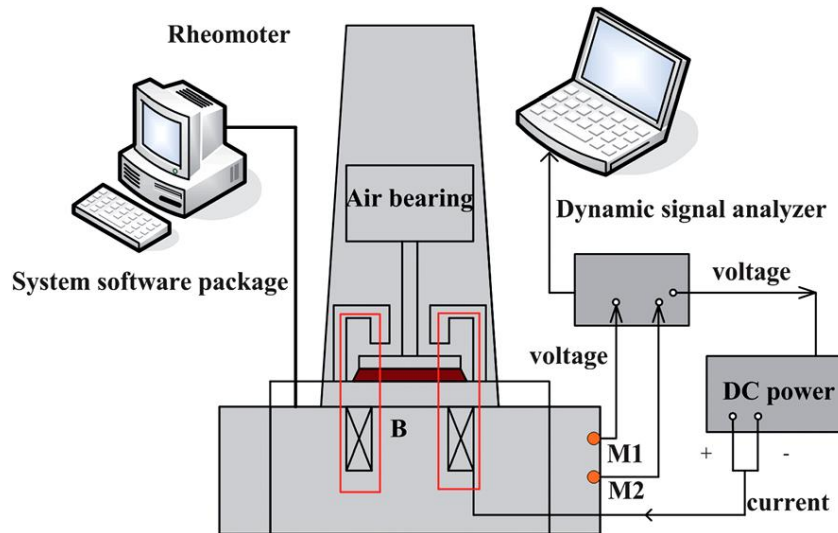


**Figure 3.8** Schematic of an MR rheometer (reprinted from: X. Gong et.al, *Soft Matter*, **8**, 5256–5261. ©RSC 2012)

Fig. 3.8 schematically illustrates the MR rheological measuring system in a standard MCR Rheometer. The magnetic field is generated by Cu coils of 1 mm diameter with 495 turns. The RheoPlus software controls the magnetic field strength across the plates holding the MR sample by adjusting the electric current through the coil. The magnetic field is applied perpendicular to the parallel plate system. Therefore, magnetic field in the gap between two plates is a function of electric current passed through the coil. Volume of MR fluid in the gap is taken primarily as 0.3 mL. The control unit of rheometer automatically demagnetizes after the test was completed. For steady shear measurements, shear rate was varied from  $0.01 - 10^3 \text{ s}^{-1}$  under different magnetic fields. Stress and viscosity relaxation with time was performed under constant shear rate of  $10 \text{ s}^{-1}$ . For oscillatory magnetorheology, amplitude-sweep (constant frequency) and frequency sweep (constant strain) studies were performed in both SAOS and LAOS modes. For temperature-dependent MR studies, rheometer was attached to a JULABO F25<sup>®</sup> temperature controlling unit and various temperatures were maintained to high accuracy. Temperature-dependent magnetorheological studies under steady shear and oscillatory modes were performed at elevated temperatures, in addition to room temperature. Magnetosweep measurements, i.e. viscosity and shear stress variation as a function of magnetic field were also measured under constant shear rate of  $10 \text{ s}^{-1}$ .

# 4

## Chapter 4

### **Investigations on Fe<sub>55</sub>Co<sub>45</sub>-based fluids: structure and magnetorheology**

*In this chapter, we described the characterization of cubic and spherical Fe<sub>55</sub>Co<sub>45</sub> alloy microparticles synthesized by borohydride reduction for use in magnetorheological fluids. Surface morphological studies by scanning electron microscopy revealed well shaped cubic and spherical geometry for the citrate and polymer-stabilized Fe<sub>55</sub>Co<sub>45</sub> alloys (1.2 μm and 0.7 μm, respectively), while the alloy compositions remained nearly the same for both. X-ray diffractions of the as-prepared and annealed samples under various temperatures showed high degree of crystallinity with increasing temperatures of annealing. Studies of D.C. magnetization of the systems revealed that the particles possessed a core-shell type structure, with inner magnetic core having a diameter around 30 nm with a log-normal distribution. Magnetorheological studies were performed with 8 volume% suspensions of as-synthesized particles dispersed in silicone oil (viscosity 30 mPa.s) under different magnetic fields. A microstructure-rheology correlation played a crucial role for cubic-FeCo based MR fluids showing superior magnetorheological properties. Detailed studies of the magnetorheological properties were discussed on these systems for practical use.*

## 4.1 Introduction

As discussed previously most MR fluids utilize carbonyl iron particles (CIP) as dispersed phase. Ferromagnetic binary alloys too can be a worthy choice for the same in terms of their high magnetic permeability and saturation magnetization [59]. FeCo is particularly interesting because of its high saturation magnetization, permeability and low coercivity. An efficient MR fluid contains nearly uniform, oxidation resistant, micron-sized magnetic particles with high permeability. While it is true that larger particles will offer more change in rheological properties per unit magnetic field, the problem with these is that they are unstable against sedimentation, thus gradually losing their properties. This occurs due to large density difference between the carrier fluid and magnetic particles, and various attempts were made to alleviate it [60]. Each of them has a problem of its own. Another important aspect of using FeCo alloy microparticles is their excellent affinity towards surfactants and polymeric additives in wet-chemistry and we can modify their shapes and sizes for stability against sedimentation. Polymer encapsulation of FeCo particles minimizes the density difference between the carrier liquid and particles, thus countering the settling tendency [61].

In this chapter we describe morphology and structural characterization of the microparticles of a FeCo alloy system in two distinct shapes and sizes. Furthermore, microparticles of cubic and spherical FeCo were synthesized by novel ultrasonic-assisted borohydride reduction. Magnetorheological studies were performed to emphasize the structure-magnetorheology correlation in MR fluids containing spherical and cubic microparticles of FeCo with nearly identical compositions.

## 4.2 Results and discussions

### 4.2.1 Morphological characterization of dry powder

#### 4.2.1.1 SEM and EDAX

FESEM images in Fig. 4.1 show the different shapes, sizes and surface textures of sodium citrate and sodium acetate-PEG encapsulated alloy microparticles. While use of polymer and sodium acetate as a capping agent resulted in spherical particles, sodium citrate yielded uniform cuboidal particles. The particles formed were of exclusively cubic or spherical morphologies depending on the precursor contents. Better control of sizes for

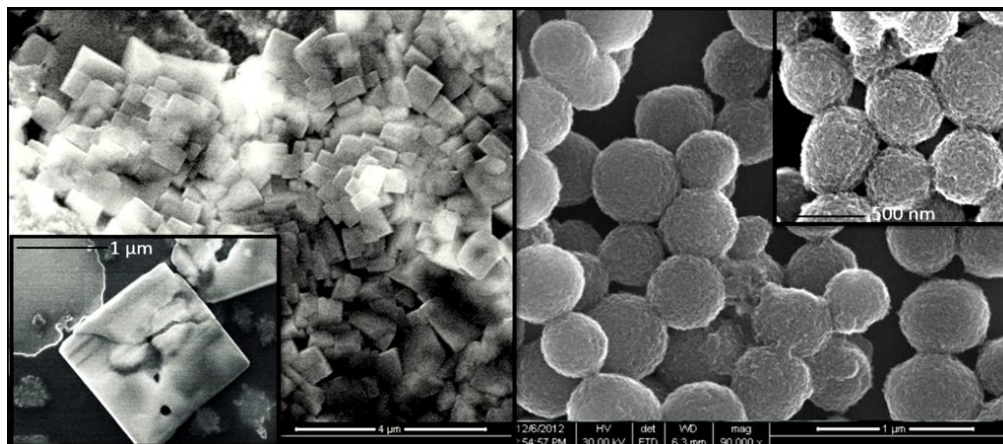


**Figure 4.1** FESEM images of sodium citrate capped cuboidal microparticles (left) and sodium acetate-PEG encapsulated spherical particles.

both samples were found to depend on a number of factors like, choice of capping agents, adjustment of reaction times, compositions and maintenance of proper ratio of metal to capping agents/polymer and borohydride etc. In the present case for the citrate stabilized alloy, average size was measured to be around  $1.2 \mu\text{m}$  and for that of acetate-polymer (PEG) stabilized alloy, it was approximately  $0.7 \mu\text{m}$ . The size distributions of the respective microparticles were shown in Fig. 4.2. These are probably

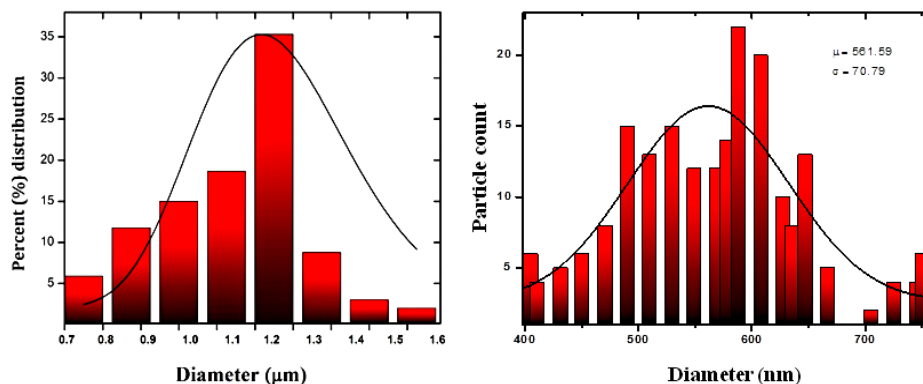


**Figure 4.2** Particle size distribution curves for Na-citrate- $\text{Fe}_{55}\text{Co}_{55}$  (left) and PEG-acetate- $\text{Fe}_{55}\text{Co}_{55}$  microparticles (right) respectively. The fitting lines indicate log-normal

the first reported FeCo particles that were prepared by borohydride reduction technique and grown up to micrometer size particles. The surface roughness in PEG-encapsulated microspheres (Fig. 4.1 right inset) is associated with the polymer-assisted growth process. The Energy dispersive X-ray spectra (EDAX) at five different spots on microparticles of

the samples (obtained from TEM analysis) each reveals nearly identical and homogeneous composition as  $\text{Fe}_{55}\text{Co}_{45}$  (Fig. 4.3).

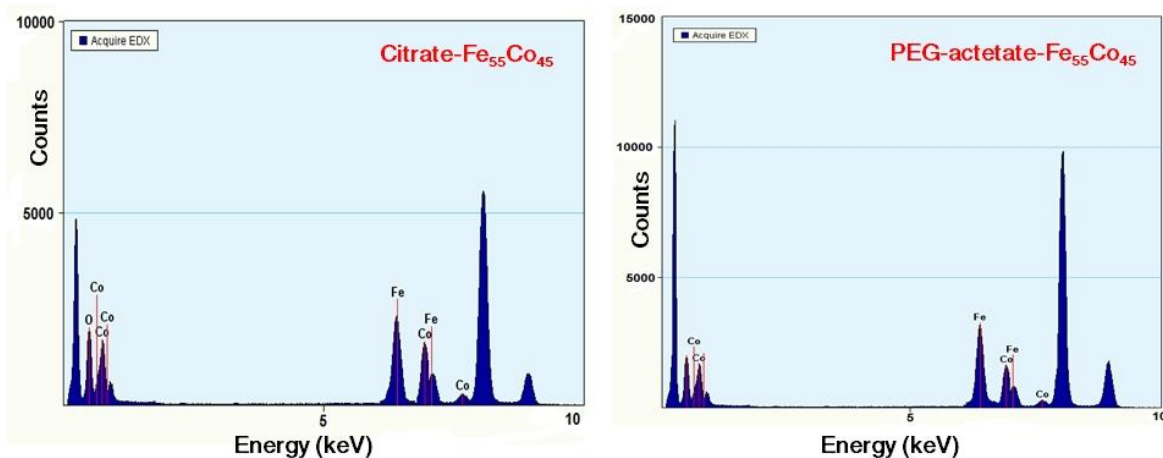


**Figure 4.3** Typical EDAX spectra (as obtained from TEM analysis) of citrate- $\text{Fe}_{55}\text{Co}_{55}$  cubical microparticles and PEG-acetate- $\text{Fe}_{55}\text{Co}_{45}$  microspheres (right), respectively.

#### 4.2.1.2 TEM

Transmission electron microscope images of single particles of citrate-  $\text{Fe}_{55}\text{Co}_{45}$  and PEG-acetate-  $\text{Fe}_{55}\text{Co}_{45}$  are shown below in Fig. 4.4. Extended growth steps in the synthetic process yield micron-sized cubes and spheres of  $\text{Fe}_{55}\text{Co}_{45}$ . The samples are not transparent enough to be visualized in HRTEM. Fig. 4.4A shows low-resolution TEM of free-standing single microcube of citrate-  $\text{Fe}_{55}\text{Co}_{45}$  in which all edges are approximately equal in length. Similarly, TEM micrograph of PEG-acetate- $\text{Fe}_{55}\text{Co}_{45}$  (Fig. 4.4B) also reveals roughly monodisperse nature of microspheres.

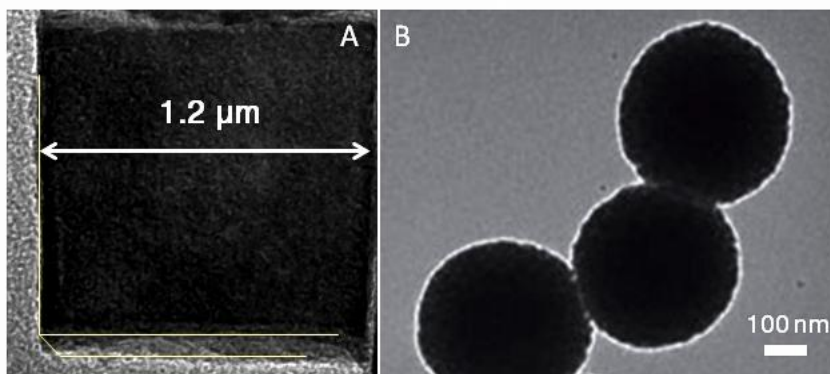


**Figure 4.4** Typical TEM images of citrate- $\text{Fe}_{55}\text{Co}_{55}$  cubical microparticles (A) and PEG-acetate- $\text{Fe}_{55}\text{Co}_{45}$  microspheres (B), respectively.

### 4.2.1.3 X-ray diffraction

Crystal structures of FeCo samples were analyzed by x-ray diffraction patterns shown in Fig. 4.5. For both samples, the  $\alpha$ -FeCo peaks were identified as (110), (200) and (211), indicating a body-centered cubic (bcc) structure characteristic of FeCo alloys (JCPDS card no. 49-1567 and ICDD reference code 00-044-1433). The crystallite sizes for both citrate-Fe<sub>55</sub>Co<sub>45</sub> and PEG-Fe<sub>55</sub>Co<sub>45</sub> samples were calculated using Scherrer equation

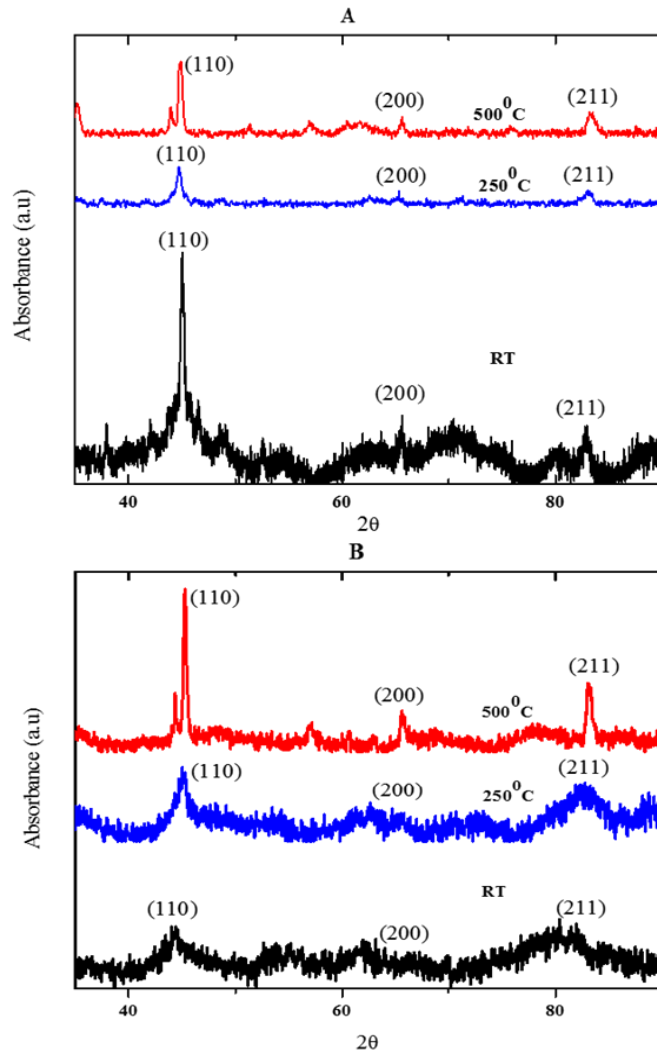


**Figure 4.5** X-ray diffraction pattern of citrate-bound Fe<sub>55</sub>Co<sub>45</sub> (A, top) and acetate-polymer bound Fe<sub>55</sub>Co<sub>45</sub> (B, bottom) samples under various annealing temperatures. Only major peaks were identified.

which states that:  $D = k\lambda/\beta\cos\theta$  where  $D$  is mean crystallite size,  $k$  is shape factor,  $\lambda$  is x-ray wavelength,  $\beta$  is line broadening at half of the maximum intensity (FWHM in

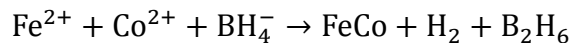
radian) and  $\theta$  is Bragg's angle. The FWHM calculated from (110) peak broadening gives us the crystallite mean size for citrate-Fe<sub>55</sub>Co<sub>45</sub> and PEG-Fe<sub>55</sub>Co<sub>45</sub> as 23 nm and 28.3 nm, respectively. (In XRD we are looking at the metallic core part only, not in the overall microparticle that SEM found. That is why there is a size mismatch between two measured values). In order to get higher crystallinity, the sample pellets of 3 mm diameters were annealed in a TA Q200™ differential scanning calorimeter (DSC). Ramping rate during annealing was 10°C/min and kept at final temperatures for 15 minutes. As is observed, samples at higher annealing temperature are more ordered with sharper peaks. The increasing crystallinity at higher temperatures can be resulted in higher lattice parameters and increased crystallite sizes. The trend is shown in the Table 4-1:

**Table 4-1** various parameters obtained from x-ray diffraction data are given in this table. Average grain size ( $D$ ) and lattice parameter ( $a$ ) of FeCo alloy microparticles are calculated at different temperatures.

<b>Na-citrate Fe<sub>55</sub>Co<sub>45</sub></b>		
Annealing temp. (°C)	Crystallite size, $D$ (nm)	Lattice parameter $a$ (nm)
RT (25°C)	23.0	0.2856
250°C	34.5	0.2858
500°C	42.2	0.2860
<b>PEG-acetate Fe<sub>55</sub>Co<sub>45</sub></b>		
RT (25°C)	28.3	0.2857
250°C	32	0.2858
500°C	48.6	0.2861

#### 4.2.2 Structure and growth mechanism

In the synthesis system, Co (II) and Fe (II) salt were reduced by sodium borohydride in aqueous media which can be explained by electromotive forces (*emf*) [62]. The possible reaction scheme can be formulated as follows:



The evolution of microparticles from a solution follows three distinct steps: nucleation, seed generation followed by growth of seed to form nanoparticles [63]. An extended growth step can ensure bigger microparticles and hierarchical morphologies. The steps in synthesis of FeCo microstructures are illustrated in Fig. 4.6.

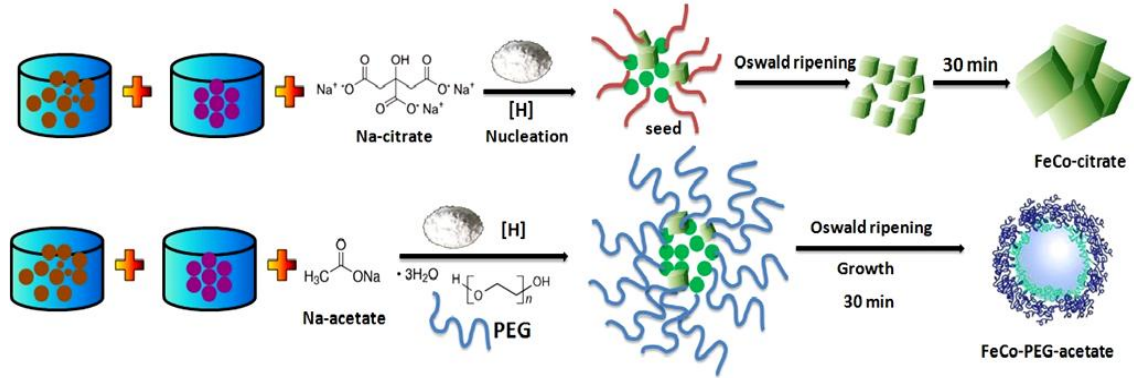


**Figure 4.6** Schematic of the structural evolution of citrate-Fe<sub>55</sub>Co<sub>55</sub> cubical microparticles and PEG-acetate-Fe<sub>55</sub>Co<sub>45</sub> microspheres from precursor solutions.

The borohydride reduction of metal precursors is almost instantaneous, i.e. reaction time is considerably shorter compared to other reduction methods. So, higher concentration of nuclei at the first stage of process can be explained by high rate of nucleation prior to dissolution of metal salts. Nucleation is followed by the formation of seed nanoparticles. At high concentrations of metal salts the supersaturation factor  $\lambda(t)$  is higher. Therefore, according to the Adamson equation for homogeneous nucleation, the nucleation rate ( $k_n$ ) will also be higher. The equation is as follows [64]:

$$k_n(i, t) = \begin{cases} 0, & i < n^* \\ ik_0 \exp\left(\frac{-16\pi\sigma^2 v_m^2}{3(k_B T)^2 (\ln \lambda(t))^2}\right), & i \geq n^* \end{cases} \quad (4.1)$$

where  $\sigma$  is the interfacial tension between solid nucleus and surrounding liquid,  $v_m$  is the volume of one precipitate molecule,  $\lambda$  is the supersaturation ratio of liquid product molecules,  $i$  is the number of liquid product molecules in a drop and  $n^*$  is the critical number of liquid product molecules in a nucleus. Thus at higher concentrations of metal ions, more nuclei will be formed. Therefore the growth stage which is followed by the addition of generated molecules is slowed down and the resulting nanoparticle size is reduced [65]. Similarly at lower concentrations of metal precursors, the number of formed nuclei is lower providing more product molecules to contribute in the growth of

nanoparticles leading to larger microparticles and hierarchical morphologies. In order to ascertain the fact that growth of nanoparticles was only possible by diffusion of product

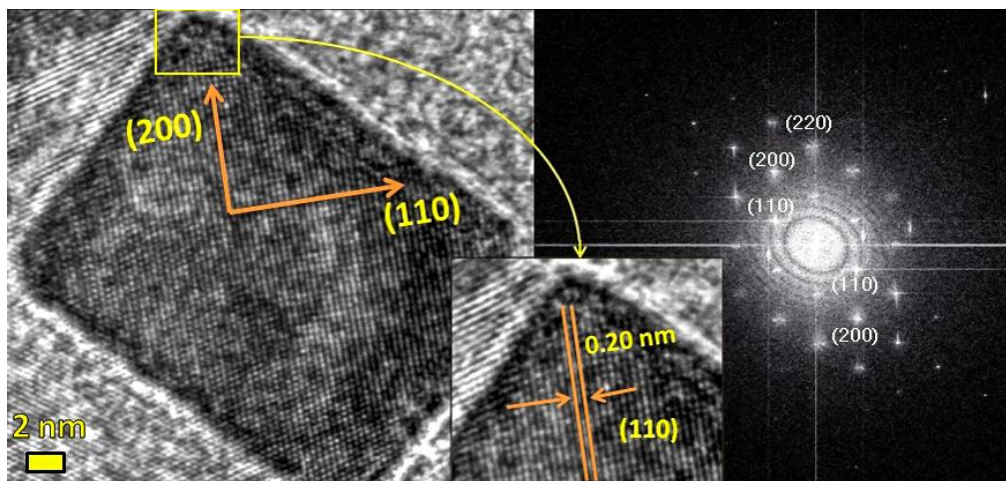


**Figure 4.7** HRTEM image of citrate-Fe<sub>55</sub>Co<sub>55</sub> nanocubes after 10 minutes of the start of reaction. The size of nanocubes is approx. 30 nm. In the right, FFT image of the same is shown. Inset, magnified portion of the edge of nanocube with preferred growth plane is illustrated.

molecules onto the surface of seed particles until they bound to favored or ‘habit’ planes, we performed HRTEM analysis of the nanoparticles formed at 10 minutes since the reaction had started [66]. The Fig. 4.7 shows HRTEM image of a single nanocrystal of citrate-FeCo with periodic lattice fringe spacing of 0.20 nm which correspond to interplanar spacing between (110) planes of FeCo alloys. The fast-Fourier transform (FFT) pattern for the nanocrystal is also shown and indexed to corresponding crystal planes of (110), (200) and (220). The preferred growth direction for nanoparticles is therefore, along (110). Na-citrate and PEG acted as capping agents and bounded to this particular habit plane, favoring the periodic growth as shown in Fig. 4.7. Since the concentration of metal precursor was low, the growth step was extended to form larger micron sized cubic particles for citrate-FeCo. Although the stages of up to seed generation were similar for both materials (Fig. 4.6), however, PEG-FeCo tends to appear roughly spherical in size owing to the fact that excess polymer concentration in precursor might have influenced the final geometry of particles.

#### 4.2.3 Magnetization studies

Variation in saturation magnetization values for the alloyed powders was observed in the room temperature hysteresis curves shown in Fig. 4.8. It was observed that encapsulation

of polymer on the Fe<sub>55</sub>Co<sub>45</sub> surface seemed to have affected saturation magnetization [67] of acetate-PEG capped alloy ( $M_s \sim 105 \text{ emu/g}$ , coercivity  $\sim 324 \text{ Oe}$ ) as compared to the

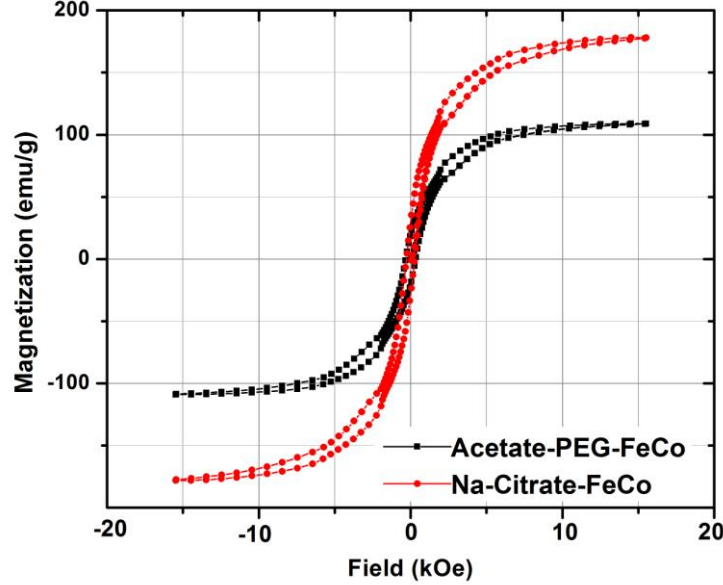


**Figure 4.8** Room temperature magnetic hysteresis loops (M-H) of the two citrate-capped FeCo system ( $M_s \sim 177.5 \text{ emu/g}$ , coercivity  $\sim 264 \text{ Oe}$ ). Analysis of magnetization was performed following reference [68], wherein the approximation to the approach to saturation magnetization of Langevin's function  $L = \coth b - \frac{1}{b}$  (where  $m$  is the particle magnetic moment  $= M'_s V$ ,  $M'_s$  is saturation magnetization of bulk and  $M_s$  is the saturation magnetization of fluid, such that  $M_s = \phi M'_s$  where  $\phi$  is volume fraction) was used to get an idea of the particle size, in this case it would mean the size of the magnetic component. The expression for mean diameter ( $D_v$ ) for magnetic core of a particle derived by Chantrell *et al.* [68]:

$$D_v = \left[ \frac{18k_B T}{\pi M'_s} \sqrt{\frac{\chi_i}{3\phi M'_s H_0}} \right]^{\frac{1}{3}} \quad (4.2)$$

$$\sigma = \frac{\left[ \ln \left( \frac{3\chi_i}{(\phi M'_s \cdot 1/H_0)} \right) \right]^{1/2}}{3} \quad (4.3)$$

where  $\sigma$  is standard deviation. The quantity  $1/H_0$  is calculated from the intercept of  $M$  vs.  $1/H$  curves at  $M = 0$ . We calculated that and the fittings show that the citrate particles have a core size of 26 nm, with  $\sigma$  value of 1.20 nm, while the other has a core size of 29 nm, with the  $\sigma$ -value of 1.15 nm. This assumes a log-normal distribution of the particle sizes, which is found to be generally true for these types of particles [69]. Since there was no direct measurement on the core-shell particles, we do not contest this claim. It is now possible to understand the formation morphology of the particles, when the particles are smaller, these were found to take spherical shapes (coming from the roughly spherical core) whereas in the larger grown particles, the crystal structure of the shell component would show up. The citrate particles are bigger, so particles are cuboidal due to preferential growth along (110). In the other case, the particles are smaller, as well as the fact that there was a soft component from PEG, allowed it to retain the roughly spherical shape.

#### **4.2.4 Magnetorheological characterization**

##### *4.2.4.1 Preparation of MR fluids*

Preparation of 8 volume-% MR fluids involved the mixing of sodium citrate-capped  $\text{Fe}_{55}\text{Co}_{45}$  and sodium acetate-PEG couple encapsulated  $\text{Fe}_{55}\text{Co}_{45}$  microparticles into calculated volumes of silicone oil (30 mPa.s, density  $0.761 \text{ g/cm}^3$ ) by mechanical stirring following ultrasonic agitation for a few hours to ensure complete dispersion of aggregates. Silicone oil was chosen as a matrix fluid for its low off-state viscosity and chemical inertness. The densities of microparticles were measured by standard pycnometry using specific gravity bottles, for citrate-  $\text{Fe}_{55}\text{Co}_{45}$  and acetate-PEG- $\text{Fe}_{55}\text{Co}_{45}$  particles, these were  $5.8 \text{ g/cm}^3$  and  $4.0 \text{ g/cm}^3$  respectively. Lower density of PEG- $\text{Fe}_{55}\text{Co}_{45}$  can be attributed to polymer-encapsulation.

##### *4.2.4.2 Steady shear magnetorheology: particle shape and size dependence*

To investigate the combinatorial effect of particle's size and morphology on rheological properties, two different MR fluid systems of same concentration (8 vol %) were prepared using both types of particles. Steady shear magnetorheological responses were recorded for each of these MR suspensions as a function of shear rate under varying magnetic fields from 0 to 1.2 T at 40°C and shown in Fig. 4.9. The curves were definitely

non-linear, thus implying that the behavior is plastic. Dynamic shear stresses were found to better follow the nonlinear Herschel-Bulkley model,  $\tau = \tau_0 + k\dot{\gamma}^n$  where  $\tau$  is the shear stress,  $\dot{\gamma}$  the shear rate,  $\tau_0$  the yield stress (i.e. at zero shear velocity), and  $k$  and  $n$  are regarded as model factors. This behavior is plotted as lines in the curves, and the parameters are tabulated in Table 4-2.

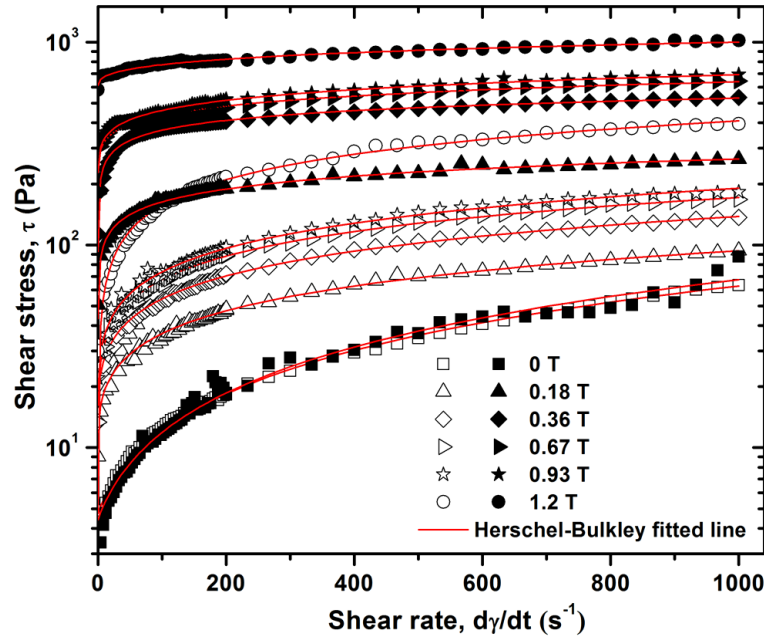


**Figure 4.9** Shear stress vs. shear rate curves under different magnetic flux density for 8 vol% MR fluids containing Na-citrate-Fe<sub>55</sub>Co<sub>45</sub> (closed symbol) and Na-acetate-Fe<sub>55</sub>Co<sub>45</sub> particles (open symbol). Lines are fit to the Herschel-Bulkley equation.

Examination of the tables shows some surprises. While the fits are reasonably good (see Fig. 4.9), the individual parameters are not very consistent. In particular, the non-monotonic behavior of  $\tau_0$  in case of citrate-FeCo particles is disturbing, as also some of the other values of  $k$  and  $n$ . A close inspection of the data and the fit reveals a probable cause. Firstly, the shear behavior near the starting field is not the same for all, thus upsetting the values of  $\tau_0$ . Then the behavior under high shear rate and magnetic fields is not monotonic, thus the fit is not possible with a simple power law such as Herschel-Bulkley. The acetate-PEG sample was better behaved; at least the exponent has gradually fallen from the zero field value, as expected. The trend of  $k$  is also along the expected line. But we see that the yield stress is a problem.

**Table 4-2** Rheological behavior of the MR fluids under different magnetic fields at 40°C. The individual Herschel-Bulkley fitting parameters are shown at different magnetic fields.

<b>Na-citrate Fe<sub>55</sub>Co<sub>45</sub></b>			
Magnetic field (T)	Yield stress, $\tau_0$ (Pa)	Consistency, $k$ (Pa. s <sup>n</sup> )	$n$
0	4.4±1.17	0.1±0.04	0.92±0.06
0.18	11.2±6.42	54.0±4.58	0.22±0.01
0.36	-96.7±29.55	255.6±26.34	0.13±0.01
0.67	186.2±15.28	75.1±9.83	0.26±0.01
0.93	181.6±14.51	83.6±9.29	0.26±0.01
1.2	599.5±10.11	33.2±4.64	0.36±0.02
<b>PEG-acetate Fe<sub>55</sub>Co<sub>45</sub></b>			
0	4.7±0.25	0.1±0.01	0.89±0.01
0.18	11.2±1.40	2.4±0.35	0.51±0.02
0.36	15.0±1.21	4.0±0.33	0.50±0.01
0.67	14.1±1.47	6.2±0.45	0.47±0.01
0.93	17.5±2.73	5.9±0.76	0.49±0.02
1.2	-4.8±5.43	24.8±2.10	0.40±0.01

We think that the difference in behavior was more due to the shape and size of the two constituents since the citrate particles are bigger and have less symmetry (cubic rather than spherical) – also presumably have harder shell than the PEG coatings, their yield stresses and viscosity coefficients are bigger – meaning the resistance to shear was larger. This was also expected since the square shapes can make a stronger chain by virtue of larger contact area among the cubes than that is possible with the spherical particles. Coupled with the fact that the  $n$  coefficients for all of them under external fields are not so different among themselves as well as being quite low, it means that these particles are more strongly affected by magnetic field and that prevents them from acting as simple

rheological fluids. This is also borne by the fact that the  $M_s$  for this system is higher than that of the other [70]. This latter system is better behaved. This type of behavior we have also encountered in PVC-Fe<sub>3</sub>O<sub>4</sub> composite systems, as described in chapter 7. That system was magnetically even softer, but the Herschel-Bulkley fits started to deteriorate with lower field values, since the curves started drooping at higher fields and shear rates [71].

To appreciate the magnetic contribution, we tried to fit the data to the model proposed by Ginder *et al.* [49]. Since the rheological fits were not satisfactory with Herschel-Bulkley model, we used the previously described linear Bingham plastic model,  $\tau = \tau_{ys} + \eta\dot{\gamma}$  where  $\tau$ ,  $\tau_{ys}$ ,  $\eta$  and  $\dot{\gamma}$  represent shear stress, dynamic yield stress, viscosity and shear rate, respectively. Obviously the fitting has to be done only at the higher end of the graph (since it cannot account for the initial rise), and the limits to fitting points are more subjective than objective. However, doing that as carefully and as unbiased as possible, we arrive at the following values of the parameter  $\tau_{ys}$ , given in Table 4-3 below:

**Table 4-3** yield stresses ( $\tau_{ys}$ ) of the two systems, from Bingham model.

Magnetic field ( <i>Tesla</i> )	Yield stress, $\tau_{ys}$ ( <i>Pa</i> )	
	Na-citrate Fe <sub>55</sub> Co <sub>45</sub>	PEG-acetate Fe <sub>55</sub> Co <sub>45</sub>
0.00	9.96	6.70
0.18	181.17	47.43
0.36	391.39	69.86
0.67	462.06	92.52
0.93	517.07	114.36
1.20	764.63	228.24

Now, there are three regions for the Ginder's model, wherein the  $\tau_{ys}$  will behave as (a)  $\tau_{ys} \propto \phi\mu_0H^2$  at very low applied field ( $\phi$  is particle volume fraction and  $\mu_0$  is permeability of free space,  $4\pi \times 10^7 H/m$ ), (b)  $\tau_{ys} = 2.45\phi\mu_0M_s^{1/2}H^{3/2}$  at an intermediate field range i.e. field is lower than is required to saturate magnetically ( $M_s$  is

saturation magnetization) and (c)  $\tau_{ys}^{sat} = 0.086\phi\mu_0M_s^2$  at sufficiently high field strength when particles saturate magnetically. The result of our fittings is shown in Fig. 4.10. The

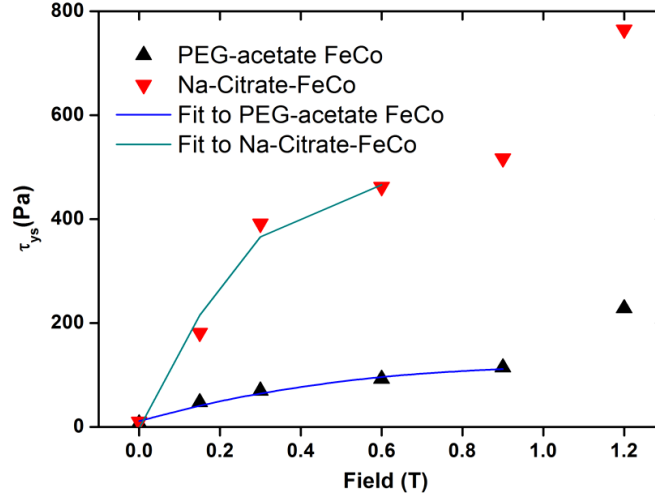


**Figure 4.10** fitting of Ginder’s model to the yield stress data for the two systems.

parabolic fits are found to be better in case of PEG-acetate particles, one possible reason is that these have spherical morphology – the shape that was used in constructing the Ginder’s model. However, while the fits at low field values may not be bad (there are too few data points to rigorously justify the merits of the fit), the uprisings at the higher end show that the systems had entered a different field induced regime. Since we know from the law of approach to saturation that the systems were not saturated even at 1.2 T, the uppermost field available in the rheometer, we tried to fit for the intermediate region. However, in neither case the fits produced a good  $\tau_{ys}$  and so we abandoned the procedure any further. The reasons of the failure may be that there are other effects [72] and forces, besides the magnetostatic forces, that come into play in the present system. Therefore, Ginder’s description of sub-quadratic dependence of yield stress on magnetic field in the MRFs containing particles with complex surface properties with geometries other than spheres is insufficient to follow the observed changes.

#### 4.2.4.3 Sedimentation stability of MR fluids

Stabilities of the MR fluids against sedimentation, in the absence of external magnetic field, are plotted in Fig. 4.11. The sedimentation ratios of the MRFs were measured by

placing the fluids in a graduated cylinder and using the relation,  $R = \frac{y}{x+y}$  where  $x$  and  $y$  denotes the vertical length of supernatant and turbid layer, respectively. The curves seem to follow an exponential decay law, i.e.  $R \sim \exp(-t/\tau)$  where  $\tau$  is the time constant. In case of the citrate coated particles, the  $\tau$  is 3.9 hrs and in the other case  $\tau$  is 2.7 hrs. Since the plot is of the length of the clear layer, this means that the citrate particles settled down quicker. This was also expected, for the apparent density of the citrated particles is  $5.8 \text{ g/cm}^3$ , which is greater than that of the other at  $4.0 \text{ g/cm}^3$ . It is interesting to note that the whole 40 hrs worth of data would still fit much better than a power law that would have dominated the long time relaxation, this is probably due to rather narrow dispersion in size of our particles.

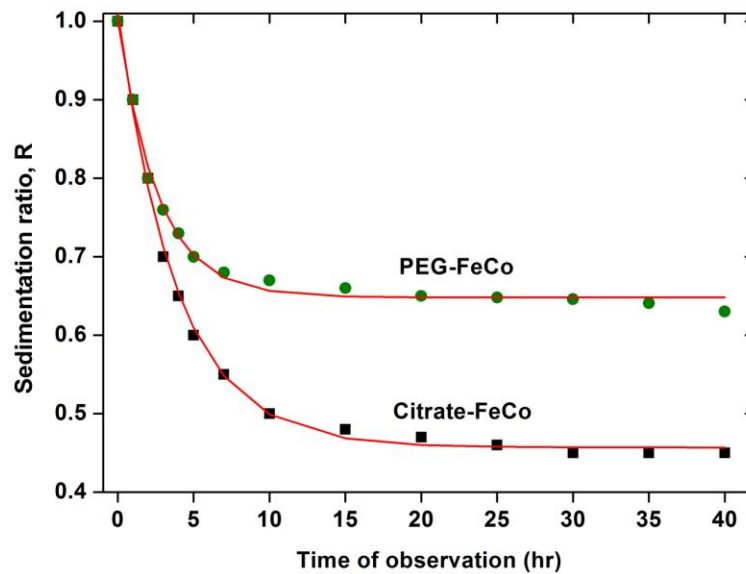


**Figure 4.11** Sedimentation ratio,  $R$  vs. time dependence of 8 vol% MR fluids based on Na-citrate stabilized FeCo particles (square) and Na-acetate/PEG encapsulated FeCo (sphere) particles. Red lines are from fitting equation (exponential decay).

### 4.3 Conclusion

In this chapter, we discussed the structure and morphology of  $\text{Fe}_{55}\text{Co}_{45}$  microparticles with different shapes, size and magnetic properties. The materials were synthesized by novel ultrasonic-assisted borohydride reduction at room temperature. The extended growth steps in presence of Na-citrate, Na-acetate and PEG ensured larger particles with

cubic and spherical geometries. The structure-rheology correlation was investigated in the MR fluids containing the microparticles. Individual fitting parameters in Herschel-Bulkley model were not following regular trends. The inter-particle interaction was affected due to shape, size, magnetization and surface morphology of constituent particles. The Ginder's law of sub-quadratic dependence of yield stress on magnetic field was also insufficient to explain the trend due to complex interaction among the particles of varied shapes and sizes. Finally, PEG-FeCo based MRF showed enhanced stability from settling as polymer encapsulation reduced the bulk density of the same.

5

## Chapter 5

### NiCo nanoflowers and nanoplatelets: structure, morphology and rheology

*In this chapter, we discussed the structure and morphologies of hierarchical flower-like particles and monodisperse NiCo nanoplatelets synthesized by both polyol and hydrothermal reductions. The growth mechanisms of nanoflower and platelet-like nanoparticles from precursors were described with reference to the SEM and TEM analysis. We further studied the dependence of composition of individual metal components, basicity of reacting media, effect of polymer and surfactants on to the structure, surface and magnetic properties of the nanostructures. Furthermore, in order to emphasize a shape-rheology correlation, magnetorheological studies were performed with suspensions containing NiCo nanoflowers and nanoplatelets. The effect of nanoparticle substitution in MR fluids were studied in ferrofluid-based MR fluid containing NiCo nanoflowers.*

#### 5.1 Introduction

The NiCo binary alloy is an important member of transition metal alloys due to its diverse potential applications in microwave absorption, magnetic resonance imaging contrast agents, magnetic recording devices, magneto-optics, ferrofluids and magnetorheological (MR) suspensions etc. [73-76]. The diverse application ranges of NiCo-based nano- and microparticles originate in their wide ranging catalytic and soft magnetic properties, in addition to their enhanced mechanical properties compared to Co and Ni. The NiCo nanoparticles when encapsulated with polymer will ensure enhanced sedimentation stability of the MR fluids. This is another very desirable property. Additionally, NiCo nano- and microparticles can be synthesized by various wet chemical reduction methods and accordingly, magnetic and surface properties can be tuned. In addition to single domain nanoparticles, a wide range of structure and magnetically anisotropic microparticles of NiCo alloy system can be synthesized by polyol and

hydrothermal reduction methods. This includes hierarchical flowers and microclusters, microspheres, nanoplatelets, nanorod and microfibers etc [76-78].

Hierarchical ferromagnetic microparticles of NiCo have often been regarded as an important class of functional materials due to their enhanced surface properties and varied range of architecture, in comparison to their single domain, discrete counterparts [79,80]. Hierarchical structures originate from the self-organization of nanoscale building blocks through various chemical or physical interactions [81]. However, the prediction of the final structures from self-assembly of low dimensional nanoscale building blocks is still not possible and it depends on number of parameters, e.g. concentration of metal ions in precursor, types of surfactants/polymer and reducing agents etc [82]. One-pot synthesis of hierarchical nanostructures in presence of organic surfactants and polymer is one of most well-documented method that effectively combines the nanometric building blocks to the formation of hierarchic structures with desired architecture [83]. In this method, polymer or surfactant control anisotropic growth of nanomaterials by chemically absorbing onto the facets of growing nuclei. One of most successful ‘bottom-up’ approaches to synthesize hierarchical nanostructures utilizes liquid polyol as both solvent and reducing agent [84,85]. In the past two decades, there has been significant number of researches on polyol syntheses of functionalized magnetic nanomaterials with variable morphologies. In addition to study the effect of hierarchical nanoflower particles on MR properties, we have also investigated the structure-magnetorheology correlation for the hexagonal NiCo platelet-based MR fluids. The monodisperse hexagonal nanoplatelets of NiCo alloy can be synthesized by hydrazine-mediated hydrothermal reduction at elevated temperature.

In this chapter, we discussed the morphology and growth mechanisms of hierarchical NiCo nanoparticles (nanoflowers) and monodisperse NiCo nanoplatelets. The structure-dynamics correlation studies in MR fluids containing the flower-particles and nanoplatelets were demonstrated in transient and oscillatory magnetorheological measurements under various conditions, e.g. magnetic field, particle volume fraction, ferrofluids as carrier liquids etc.

## **5.2 Structure and morphology of particles**

## 5.2.1 SEM and TEM studies

### 5.2.1.1 $Ni_xCo_{1-x}$ flower-like microparticles

The morphologies of as-prepared NiCo flower-like nanostructures in presence of Jeffamine<sup>®</sup>, CTAB and PAA are shown with low-magnification FESEM images shown in Fig. 5.1. The structural evolution of rose-like nanoparticles for NiCo-Jeffamine was studied by analyzing particles in FESEM at various time intervals during preparation (Fig. 5.2). At the early stage of reaction, the sample was smooth spherical with about  $\sim 450$  nm in size. As the reflux time was increased to 90 minutes, tiny ridges of nanosheets were observed on the surface as if the sheets were curved out of surface. The size of particle at this time increased to  $\sim 650$  nm. At final stage after 3 hours of reaction, nanosheets grew larger to form rose-like nanostructures of  $\sim 700$  nm in size. The typical thickness of nanosheets was about 30 nm and the sheets were connected to each other through the core. The overall yield of NiCo-Jeffamine nanoflowers was calculated to be as high as 86%. TEM image of a single nanoflower, shown in Fig. 5.3, further revealed that the lattice spacing was 0.205 nm, corresponding to (111) plane of cubic (*fcc*) NiCo alloy crystals [86]. Selected area diffraction (SAED) pattern for the marked region indicated polycrystallinity in sample.

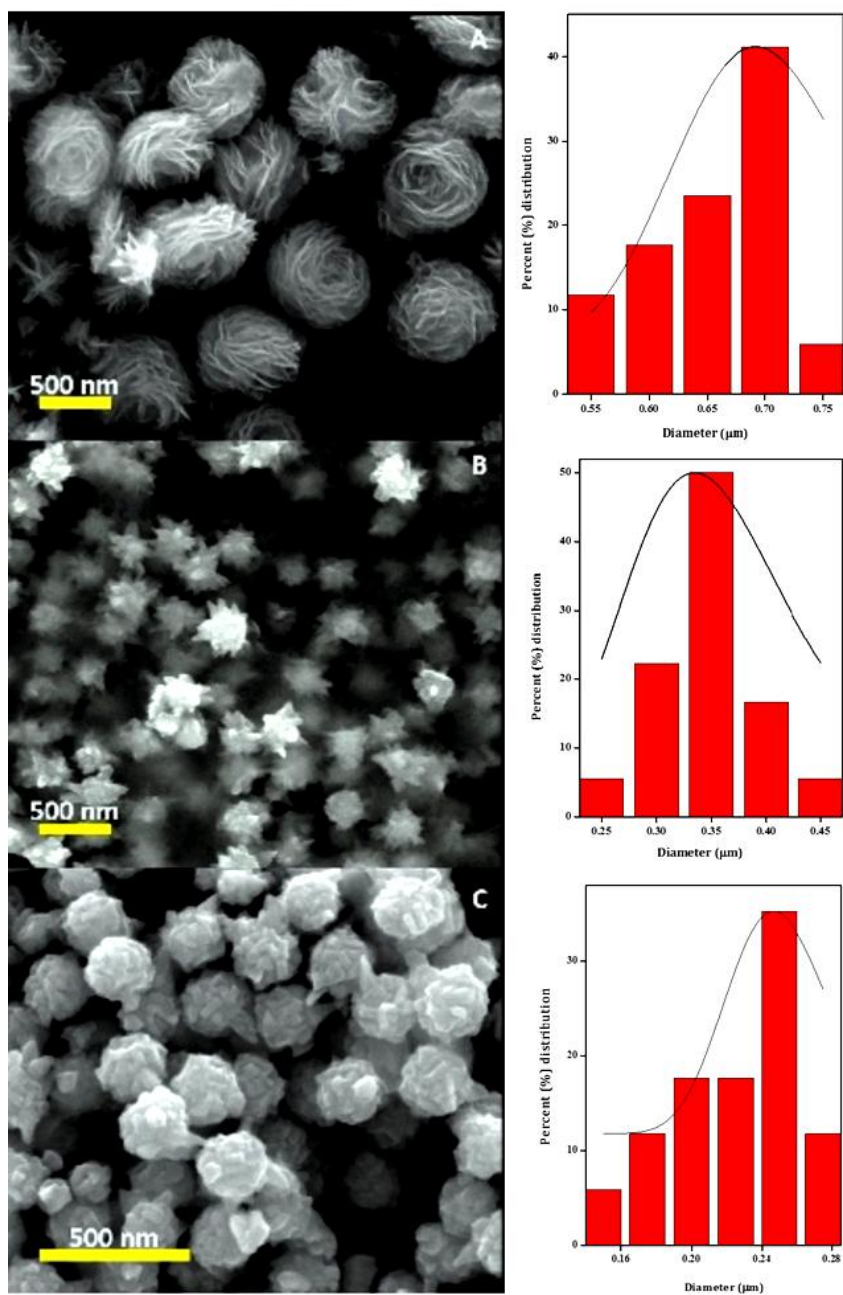


**Figure 5.1** Flower-like hierarchic nanostructures obtained in 1, 2-propanediol using amphiphilic polymer Jeffamine (A), poly-acrylic acid, PAA (B) and surfactant CTAB (C). Corresponding histogram size distributions of particles are shown at right.

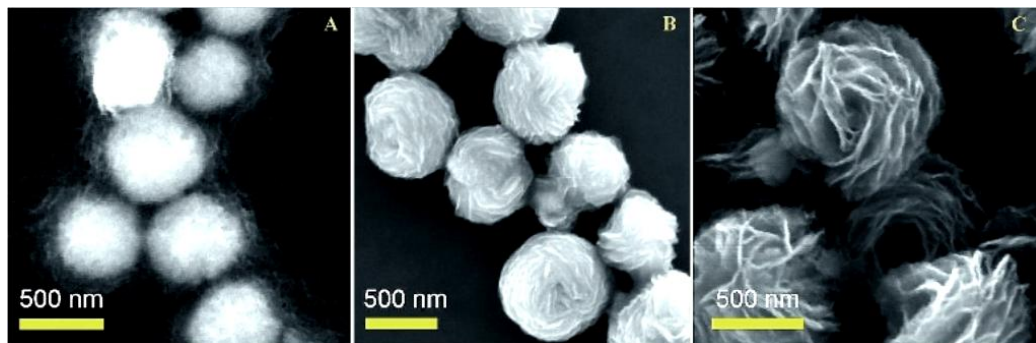


**Figure 5.2** FESEM images of Jeffamine-NiCo nanoflower intermediates during refluxing after different reaction times: (A) 30 min, (B) 90 min, and (C) 180 min.

EDAX analysis confirmed the compositions for all samples and it was shown that final compositions varied only slightly from initial molar composition of respective metal salts.

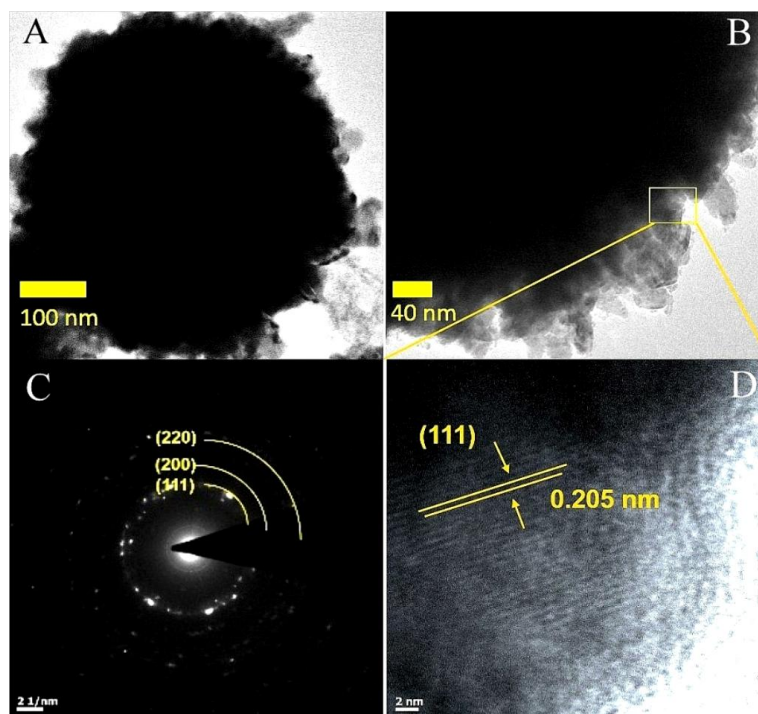


**Figure 5.3** TEM micrograph and SAED of a NiCo hierarchic flower (A-D in order of increased magnification).

### 5.2.1.2 NiCo nanoplatelets

Morphology, average size and composition of NiCo hexagonal nanoplatelets were confirmed by FESEM and TEM analyses. Fig. 5.4 (A & B) illustrates the low and high magnification FESEM images along with particle size distribution histogram. The mean

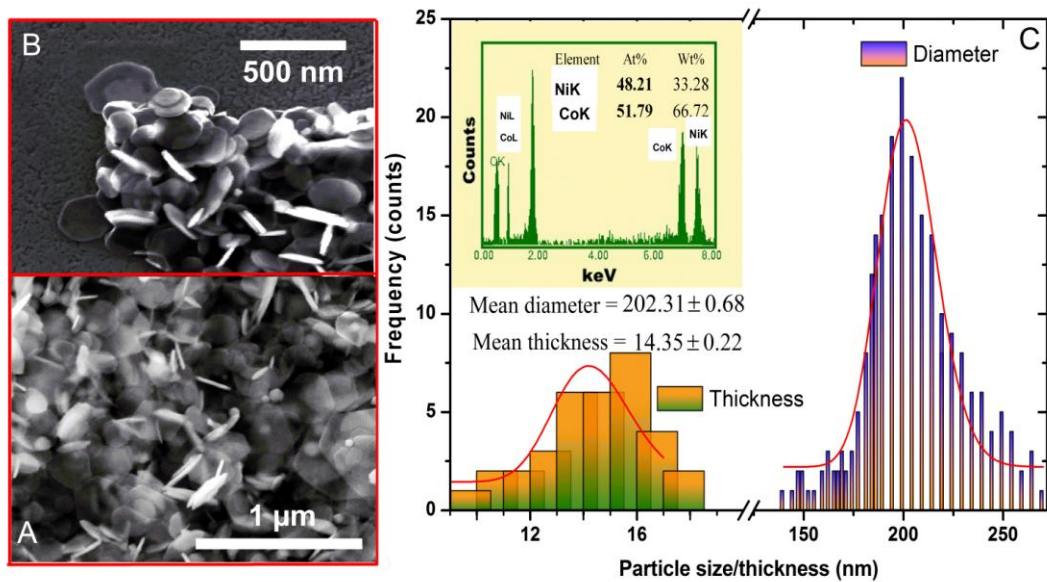


**Figure 5.4** Clockwise from left: (A & B) low- and high resolution FESEM images of NiCo hexagonal nanoplatelets, (C) average size (diameter) and thickness distribution curves of nanoplatelets and (C, inset) EDX spectra of the sample confirming the 1:1 composition.

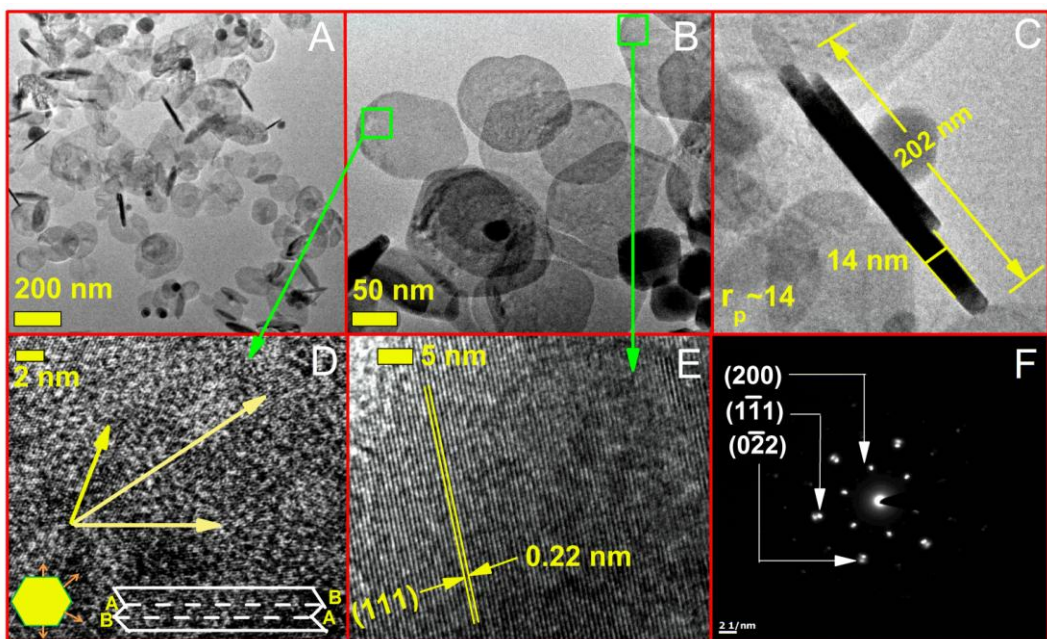


**Figure 5.5** (A, B) Low and high magnification TEM images of NiCo nanoplatelets, (C) cross section of individual nanoplatelet with aspect ratio of 14, (D, E) HRTEM of selected spots with schematic of growth direction, and (F) selected area diffraction pattern (SAED) of nanoplatelets.

radius and thickness of nanoplatelets are measured assuming log-normal distribution and found to be 202 nm and 14.3 nm, respectively. It is evident that the distribution is nearly monodisperse with distinguished hexagonal shape of platelets. The EDAX spectra in Fig.

5.4C shared that the nanoplatelets attained compositional homogeneity with nearly 1:1 Ni and Co atomic ratio. Similar structural characters were also reflected in the TEM images of Fig. 5.5 in which individual nanoplatelets were viewed both front and sidewise. The typical aspect ratio ( $r_p$ ) of plates was found to be 14. The more detailed structural features were extracted from HRTEM and SAED analysis (Fig. 5.5D, E, and F). The HRTEM of selected area at the top of a single particle indicated a lattice with spacing of 0.22 nm which was in good agreement with typical lattice spacing of (111) planes in an *fcc* crystal [87]. The schematic of epitaxial growth of nanoplatelets are shown in Fig. 5.5D. For an *fcc* crystal it is known that favored growth direction is along (111) planes in order to minimize the anisotropic energy. Considering the 6-fold rotational symmetry of SAED pattern, it can be concluded that the hexagonal faces of platelet are represented by (111) planes. From SAED (Fig. 5.5F), three sets of diffraction spots were isolated: the inner spot with lattice spacing 0.22 nm represented the (111) plane whereas the outer spot with d-spacing of 0.14 nm was typical of (220) characteristic to *fcc* NiCo. Therefore, HRTEM and SAED justified that the top and bottom faces of hexagon were bound by (111) planes and the six edges (side face) by (111) and (100) planes. The detailed growth mechanism is discussed in the proceeding section 5.2.3.

### 5.2.2 X-ray diffraction studies of NiCo nanoflowers and nanoplatelets

The crystal structures and phases of the resulting particles were determined by powder x-ray diffraction as shown in Fig. 5.6(A) and Fig. 5.6(B). The diffraction data of NiCo-Jeffamine nanostructures (ranging from  $2\theta = 35^\circ$  to  $80^\circ$ ) for various  $[\text{Ni}^{2+}]: [\text{Co}^{2+}]$  ratios are shown in Fig. 5.6(B). The featured peaks at  $2\theta = 44.6^\circ$ ,  $51.6^\circ$  and  $77.7^\circ$  represented a face-centred cubic structure for NiCo nanostructures with significant presence of *hcp* phases in Co-rich alloys. All the peaks related to *fcc* and *hcp* were indexed and these matched well with *fcc* Ni (JCPDS 15-0806) and Co (JCPDS 01-1260). However, presence of *hcp* phase (corresponding to {100}, {101}) throughout the composition ranges was noted and it became prominent for Co-rich content as  $\text{Co}_{80}\text{Ni}_{20}$  alloy crystallize in a mixed *fcc* and *hcp* phases. The (111) and (200) peak intensity ratios for alloys were calculated. It was seen that the ratio was increased for Ni-rich alloys. However, only NiCo-CTAB nanoflowers were crystallized exclusively in *fcc* phases as

shown in Fig. 5.6(A). The intensity ratio of NiCo (111) peak relative to (200) peak was found to be 3.7 for NiCo-CTAB, which was larger than that predicted for polycrystalline *fcc* NiCo (2.44) [82,88,89]. It was observed that Co-rich alloys crystallized in predominantly *hcp* structures despite the presence of Ni which was expected to favor *fcc* phase. Surface roughness of predominantly *hcp*  $\text{Co}_{78}\text{Ni}_{18}$  and  $\text{Co}_{59}\text{Ni}_{41}$  resulted from extended growth step by coalescence of primary nanoparticles of about  $\sim 100$  nm in size. It was previously shown that spherical shaped *hcp*  $\text{Co}_{80}\text{Ni}_{20}$  exhibited a high probability of stacking faults [88].

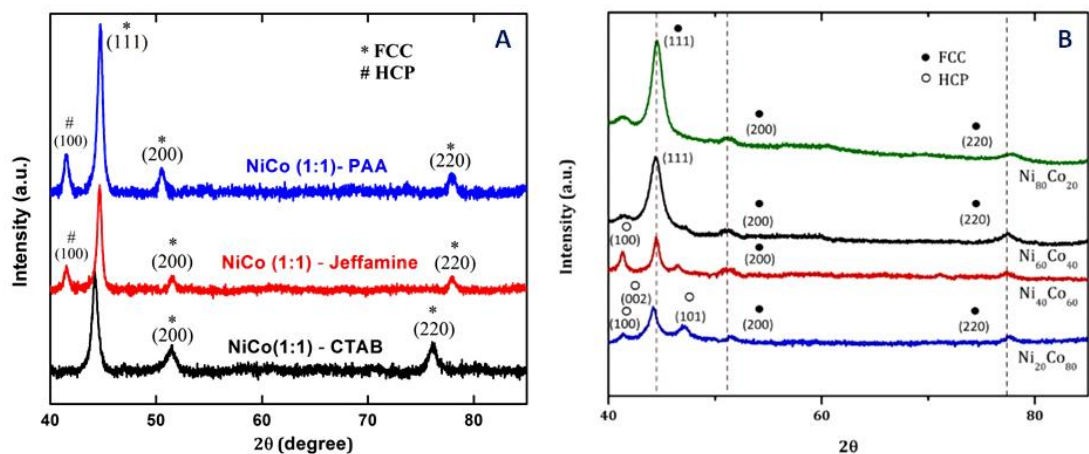


**Figure 5.6** (A) x-ray diffraction of NiCo-nanoflowers ( $\text{Ni}^{2+}:\text{Co}^{2+} = 1:1$ ) in presence PAA, Jeffamine and CTAB, (B) XRD patterns of as-synthesized nanostructures with increasing Ni-contents in alloys, obtained by the reaction of Jeffamine in 1, 2-propyleneglycol/KOH. The dashed lines mark the prominent peaks of bulk 1:1 alloy.

Fig. 5.7 shows the powder x-ray diffractogram of the raw  $\text{Ni}_{50}\text{Co}_{50}$  nanoplatelets synthesis product. It has to be noted that the phases were assigned in combination with TEM-EDAX determined compositions on individual nanoplatelets as described in the previous section. These analyses showed that the elemental composition and crystal structure was in good agreement with that of x-ray diffraction pattern. In Fig. 5.7, three sharp XRD peaks were observed at  $44.4^\circ$ ,  $51.5^\circ$  and  $77.4^\circ$ , corresponding to the (111), (200) and (220) planes, respectively. The appearance of these peaks in the XRD pattern indicated the existence of a face centered cubic (*fcc*) crystal phase in the product. Unlike

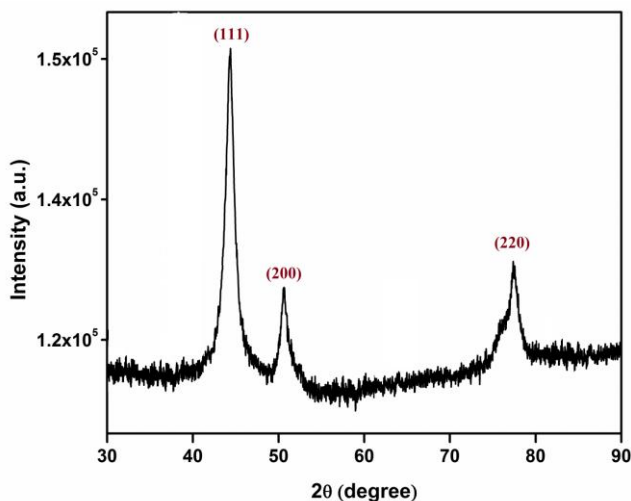


**Figure 5.7** x-ray diffraction of NiCo-nanoplatelets ( $\text{Ni}^{2+}:\text{Co}^{2+} = 1:1$ ). The major peaks correspond to *fcc* structure.

the previous NiCo alloys, XRD pattern of 1:1 NiCo nanoplatelets has shown no other detectable peaks, especially for those caused by either impurities such as  $\text{Co}(\text{OH})_2$  or  $\text{Ni}(\text{OH})_2$  or due to presence of unreacted Co or Ni. This suggests that the reduction reaction in our solvothermal route was completed.

### 5.2.3 Evolution of particles: growth mechanism

#### 5.2.3.1 NiCo hierarchical nanostructures

It has been known that the precipitation of a solid from solution proceeds in three distinct stages: 1. Nucleation, 2. Evolution of nuclei into seeds and 3. Growth of seeds into nanostructured materials [90]. In presence of high  $[\text{OH}^-]$  in precursor, free  $\text{Ni}^{2+}$  and  $\text{Co}^{2+}$  ion concentration decreased rapidly due to the formation of corresponding metal-hydroxyglycolates [84]. This has reduced effective reduction potentials of  $\text{Co}^{2+}$  and  $\text{Ni}^{2+}$  salts to as low as  $-0.74\text{V}$  and  $-0.73\text{V}$  at the given concentration of  $[\text{OH}^-]$  in reaction system, compared to the original redox potential values of  $\text{Co}^{2+}/\text{Co} = -0.29\text{V}$  and  $\text{Ni}^{2+}/\text{Ni} = -0.25\text{V}$ , respectively [82,91]. Therefore, Ni and Co-hydroxyglycolate intermediates can now be simultaneously co-reduced to the respective metal atoms to form NiCo nuclei. The nucleation step was expected to follow the model proposed by LaMer and coworkers [52]. The growth mechanism of final rose-like nanoflower was illustrated schematically in Fig. 5.8. Due to rapid decomposition of precursor, concentrations of metal atoms reached a supersaturation level and atoms of Co and Ni randomly oriented to form NiCo

nuclei via a self-aggregation (homogeneous nucleation) as long as there were no external seed nuclei. However, formation of well-defined structure i.e. seed from clusters of nuclei indicated a critical point of growth beyond which structural fluctuation became energetically unfavorable. Formation of seeds marked the start of final step of nanostructure synthesis. Seeds can have either single crystal, singly-twinned or multiply-twinned structures, and their formation depends on various factors. After formation of seed, diffusion of newly formed metal atoms established a dynamic equilibrium between growth and dissolution. Diffused atoms on the surface of seed moved until they found favored direction or ‘habit’ plane [90]. Finally seeds were grown to form spherical nanoparticles in presence of free polymer molecules. Hydrophilic parts of triblock copolymer preferentially adsorbed on nanoparticle surface to form uniform nanospheres as shown in Fig. 5.2A [92]. This served as a template for the growth of nanosheets around these spherical particles. As the reaction time increased, decomposition of precursor slowed down due to Oswald ripening and a consecutive second phase of seed generation took place via a kinetically controlled process. It was found that as soon as the solution attained supersaturation, formation of nuclei and seed took place through random

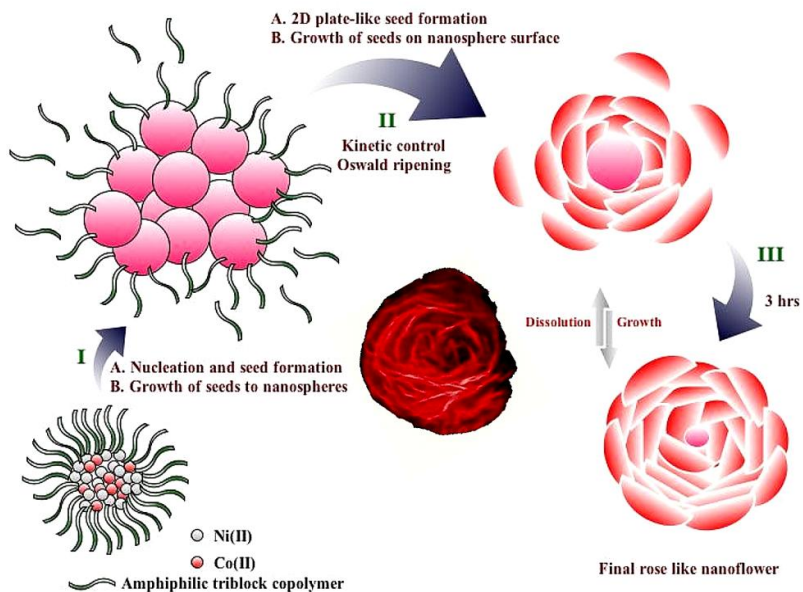


**Figure 5.8** The growth mechanism of hierarchical flower-like Jeffamine-NiCo structures.

hexagonal close packing (*rhcp*) with substantial stacking faults [93]. These stacking faults could lead to plate-like seed formation with exposed (111) facets at the edges (Fig.

5.3). In spite of the minimization of surface free energy due to formation of extended (111) facets, surface area of the plate-like seeds is considered to be very high and its formation can only be ascertained by kinetically controlled situation, as was the case here. The seeds then grew spontaneously onto the surface of nanospheres (Fig. 5.2B). As the reaction time increased further, more and more 2D sheets grew following a dissolution and growth equilibrium established on the nanospheres. As a result, size of spherical 'core' decreased. The final nanoflowers with substantial interplanar spacing obtained after refluxing the precursor for 3 hrs. However, it can be noted that nature and concentration of polymeric materials and surfactants, choice of polyol media, concentration of KOH in reacting media and appropriate molar ratios of Ni and Co-salts in precursor are equally significant in determining the final morphology of nanoflower and are discussed below.

Structural evolution of hierarchical nanomaterials from seeds was driven by introduction of selective capping agents. In our experiment, two polymeric materials with amphiphilic and hydrophilic properties (namely Jeffamine ED-600 and PAA) and one surfactant (CTAB) were used as capping agents for NiCo nanoflower synthesis. Role of surfactant and polymeric capping agents were extremely important in terms of overall morphology, size and surface properties. Preferential binding affinities of these capping agents towards a particular facet provide a means to control relative surface areas of other facets.

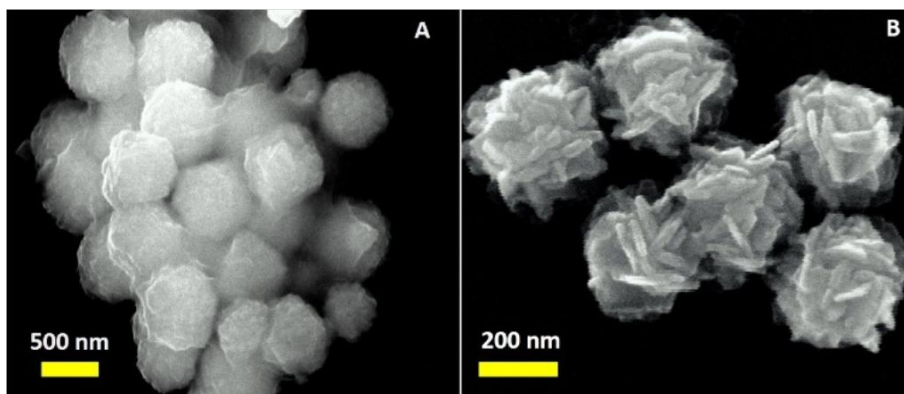


**Figure 5.9** FESEM images of NiCo-Jeffamine nanostructures synthesized in (A) ethylene glycol (EG) and (B) tetraethylene glycol (TEG).

Rose-like nanoflowers containing nanosheets ( $\sim 30$  nm thickness) attached to the core were obtained for Jeffamine, whereas nanoflowers with rod-like subunits were found

when PAA and CTAB were used as capping agents. Highly selective nature of nanoflower synthesis in presence of amphiphilic block copolymer arises from unique affinity of its amine N or ether O towards metal ions. Although the detailed mechanism of growth is unknown, it is believed that block copolymer helps in directing anisotropic growth towards the preferential plane or ‘habit’ plane. From HRTEM and SAED, it is seen that the preferential growth direction for nanosheets of Jeffamine-based NiCo flower was along (111) plane. For PAA-capped NiCo, selective binding of carboxyl O to metal centers provides a basis for ordered growth of nanorod and subsequent assembly of nanorod subunits to form uniform nanoflowers of different morphologies. For CTAB-mediated growth of NiCo nanoflower, building blocks are found to be a mixture of nanoplates ( $\sim 40$  nm thickness) and pointed nanorods growing outwards. It has been known that  $\text{Br}^-$  ions from CTAB act as smaller ionic capping agent and selectively adsorbed to (100) planes of metal atoms [94]. Since (100) facets are now blocked by  $\text{Br}^-$  metal atoms are added preferentially to exposed (111) facets. This is further confirmed by large (111) to (200) x-ray diffraction peak intensity ratio for NiCo-CTAB as basal plane of growth is (111) facet. The choice of polymer/surfactant is also known to affect the overall size distribution of nanoflower, as is shown in Fig. 5.1. Average size of nanoflowers follows the order: NiCo-Jeffamine ( $\sim 700$  nm) $>$ NiCo-PAA ( $\sim 330$  nm) $>$ NiCo-CTAB ( $\sim 240$  nm).

It was also found that the average size and morphology were significantly affected by the polyol used. When PrG was substituted by ethylene glycol (EG) or TEG, shape and size of nanostructures altered completely. In EG, no flowers like aggregates were formed; instead, spherical monodisperse nanometric units of NiCo-Jeffamine with an average diameter of  $\sim 800$  nm were obtained (Fig. 5.9A). For TEG, nanoflowers with average diameter of  $350$  nm were obtained (Fig. 5.9B). For the later, nanorod-like subunits with average length of  $40$  nm assembled side-by-side to form flower microstructures. Therefore, particle size decreases in the order: EG $>$ PrG $>$ TEG under reflux, in reverse order of the increasing boiling points of polyols. This can be rationalized in terms of reflux temperature (boiling point of polyol) with respect to polyols [95]. Slower reduction rate for NiCo nanomaterials in the order EG $<$ PrG $<$ TEG proved to affect overall particle

size distribution. Effect of viscosity of polyol in reduction rate (which suggests the opposite trend as rate of diffusion of NiCo nuclei was hindered by increasing viscosity of polyol) may be swamped by increasing reaction temperatures, thus facilitating faster rate and smaller crystallite size. The morphologies and sizes of NiCo nanostructures were also affected by the molar ratio of  $\text{Ni}^{2+}$  and  $\text{Co}^{2+}$  in the initial reaction mixtures. With changing  $[\text{Ni}^{2+}]$  in precursor, particle morphologies changed dramatically. When total molar concentration of metals in solution and temperature remained unaltered, increased mole ratio of  $\text{Ni}^{2+}$  facilitated the formation of flower-like nanostructures. For the syntheses, PrG was used as solvent-cum-reducing agent and reaction time was kept constant at 3 hrs. Fig. 5.10 showed FESEM images of NiCo-nanostructures with variable Ni-contents.

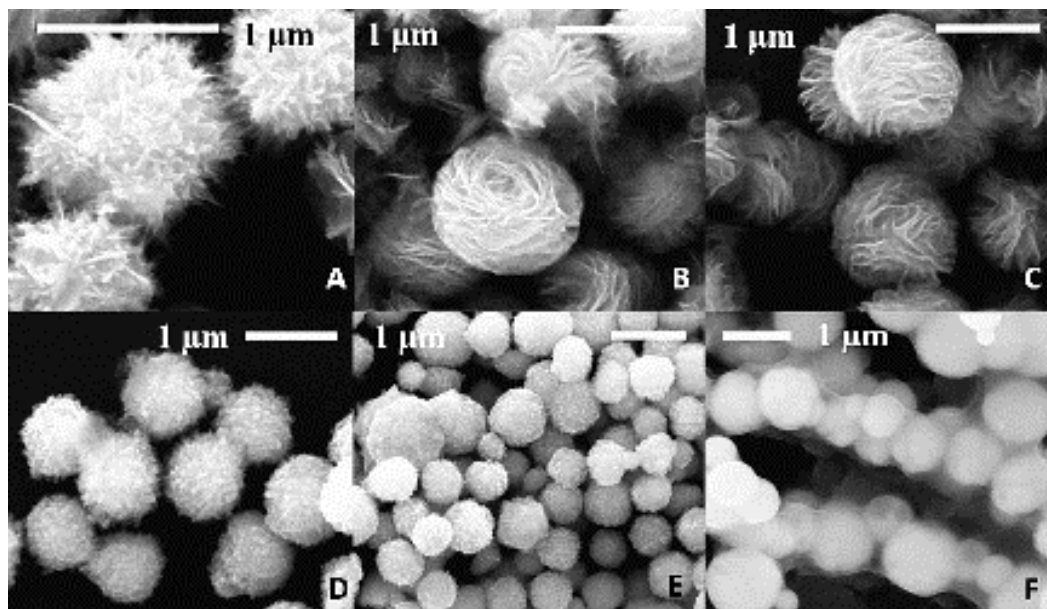


**Figure 5.10** FESEM images of NiCo nanoparticles obtained with the initial molar ratios of Ni(II) and Co(II) salts of (A) 0:100, (B) 20:80, (C) 40:60, (D) 60:40, (E) 80:20 and (F) 100:0, respectively.

Rose-like nanoflowers with 2D nanosheets predominantly form for compositions between  $\text{Ni}_{53}\text{Co}_{47}$  and  $\text{Ni}_{82}\text{Co}_{18}$ . For pure Co (Fig. 5.10F), spherical nanoparticles with smooth surfaces were obtained instead of assembled structures. For pure Ni (Fig. 5.10A), however, dendrites containing fibril-like subunits were formed. Therefore, shape of NiCo nanostructures with changing compositions varied widely from Ni-rich nanoflowers to Co-rich aggregated, uniform nanospheres (Fig. 5.10D and 5.10E). Initial molar

compositions along with final compositions and shapes of as-prepared NiCo are shown in Table 5-1.

The reflux reaction in PrG containing Jeffamine in presence of 1:1  $\text{Co}^{2+}$  and  $\text{Ni}^{2+}$  was repeated under different KOH concentrations in precursor and resulting nanostructures obtained are shown in Fig 5.11. It is evident from the FESEM images that the shape morphology of NiCo nanoflowers was strongly affected by basicity of the reacting media. At lowest concentration of KOH (0.2M), alloy nanoparticles appeared to have smooth spherical surface (Fig. 5.11A), while at higher concentrations surface roughness increased significantly.

**Table 5-1** composition, shape and size of NiCo alloyed microstructures of different metal ratios.

<b>Composition (Ni<sub>x</sub>Co<sub>1-x</sub>) taken</b>	<b>Final Composition</b>	<b>Mean diameter (nm)</b>	<b>Nanostructure shape</b>
Ni <sub>20</sub> Co <sub>80</sub>	Ni <sub>23</sub> Co <sub>77</sub>	750	Sphere with rough surface
Ni <sub>40</sub> Co <sub>60</sub>	Ni <sub>42</sub> Co <sub>58</sub>	700	Hierarchic sphere
Ni <sub>50</sub> Co <sub>50</sub>	Ni <sub>51</sub> Co <sub>49</sub>	700	Hierarchic flower with 2D nanosheets
*Ni <sub>50</sub> Co <sub>50</sub>	Ni <sub>51</sub> Co <sub>49</sub>	330	Hierarchic flower with nanorod
◆Ni <sub>50</sub> Co <sub>50</sub>	Ni <sub>53</sub> Co <sub>47</sub>	240	Hierarchic flower with nanorod and plate
Ni <sub>60</sub> Co <sub>40</sub>	Ni <sub>63</sub> Co <sub>37</sub>	750	Hierarchic flower with 2D nanosheets
Ni <sub>80</sub> Co <sub>20</sub>	Ni <sub>82</sub> Co <sub>18</sub>	800	Hierarchic flower with 2D nanosheets

◆Nanoflower with CTAB

\*Nanoflower with PAA

As the concentration of KOH increased to 0.6M, agglomerated nanostructures (size ~650 nm) containing tiny nanoparticles were formed (Fig. 5.11C). At lower concentration of KOH, insufficient  $[\text{OH}^-]$  allowed release of more free metal ions in solution and consequently, reduction rate was higher. In this case, smooth spherical nanoparticles with

smaller size were obtained. As KOH concentration was increased to 0.8M (Fig. 5.11D), growth rate was lowered significantly due to absence of free metal ions. Therefore, hierarchical nanoflowers composed of 2D-nanoplate subunits with preferred growth of exposed (111) facets were obtained. Higher deviations in Co and Ni compositions were also recorded for NiCo alloys prepared in presence of lower  $[\text{OH}^-]$  in precursor. A better match between initial molar concentrations of metals and in as-synthesized alloys was found for samples prepared under high molar concentrations of KOH. Experimentally observed compositions from energy dispersive x-ray (EDAX) studies of alloyed samples were tabulated in Table 5-1, against initial molar conc. of metals. This can be attributed

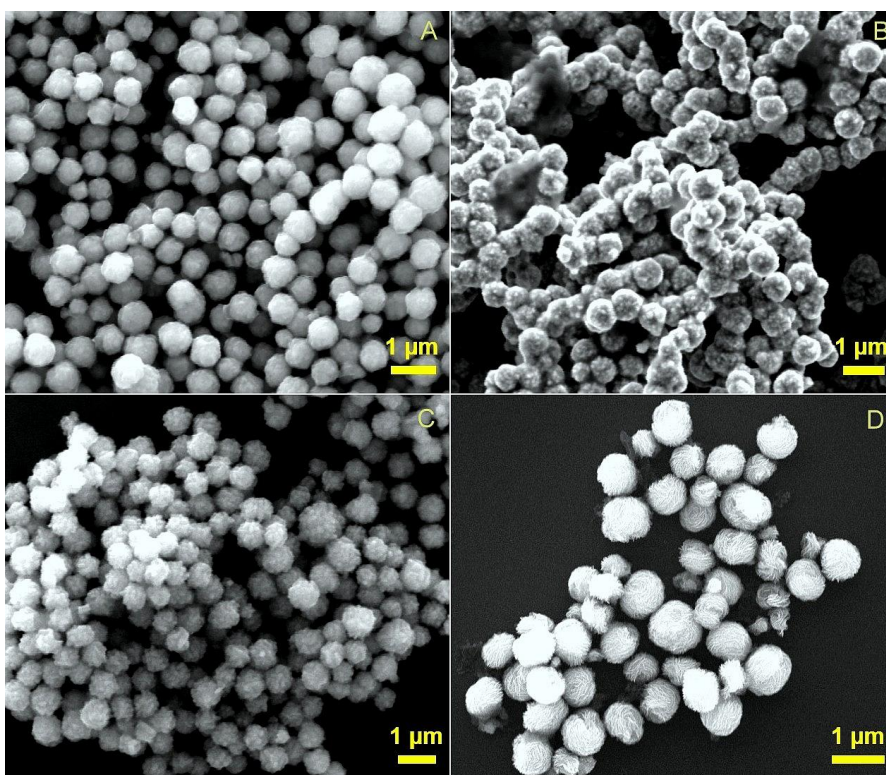


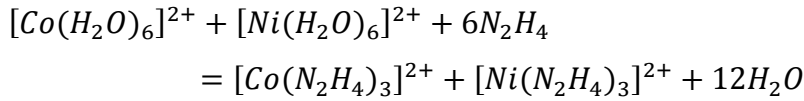
**Figure 5.11** FESEM images of NiCo nanostructures with Jeffamine by addition of different concentrations of KOH in PrG: (A) 0.2M, (B) 0.4M, (C) 0.6M, and (D) 0.8M.

to greater tendency of metals to undergo alloy formation in highly basic media. According to Rafique et al. [82], at lower KOH concentration,  $\text{Ni}^{2+}$  was reduced considerably faster than  $\text{Co}^{2+}$  and only a few  $\text{Co}^{2+}$  could take part in coprecipitation of alloy. The remaining  $\text{Co}^{2+}$  got reduced to metallic cobalt (*hcp*) and was separated after washing. As KOH conc. was increased, more metal salts formed hydroxyglycolate

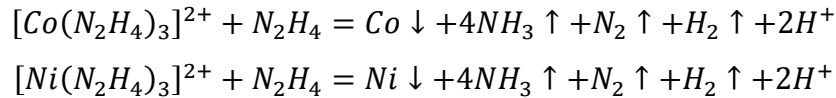
intermediates. As a result, effective reduction potentials of metals became closer and higher number of metal ions took part in coreduction.

### 5.2.3.2 NiCo nanoplatelets

On the basis of the reaction in the precursor solution at high temperature in aqueous medium, a possible growth mechanism for the formation of hexagonal CoNi nanoplatelets is described in this section. The formation mechanism of metal alloy nano and microstructures have been discussed in previous section. In the first step, dissolution of metal salts in precursor, i.e.  $\text{Co}^{2+}$  and  $\text{Ni}^{2+}$  ions dissolved in water in presence of surfactant CTAB to form colored aqueous solution. After hydrazine hydrate ( $\text{N}_2\text{H}_4 \cdot \text{H}_2\text{O}$ ) was added into the solution, the aqueous complexes reacted to form the complexes of  $[\text{Co}(\text{N}_2\text{H}_4)_3]^{2+}$  and  $[\text{Ni}(\text{N}_2\text{H}_4)_3]^{2+}$  and the solution turned turbid. The process is expressed by the following equation [96,97]:



In the next step, the hydrazine-complexes of respective metals reacted with excess free hydrazine in the solution at higher temperature to get reduced to individual metal ions. The reduction of metal salts into free metal atoms initiated the formation of alloyed nuclei. The reduction can be expressed in terms of following equation:



Individual metal atoms thus formed coalesced to generate NiCo alloy nuclei. Following homogeneous nucleation, seed formation and Oswald ripening, final nanostructured materials were grown. It has been previously stated that seed formation can effectively determine the final morphology of nanomaterials. The role of surfactant CTAB was extremely crucial in the directed growth of nanocrystals. The preferential attachment of

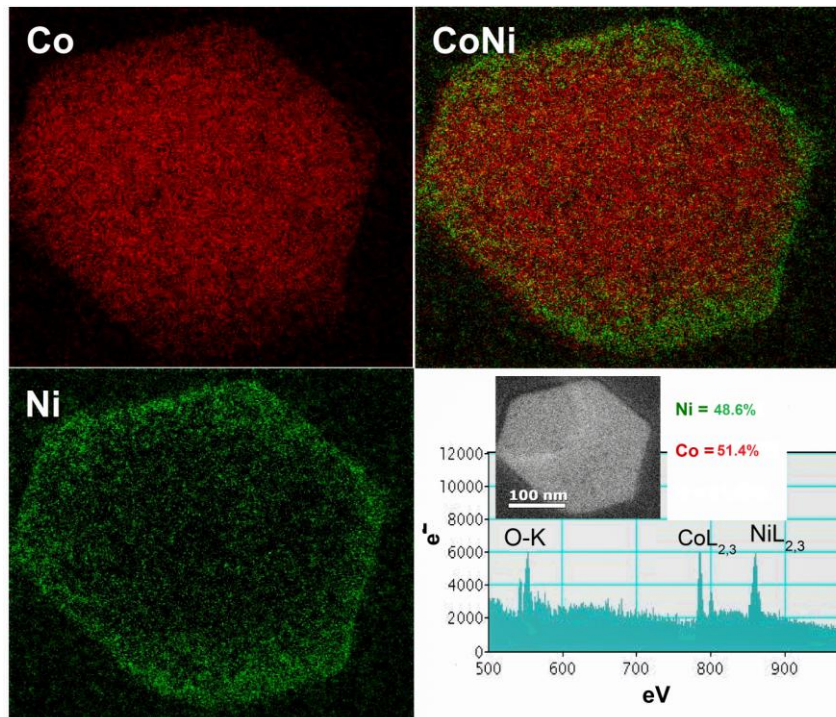


**Figure 5.12** HRTEM color mapping images of Co, Ni and NiCo in an isolated hexagonal nanoplatelet. The EELS spectra further confirmed the composition of CTAB-NiCo. The O comes from CTAB molecules.

CTAB molecule on exposed (111) planes gave rise to slow growth and led to the area enlargement of the (111) facets, and finally formed the NiCo alloy hexagonal nanoplatelets with exposed (111) crystal facets. The composition of NiCo alloy nanoplatelets were further investigated in TEM-color mapping and EELS spectra (Fig. 5.12).

The color mapping for Co and Ni components in a single hexagonal nanoplate revealed the almost uniform distribution of metals, with Co slightly more abundant at the core. Furthermore, the EELS spectra of NiCo alloy have shown that the composition of metals in the nanoplatelets was nearly equimolar.

#### 5.2.4 Magnetic characterization

Magnetic hysteresis (M-H) loops of NiCo flower-like samples were measured at room temperature (300K) and the data are presented in Fig. 5.13A and tabulated in Table 5-2. While comparing the effect of different polymers and surfactant on the magnetic properties of 50:50 alloys, we found marked variations with these as synthesized in the presence of Jeffamine, PAA and CTAB. For example while the bulk value of saturation

magnetization ( $M_s^{bulk}$ ) is 111.5  $emu/g$  [85], the NiCo-Jeffamine nanoflower has the highest  $M_s$  value of 108.6  $emu/g$  followed by others. This is among the highest values so far reported with 1:1 nanoflower composition. However, PAA-NiCo nanoflowers (mean diameter 330  $nm$ ) yielded much lower saturation magnetization compared to that of Jeffamine and CTAB. The reason for the spread in values of  $M_s$  maybe attributed to the presence of magnetically dead layers (MDL) [98], whose thickness can be estimated from the following equation [99]:

$$M_s = M_s^{bulk} \left(1 - \frac{6t}{d}\right) \quad (5.1)$$

where  $M_s^{bulk}$  is the bulk saturation magnetization of 1:1 NiCo alloy,  $d$  is the diameter of the particle and  $t$  is MDL thickness. The existence of MDL on surface might be caused by several factors, including surface spin canting [100] or loss of long range order in surface layers [101]. Putting in the values of other parameters in equation (5.1), we get values of ' $t$ ' for the three cases. It is interesting to note that minor difference in  $M_s$  values resulted in large difference in ' $t$ ' in cases of CTAB and PAA, while despite three-times

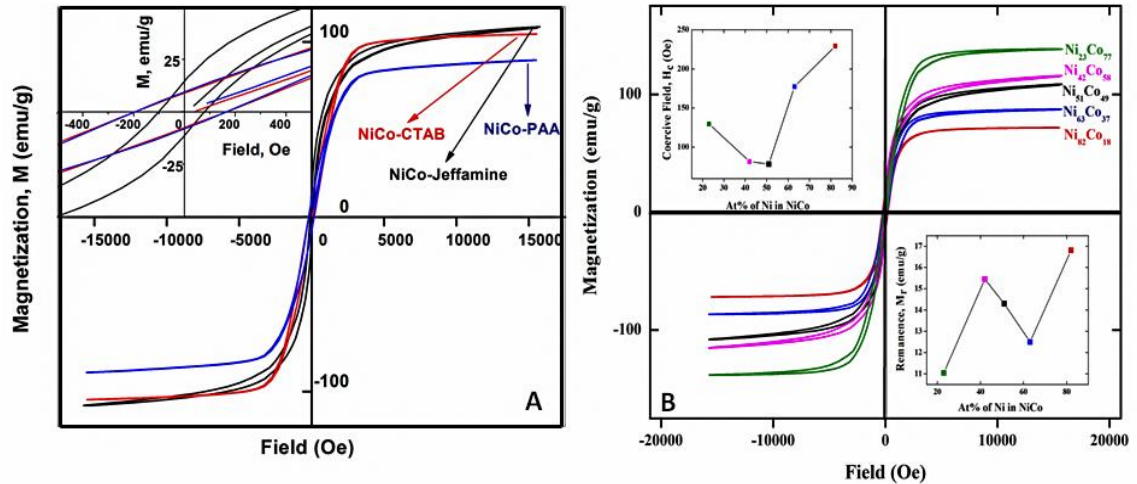


**Figure 5.13** (A) Room temperature magnetic hysteresis loops of NiCo flower-like nanostructures in presence of Jeffamine, CTAB and PAA. In the inset, zoomed in portions to show coercivity and remanence (B)  $M$  vs.  $H$  loops of  $Ni_xCo_{1-x}$  nanostructures ( $x = 0.2, 0.4, 0.5, 0.6, 0.8$ ) containing Jeffamine at room temperature. In the inset, coercivity (top left) and remanence (bottom right) plotted as a function of atomic percentage (at %) of Ni in the NiCo alloys.

**Table 5-2** Magnetic parameters of NiCo-Jeffamine nanostructures of different compositions.

Alloy	$M_s$ (emu/g)	$H_c$ (Oe)	$M_r$ (emu/g)	Dead layer thickness, t (nm)	Anisotropy constant, $K_1$ (erg.cm <sup>-3</sup> )
Ni <sub>20</sub> Co <sub>80</sub>	138.5	129.8	11.0	-	-
Ni <sub>40</sub> Co <sub>60</sub>	115.8	81.7	15.4	-	-
Ni <sub>50</sub> Co <sub>50</sub>	108.6	78.4	14.3	3.0	4.3×10 <sup>3</sup>
*Ni <sub>50</sub> Co <sub>50</sub>	89.6	160.8	9.4	10.8	7.2×10 <sup>3</sup>
◆Ni <sub>50</sub> Co <sub>50</sub>	104.5	162.7	8.6	2.5	8.5×10 <sup>3</sup>
Ni <sub>60</sub> Co <sub>40</sub>	87.3	177.3	12.5	-	-
Ni <sub>80</sub> Co <sub>20</sub>	71.7	229.0	16.8	-	-

◆Nanoflower with CTAB as surfactant

\*Nanoflower with PAA as polymeric capping agent

the size difference, the CTAB and Jeffamine coated samples yielded similar values. These all point to the effect of MDL which obviously had a significant effect on the magnetic properties of the samples. Another interesting feature was found in the coercivity values. The lowest value was recorded for NiCo-Jeffamine whereas almost similar values were observed for NiCo-PAA and NiCo-CTAB. This probably arose from more rounded shape of the former. Coupling  $M_s$  with the coercivity ( $H_c$ ) values, we can estimate the anisotropy energy ( $K_I$ ) from the following equation [20,98],

$$H_c = \frac{2K_1}{M_s} \quad (5.2)$$

Corrections due to demagnetizing factor are neglected here. The reasons are two - first is that the samples are collections of randomly oriented roughly spherical particles and as importantly, two is that we do not know yet the different demagnetization factors. With these limitations,  $K_I$  values as estimated from equation 5.2 are given in Table 5-2. It is interesting to note that  $K_I$  comes highest for the sample with CTAB which is smallest in size than others and is quite rough in surface also. The samples with bigger sizes and smoother surfaces expectedly have lower  $K_I$  values. The magnetic hysteresis loops of Ni<sub>x</sub>Co<sub>1-x</sub> -Jeffamine nanostructures with different Ni/Co molar ratios are shown in Fig. 5.13B. With increasing Co content, saturation magnetization ( $M_s$ ) increased monotonously as expected. Highest  $M_s$  value of 138.5 emu/g is found for Ni<sub>33</sub>Co<sub>77</sub> and is comparable to the bulk value (141.7 emu/g). However,  $H_c$  values first decreased and

obtained the lowest coercivity at Ni<sub>51</sub>Co<sub>49</sub> and then increased when atomic-% of Ni in NiCo alloy was increased. Highest coercivity of 229 Oe was reported for Ni<sub>82</sub>Co<sub>18</sub>. The trend in coercivity values can also be explained in terms of increased Ni proportions in these alloys.

The measurements of magnetization versus applied magnetic field for NiCo nanoplatelets are plotted in Fig. 5.14. The saturation magnetization ( $M_s$ ), remanence ( $M_r$ ) and

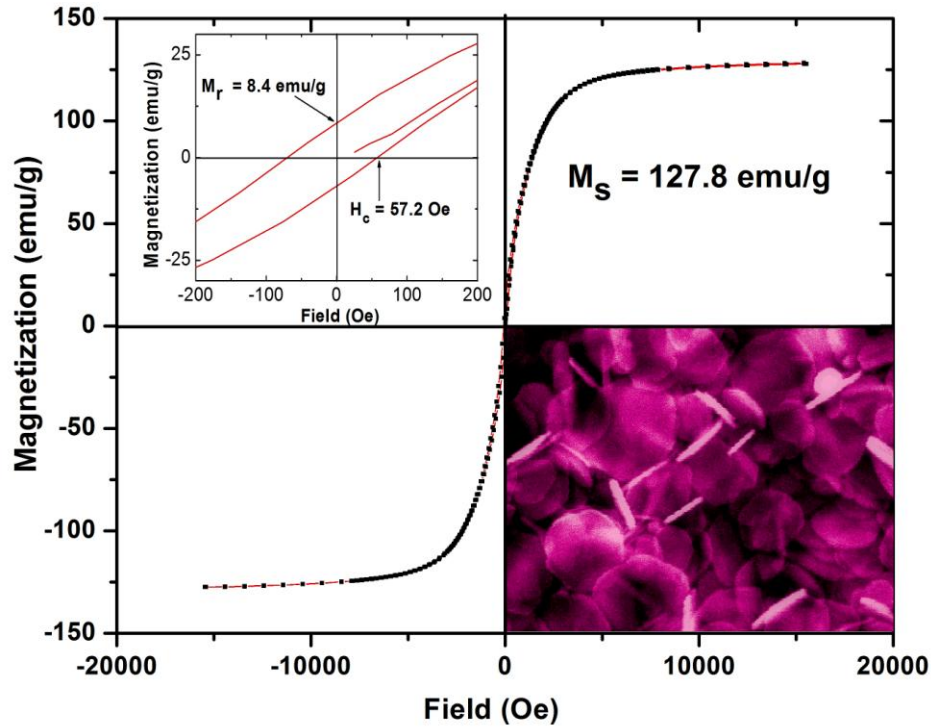


**Figure 5.14** M vs. H loops of NiCo nanoplatelets at room temperature. In the top inset, coercivity and remanence are highlighted.

coercivity ( $H_c$ ) were measured to be 127.8 emu/g, 8.4 emu/g and 57.2 Oe, respectively. It was observed that magnetic saturation value for NiCo platelets were slightly higher than nanoflowers with same compositions. This was related to the shape anisotropy of magnetic materials.

### 5.3 Magnetorheological studies

#### 5.3.1 NiCo-flower based MR fluids: role of ferrofluid in MR effect

For magnetorheological measurements, two 5 vol% MR fluid samples (MRF1 and MRF2) were prepared by dispersing exact amount of NiCo nanoflowers (density 7.6 g/cc compared to bulk density 8.90 g/cc) in silicone oil (viscosity 30 mPa.s at 25 °C) and aqueous Fe<sub>3</sub>O<sub>4</sub>-based ferrofluid, respectively (Cat. No. MSGW07, viscosity < 10 mPa.s with average particle diameter ~10 nm and from Ferrotec<sup>®</sup> Corp., Japan). Magnetorheological studies were performed for MR fluids using Anton Paar Physica MCR 301 Rheometer<sup>®</sup> with parallel plate geometry (plate gap 1 mm) at 25°C. Steady state MR rheograms (shear stress versus shear rate) were shown in Fig. 5.15.

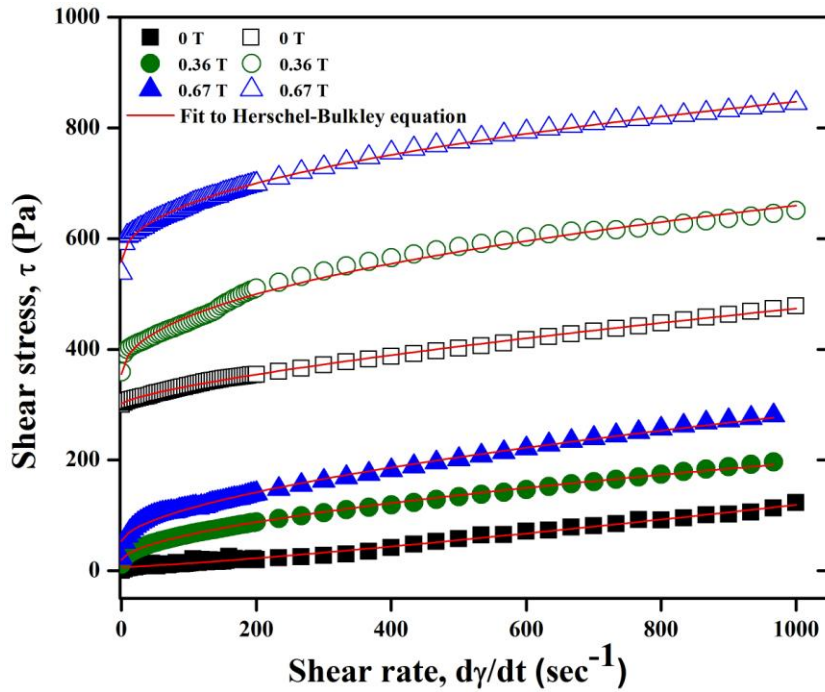


**Figure 5.15** steady state magnetorheological results for MRF1 (NiCo nanoflower dispersed in silicone oil, closed symbol) and MRF2 (NiCo nanoflower dispersed in ferrofluid, open symbol) under different magnetic fields.

The rheological behavior shows that the ferrofluid based system has a higher yield stress between the two. Since the behavior is evidently non linear, we tried to fit Herschel-Bulkley fluid model to describe it,  $\tau = \tau_0 + k\dot{\gamma}^n$  where the parameters were already described. Table 5-3 gives the fitting parameters:

**Table 5-3** Herschel-Bulkley fitting parameters for MRF1 and MRF2 under different fields

Samples	Field (T)	$\tau_0$ (Pa)	$k$ (Pa.sec <sup>-n</sup> )	$n$
---------	-----------	---------------	-----------------------------	-----

MR1	0.00	6.52	0.027	1.20
	0.36	18.70	3.19	0.581
	0.67	52.60	4.09	0.584
MR2	0.00	301.69	1.080	0.734
	0.36	350.84	13.48	0.453
	0.67	552.80	14.97	0.431

The examination of the table shows that overall the behaviors were regular and consistent with the prediction discussed previously. We see that there is a trend of enhancing the yield stresses ( $\tau_0$ ) and consistencies ( $k$ ) as the field was increased, the system became more shear thinned ( $n < 1$ ). This reflects the fact that the systems were quite affected by the field, and the lower values of  $n$ , coupled with higher values of  $\tau_0$  and  $k$  imply that the ferrofluid based system was affected more strongly. Therefore, magnetorheological (MR) studies of samples containing nanoflowers in silicone oil and ferrofluid indicated stronger MR properties for the later due to stronger microstructure formation under applied field as nanoparticles from ferrofluid interacted strongly with nanoflower-surface.

### 5.3.2 Magnetorheology in NiCo nanoplatelet-based suspensions

#### 5.3.2.1 Oscillatory magnetorheology: Strain-induced thickening in loss modulus ( $G''$ )

For magnetorheological studies under oscillatory mode, three different MR suspensions (namely M1, M2, M3) containing 5 vol%, 8 vol% and 12 vol% of NiCo nanoplatelets were prepared. The appropriate amounts of NiCo powder were dispersed into castor oil following mechanical stirring and ultrasonication. Fig. 5.16 shows the strain amplitude ( $\gamma$ ) dependence of storage ( $G'$ ) and loss modulus ( $G''$ ) measured at a constant frequency of 10 Hz for suspensions containing 5 vol%, 8 vol% and 12 vol% under three different magnetic field strengths:  $0.24T$ ,  $0.4T$ ,  $0.6T$ . The trend is expected and in coordination with the existing explanation commonly associated to viscoelastic behavior of MR suspensions under oscillatory shear. Both moduli exhibited constant initial values of storage and loss energy, commonly denoted as  $G'_0$  and  $G''_0$ , respectively until the critical strain amplitude ( $\gamma_c$ ) was reached. This constant region is defined as linear viscoelastic regime (LVR). Beyond this critical strain, the storage modulus decreased gradually as a

function of strain and loss modulus showed a hump or maxima correspond to strain hardening point, expressed as  $G''_{max}$  till both the moduli intersected at cross-over point. This point signifies that the system started flowing as  $G''$  overcame  $G'$ . In the LVR region, the suspension behavior was strongly influenced by particle volume fractions and magnetic field strengths. Sample with lowest  $\phi$  (M1) exhibited maximum value of  $\gamma_c$  followed by M2 and M3. The linear region of  $G''$  decreased as the volume fraction was increased.

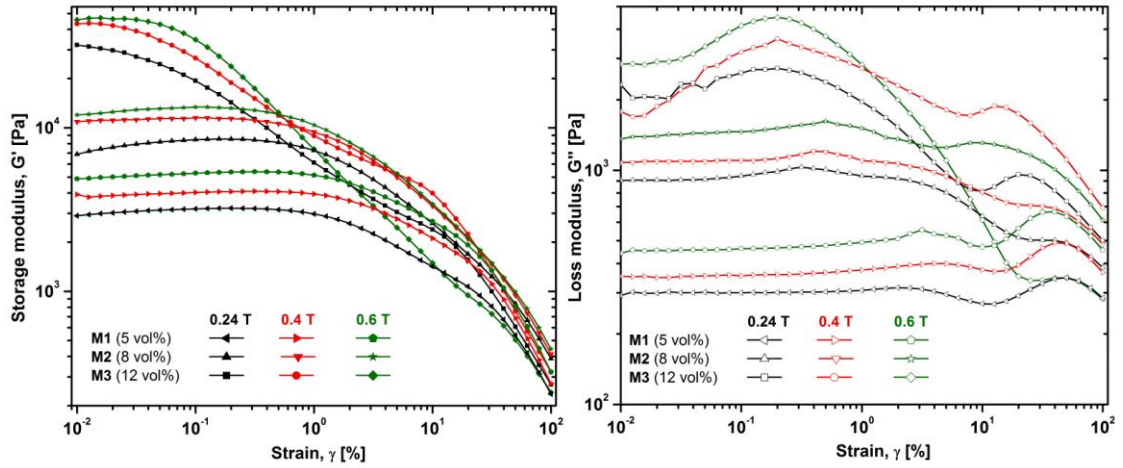


**Figure 5.16** Storage modulus ( $G'$ ) and loss modulus ( $G''$ ) at constant frequency of 10 Hz plotted as a function of shear strain amplitude ( $\gamma$ ) for different magnetic fields and suspension vol%.

Previous studies demonstrated a power-law dependence of  $G'_0$  and  $G''_0$  values with volume fractions. This relationship can be explained in terms of cohesive energy density that is associated with work done to break the field-induced aggregates [102],

$$E_{cohesive} = \int_0^{\gamma_c} \tau d\gamma \quad (5.8)$$

Also, shear stress ( $\tau$ ) in LVR is expressed as  $\tau = G'_0 \gamma$ . Therefore, cohesive energy is expressed as:

$$E_{cohesive} = \frac{1}{2} \gamma_c^2 G'_0 \quad (5.9)$$

Therefore, increase in cohesive energy with increasing particulate concentration  $\phi$  in suspensions is associated to excluded volume interaction that arises due to the reduction in average interparticle distance. The extended linear region for M1 (lowest  $\phi$ ) can be explained in terms of the ease of formation and strength of field-induced aggregates. As

$\phi$  is smaller, the structuration in suspension induced by magnetic field would be affected. However, the apparent ambiguity in  $\gamma_c$  can be explained by the fact that the structures formed under higher  $\phi$  were more prone to be affected by strain amplitude. The extended linear region appeared not because of systematic deformation of particle chain junction, but rather due to microscopic movements and minor twisting within the chain network. For higher  $\phi$  ( $M3$ ), the arrested chain networks prevented the microscopic movements of percolated aggregates, making them more prone to external strain than that in the case for suspensions with lower  $\phi$ .

For loss modulus, strain hardening corresponded to a maximum in the stress-strain curve and is typical of all the samples investigated. However, as expected, the strain-hardening was most prominent in case of concentrated suspensions. The reason was fluctuation in interparticle distance induced by increased particle concentration. Excluded volume interaction forced the particles to align and therefore, enhanced the magnetostatic interaction. For higher  $\phi$ , both short range interaction and strong magnetostatic force arising from field-induced structural aggregates were coupled to exhibit significant strain hardening in  $G''$ . Beyond the LVR, gap-spanning aggregates formed at equilibrium started to disintegrate into domains of anisotropic clusters under oscillatory shear. As the systems reach yield point, flow was initiated following the cross-over strain ( $\gamma_c$ ). Finally for much higher strain ( $\gamma > 20\%$ ), a second maximum was appeared corresponding to minor aggregates in the sheared volume. The shear-induced densification of aggregates forced them to realign, giving rise to the second maximum. Above  $G'' > G'$ , minor aggregates were completely lost and systems flowed indefinitely.

## 5.4 Conclusion

In this chapter, we investigated the structure and morphology of NiCo alloyed microparticles of various shapes, sizes, composition and magnetic properties. We fabricated hierarchical NiCo nanoflowers and NiCo nanoplatelets. The bidisperse MR fluids containing NiCo nanoflowers in ferrofluidic suspensions displayed stronger MR effect in steady shear rheology, as compared to monodispersed one. The stronger microstructure formation in bidisperse fluids further reflected in higher off-state viscosity, compared to that of other fluid. The strain dependent hardening of  $G'$  was

explained in terms of short range interaction and reduction of effective interparticle distance when fluid volume% was increased.

6

## Chapter 6

### Structure and magnetorheology in NiCo microcluster-based systems

*In this chapter, we discussed the structure and morphologies of Co-rich hierarchical NiCo microcluster synthesized by a novel surfactant/polymer-free polyol reduction. The structure and morphology of the  $Ni_{0.1}Co_{0.9}$  microcluster were investigated by SEM, TEM and X-ray diffraction analysis. Room temperature steady magneto-shear studies indicated viscoplastic behavior with stronger dependence of static yield stress on magnetization than a dipolar coupling that was operational in the dynamic yield stress. Magnetosweep measurements at constant shear rate showed interesting viscous relaxation at high magnetic fields. We also explored dynamic elastic behavior through oscillatory magnetorheological studies under both strain sweep and frequency sweep modes, and showed a glass transition like phenomenon above crossover strain. The temperature-induced MR investigations were also performed in order to gain insight and explore the operability of MR fluids for practical purposes.*

## 6.1 Introduction

In this chapter, we discussed the properties of hierarchical  $\text{Ni}_{0.1}\text{Co}_{0.9}$  microclusters. The Co-rich  $\text{Co}_{0.9}\text{Ni}_{0.1}$  alloy was selected as a preferred composition due to its higher saturation magnetization than the 1:1 alloy. Furthermore, in order to further study the microstructure-rheology correlation in MR fluids, cluster-like morphology was chosen which are predominantly formed in Co-rich NiCo alloys. The samples were prepared by novel polymer and external reductant-free polyol method where polyol itself acted as solvent-cum-reducing agent. The detailed growth mechanism of hierarchical microstructures from precursor in polyol reduction was discussed in chapter 5. Two variants of MR fluid samples were prepared by dispersing 15 vol% and 20 vol% of  $\text{Ni}_{0.1}\text{Co}_{0.9}$  powders in castor oil. The rheological studies were performed in transient and oscillatory magnetorheological measurements under various conditions, e.g. magnetic field, particle volume fraction, ferrofluids as carrier liquids etc.

In this chapter, we also studied the influences of temperature on MR effect of the fluids containing these microclusters under steady shear rheology. We investigated the mechanism that governs non-equilibrium size distribution of internal chain structures with increasing temperature. We also deduced experimental scaling parameters to correlate magnetic field and temperature-dependent shear properties. Scaling laws are generally used to study the dependence of one physical parameter to multiple variables or factors, therefore, provide insight to the internal mechanism that governs interactions within the MR fluids [103].

## 6.2 Structure and morphology of microclusters

### 6.2.1 SEM and TEM studies on $\text{Ni}_{0.1}\text{Co}_{0.9}$ microclusters

The morphologies and average sizes of the microclusters and size distribution were obtained from FESEM and low magnification TEM images and are shown in Fig. 6.1A and 6.1B. Average size was calculated to be 450 nm. The surface morphology of  $\text{Ni}_{0.1}\text{Co}_{0.9}$  can tentatively be related to the mechanism of formation. It follows two distinct phases of nanocrystal formation: nucleation and growth. The nanoparticles in polyol can either follow stepwise addition of metal atoms to form seed and subsequent coalescence of seed into nanoparticles, or primary nanoparticles aggregate to form larger micron-sized

clusters. It was seen that in this case, the latter arrangement took place [79,84,88]. The selected area diffraction (SAED) pattern for the material indicates polycrystalline nature of sample (Fig. 6.1D). The EDAX spectrum of the as-prepared  $\text{Ni}_{0.1}\text{Co}_{0.9}$  microcluster is shown in Fig. 6.1(C). It showed that Co/Ni ratio in the microcluster was very close to the initial molar ratio (1:9 for [Ni]: [Co]) of the metals salts. The spot EDAX analysis for different positions across the diameter of microcluster was also performed and it was found that  $\text{Co}_{0.9}\text{Ni}_{0.1}$  maintained compositional homogeneity.

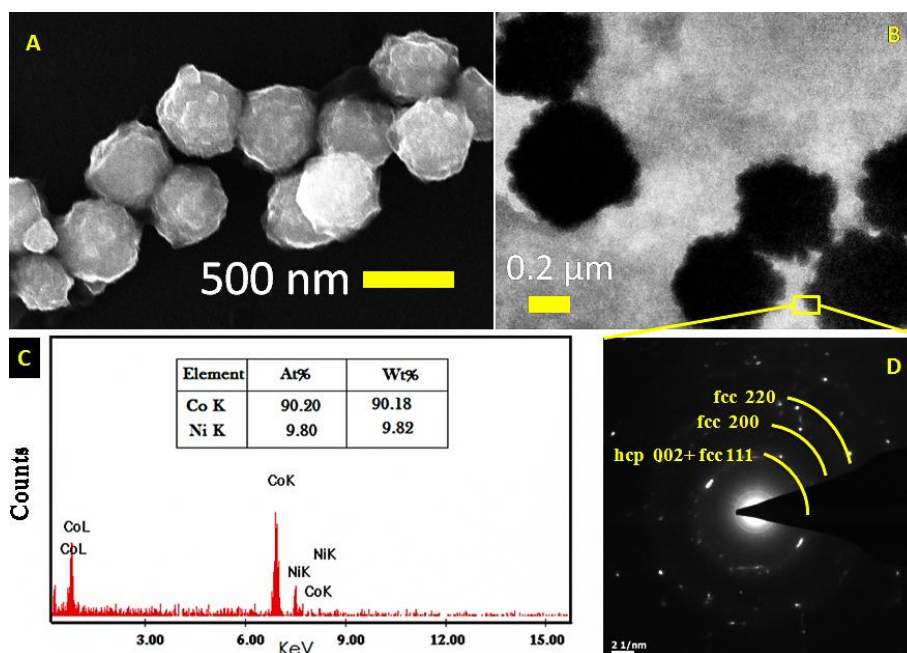


**Figure 6.1** (A) FESEM image of  $\text{Co}_{0.9}\text{Ni}_{0.1}$  microclusters, average diameter of nearly spherical microclusters was found to be 450 nm; (B, D) low resolution TEM image and selected area diffraction pattern (SAED), (C) EDAX of the sample confirmed the composition.

### 6.2.2 X-ray diffraction studies of NiCo microclusters

The crystal structures and phases of the Co-rich NiCo microclusters were determined by powder x-ray diffraction as shown in Fig. 6.2. The featured peaks at  $2\theta = 44.6^\circ$ ,  $51.7^\circ$ ,  $77.6^\circ$  were assigned to *fcc* crystal structure while significant presence of *hcp* Co phases at  $2\theta = 42^\circ$ ,  $44.8^\circ$  and  $47.5^\circ$  were also reported. In hierarchical NiCo flowers, it was previously observed that Co-rich NiCo alloys tend to crystallize in mixed *fcc* and *hcp*

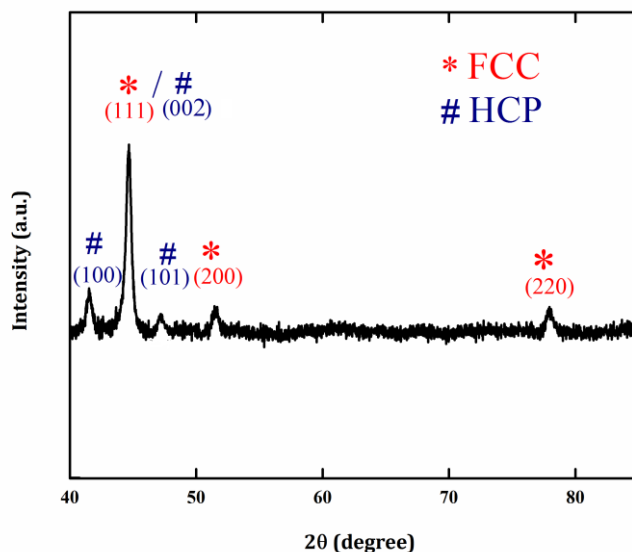


**Figure 6.2** Powder x-ray diffraction peaks of as-synthesized  $\text{Co}_{0.9}\text{Ni}_{0.1}$  microclusters. All peaks were assigned to *fcc* and *hcp* phases.

phases [85]. However, all peaks corresponding to *fcc* phases were indexed to *fcc* Ni (JCPDS 15-0806) and Co (JCPDS 01-1260). CoNi alloyed microstructures with more than 80 atomic% of Co exhibited higher probability of stacking fault [84]. The surface of microclusters appeared to be rough for Co-rich CoNi due to extended growth step by aggregation of primary nanoparticles units.

### 6.2.3 Magnetic characterization

Magnetic hysteresis at room temperature and FC-ZFC magnetization curves of the microclusters are shown in Fig. 6.3. The  $M$  vs.  $H$  hysteresis loop indicated ferromagnetic character of the sample at room temperature. The saturation magnetization ( $M_s$ ), remnant magnetization ( $M_r$ ) and coercive field ( $H_c$ ) values were calculated to be 119.5  $\text{emu/g}$ , 21  $\text{emu/g}$  and 142  $\text{Oe}$ , respectively. Magnetic saturation for  $\text{Co}_{0.9}\text{Ni}_{0.1}$  was lower than that of bulk Co or  $\text{Co}_{80}\text{Ni}_{20}$  alloy [85]. As reported earlier,  $M_s$  values for nanoparticles were considerably smaller than that of bulk alloys with same compositions, possibly due to the presence of passive dead layer of metal oxides on the surface [85,88]. The ratio of  $M_r$  to  $M_s$  at room temperature was 0.17 which was considerably lower than 0.35, indicating

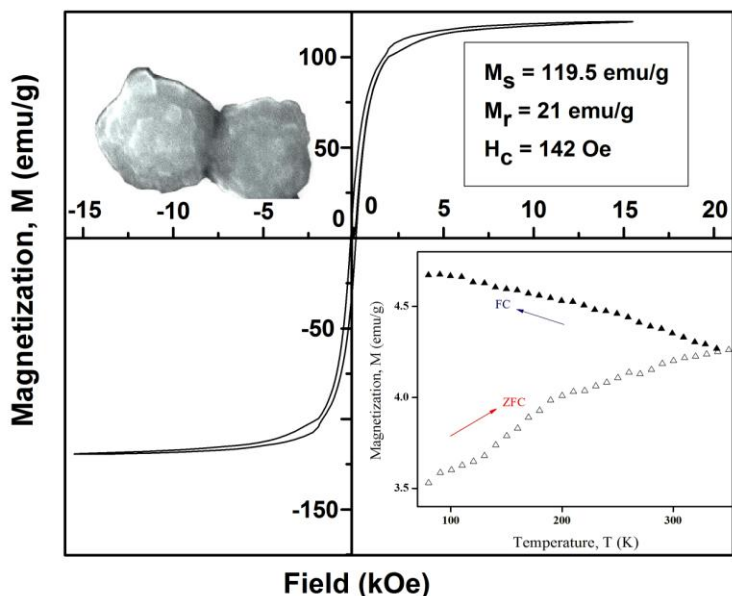


**Figure 6.3** Magnetization curve at  $T = 298\text{K}$  for  $\text{Co}_{0.9}\text{Ni}_{0.1}$  microclusters. In the right inset, ZFC-FC magnetization curves under an applied field of 100 Oe were shown.

randomly oriented, blocking type nanoparticles [104]. To confirm the magnetic state, ZFC and FC measurements from 75K to 350K, were performed in presence of field (100 Oe). The bifurcation between these indicated irreversibility starting from above room temperature, due to the magnetic nanoparticles.

## 6.3 Magnetorheological studies

### 6.3.1 $\text{Ni}_{0.1}\text{Co}_{0.9}$ microcluster-based MR fluids

The MR fluids were made by dispersing proper amounts of Co-rich  $\text{Ni}_{0.1}\text{Co}_{0.9}$  microcluster powder into castor oil (viscosity 0.879 Pa.s at 25°C) through mechanical stirring and ultrasonication. Two MR suspensions (MR1 and MR2) were prepared, with dispersed phase concentrations of 20 vol% and 15 vol%, respectively. Silica nanopowder (Merck, 2 vol% for each suspension with particle size  $\sim 20\text{ nm}$ ) was also added to avoid irreversible particle aggregation and settling. For magnetorheological measurements, magnetic field was varied from 0 to 0.6 T. Before any measurement, the sample was pre-sheared at  $20\text{ s}^{-1}$  for about 30 s. In magnetosweep experiment, field was varied from 0 to 1.1 T and back to zero under constant shear rate of  $10\text{ s}^{-1}$ . Dynamic (oscillatory) magnetorheological properties were probed by amplitude and frequency sweep experiments at 25°C. In amplitude sweep, an oscillatory strain ranging from 0.01% to

100% was applied to the sample under constant frequency of 10 Hz. The measurements were repeated at 0.04 T, 0.24 T and 0.5 T. Frequency sweep measurements were carried out under constant strain amplitude of 0.02% under the fields of 0.04 T, 0.24 T and 0.5 T. Angular frequency sweep was performed from highest (100 Hz) to lowest (0.1 Hz) frequency. Temperature-dependent MR studies under steady shear (controlled shear rate, CSR) mode were performed at 35°C, 45°C and 55°C, in addition to room temperature (25°C).

#### *6.3.1.1 Role of particle concentration in steady shear and magnetoviscous effect (MVE)*

The flow curves (Fig. 6.4, left panel) under controlled shear rate modes are obtained as a function of different magnetic fields for both magnetorheological samples, MR1 and MR2. The magneto-rheograms for both MR1 and MR2 characteristically displayed typical MR behavior. It is evident that a threshold shear stress is required to make the initial flow, which is a property of yield stress fluid and this initial stress at very low shear rate ( $\sim 0.001 - 0.1$ ) is termed as static yield stress ( $\tau_{ys}$ ) [105,106]. With increasing field, initial stress required to make the fluid flow would also go higher, owing to the formation of more robust field-dependent interparticle network. However, values of shear stresses obtained in different magnetic fields were different for both MR1 and MR2. Increasing concentration of suspended magnetic particles usually enhances MR performance [107]. Generally, field-dependent magnetorheological parameters (yield stress, shear viscosity, storage modulus) exhibit linear or power-law relationship with concentration of MR fluids [15]. This also holds good for these samples as we observe systematic increment of shear stress upon application of field. In the beginning, the field induced change was high, but at higher fields (0.4T or more), the changes leveled off as magnetic particles tend to saturate progressively. With increasing field, MR1 with higher magnetic concentration tended to form plateau-like rheograms, giving rise to more shear-thinning behavior beyond a critical shear stress. Transition from solid-like to liquid-like

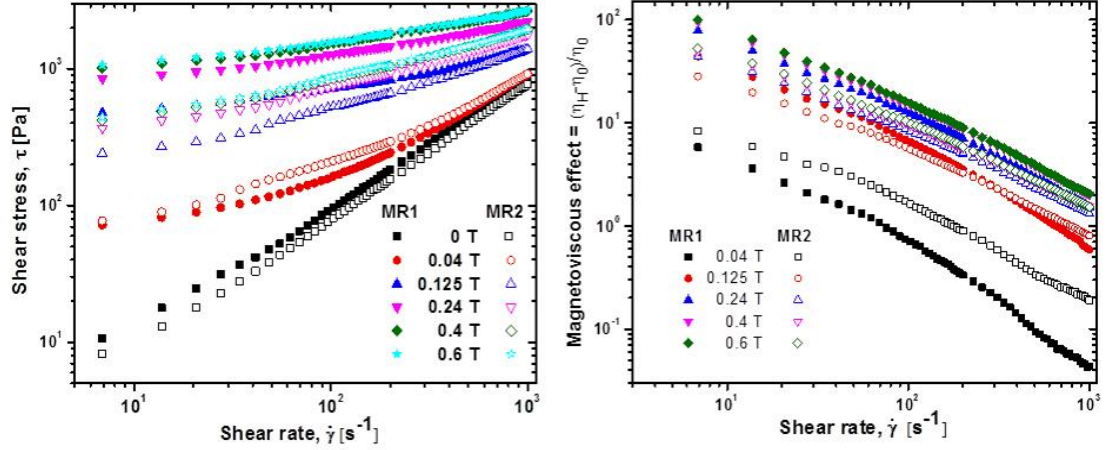


**Figure 6.4** (left) Shear stress ( $\tau$ ) plotted as a function of shear rate ( $\dot{\gamma}$ ) for different values of magnetic fields. Closed symbols is for sample MR1 whereas open symbol represents MR2. (Right) Magnetoviscous effect, MVE as a function of shear rate for MR1 and MR2 under different magnetic fields.

state was more regular for MR2 with lesser magnetic vol%. For concentrated fluids, due to flocculated structures formed at rest, flow of fluid was hindered below a certain shear stress. Beyond that stress (yield stress), it started flowing suddenly. For the lower concentrated fluids, transition from solid to liquid state was more gradual as structure at rest was relatively weaker. Another way to look at this behavior is to define the flow characteristics of magnetic fluid through a parameter  $\eta_M$ , called magnetoviscous effect (MVE). This is defined as the change in shear viscosity at a particular field and shear rate, in comparison to its zero field viscosity [106]:

$$\eta_M = \frac{\eta_H - \eta_0}{\eta_0} \quad (5.3)$$

Where  $\eta_H$  and  $\eta_0$  are the viscosities of MR fluid at a specified magnetic field and zero magnetic field, respectively. Fig. 6.4 (right panel) illustrates the MVE in flow regime as a function of shear rate for MR1 and MR2 under different magnetic fields. The magnitude of MVE decreases continuously with increasing shear rate for both samples and at all fields. This is generally expected as in flow regime hydrodynamic interactions must overcome magnetostatic forces. Therefore, field-induced aggregates are broken to continue the flow. It is also observed that MVE is more pronounced in MR1, compared to MR2. The relative increment of viscosities at a given field and a given shear rate for MR1 is higher than that of MR2 due to higher off-state viscosity of the former.

Moreover, higher concentration of magnetic microclusters in MR1 facilitated stronger field-induced chain structure, making it more rigid to external shear.

### *6.3.1.2 Magnetosweep measurement and field-dependent relaxation*

Fig. 6.5 shows magneto-sweep curves for the two samples. At a constant shear rate of  $10\text{ s}^{-1}$ , viscosity was varied as a function of magnetic field within a range of 0 to 1.15 T. It was observed that viscosity increased with increasing field, owing to the formation of field-dependent microstructures. At higher field, MR suspensions tended to saturate and viscosity remained unchanged for the rest of the field. Although both samples contained the same  $\text{Co}_{0.9}\text{Ni}_{0.1}$  microclusters, saturating field limit for MR1 was higher than that of MR2. At any field, viscosity for MR1 was found to be much higher than that of MR2, as is usually observed in suspensions with higher particle volume fractions. The tendency to form lateral aggregation (known as zippering) between single chain microstructures was more pronounced in MR1. For both samples, viscosity corresponding to backward field sweep was higher than forward sweep. This gave rise to hysteresis behavior [108]. This is a behavior that is similar to M-H curves, and indeed on comparison to Fig. 6.3, they look alike. This means that the dipole-dipole interaction was the main cause of field induced viscosity here, and once the systems were saturated, they did not offer further hindrance to the flow. The major change was in the final value of viscosity, within the magnetic fields, these are 3-times more for the denser sample. Since the volume fraction is about 33% more, this increase is expected.

The interesting observation is the crossovers of the field reverse curves below the field forward curves. Since the carrier fluid was non magnetic, the response of the fluid must be entirely due to magnetic particles. So the hysteresis was not expected to show any new feature. We found one report of such measurements (i.e. viscosity during both increase and decrease of field) in the literature [109]. However, apart from obvious difference in behavior due to change in chemical nature of sample, they did not observe this cross over too. However, they did not impose saturation field like us, and we think – in the absence of any plausible explanation, this holds the key to the difference in behavior.

Looking minutely in the viscosities at final high magnetic fields, it is seen that there was

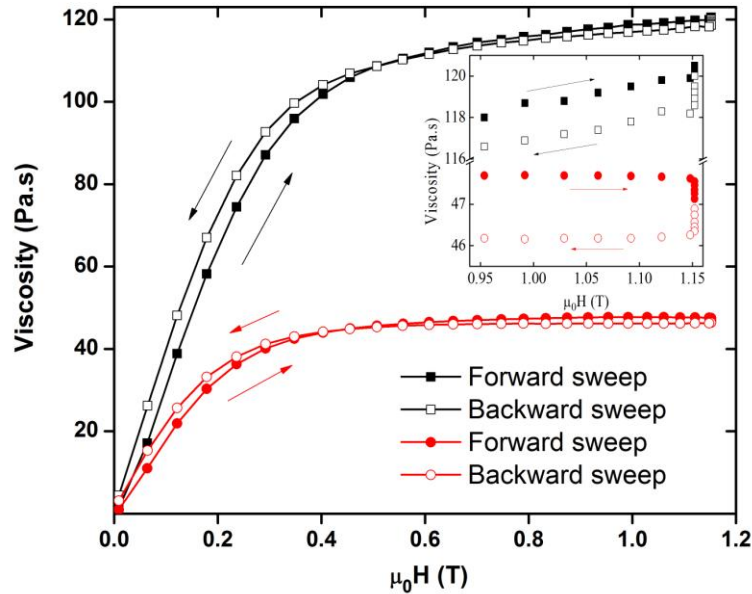


**Figure 6.5** Magnetic field sweep (viscosity vs. field) for MR1 (black square) and MR2 (red circle) at constant shear rate of  $10 \text{ s}^{-1}$ . Solid symbol represents increasing magnetic field, whereas open symbol stands for decreasing field. Inset, zoomed in portion of magnetosweep curves at higher fields.

a waiting time before the field direction was reversed. The fall in viscosity happened during then. While it is tempting to think that it was the fatigue, we think this was more likely due to rising local temperature effect [25]. Since the system spent some more time there at the same place, while under constant shear, and the viscosity was very high, so the liquid had some (local) temperature rise. Even if that must be a tiny effect, we found from the zoomed region (inset of Fig. 6.5) that there indeed was a fall in both cases at the extreme right field, thus corroborating our view. Once the field was reduced, the viscosity was restored to the value corresponding to  $25^\circ\text{C}$ , but this took some time. The relaxation went on for some time till the values matched the rising values, and then the memory effect took over. The structure was stronger in the return leg of the journey, and so the viscosity was higher.

### 6.3.1.3 Static and dynamic yield stress

Static yield stress ( $\tau_{ys}$ ) is defined as the minimum non-zero shear stress required to break the field-induced particle chain structures formed under influence of magnetic field and initiate the flow. Therefore, it is an important magnetorheological parameter often used to

characterize MR fluid's strength. While theoretically it is the value at zero stress rate, it is not practicable to measure it this way. Rather, it is taken from the value of shear stress at lowest measured shear rate ( $10^{-3}$ - $10^{-1} s^{-1}$ ). On the other hand, dynamic yield stress ( $\tau_{yd}$ ) is obtained by fitting the rheograms at higher stress rates with Bingham equation,  $\tau = \tau_b + \eta_p \dot{\gamma}$  where  $\eta_p$  is plastic viscosity [106]. Therefore, this is the extrapolated value at which the plastic flow would have occurred first. Since this is the major portion in the strain-strain rate curve in which the intended device will operate, it is also a very important parameter. The representative graph of static and dynamic yield stresses for MR1 and MR2 as a function of magnetic fields is shown in Fig. 6.6. As expected,  $\tau_{yd}$  are always

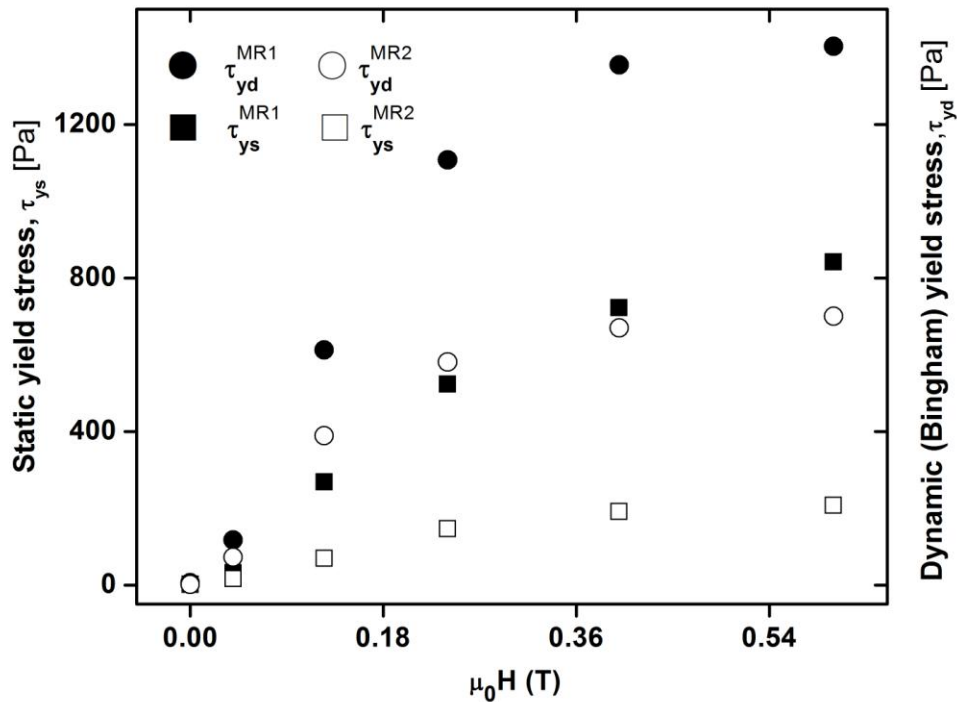


**Figure 6.6** Static ( $\tau_{ys}$ ) and dynamic yield stress ( $\tau_{yd}$ ) for both the samples MR1 (closed symbols) and MR2 (open symbols) are plotted as a function of magnetic field. Square symbols represent static yield stress whereas circular symbols denote dynamic yield stress.

higher than  $\tau_{ys}$ , and within the measurement range, they increased continuously with applied field. To understand the origin of both types of yield stresses in the MR fluid, we tried to find the relationship with magnetic field. Ginder's law ( $\tau_{ys} \propto H^{3/2}$ ) is such a well-known relation that predicts a power-law behavior for yield stress versus magnetic field

( $H$ ) [48]. This is plotted in Fig. 6.7A. In this case we find that an  $H^{3/2}$  dependence of yield stress was obtained up to an intermediate field region but that broke down in higher field. This was observed before [110]. There is an alternative relation to the fit. According to Klingenberg et al. [49], a better fit can be observed when ( $M^{1/2}H^{3/2}$ ) is replaced by  $M^2$  and it is applicable to wide range of  $M$ . This is plotted in Fig. 6.7B, with both types of  $\tau$  and

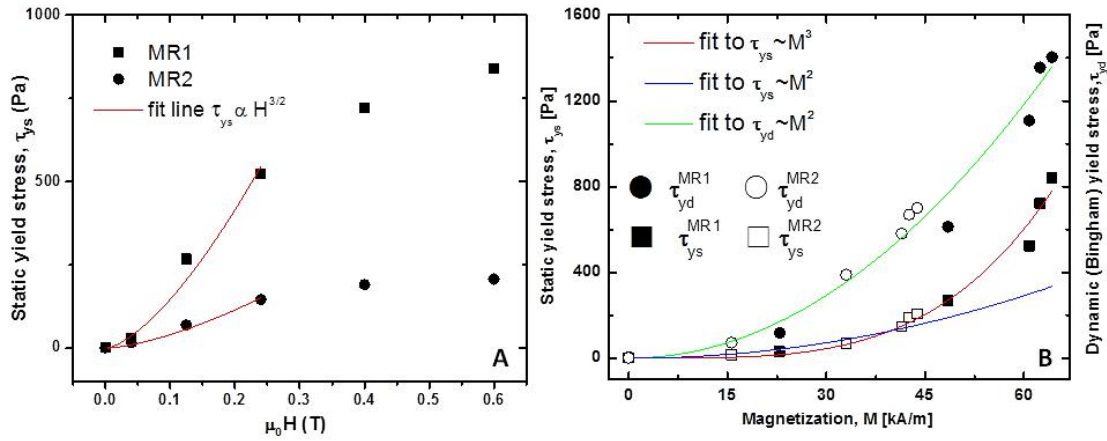


**Figure 6.7** (A) Static yield stress versus magnetic field curves for MR1 and MR2. The fit lines represent Ginder's relation:  $\tau_{ys} \propto H^{3/2}$  (B) Field-induced static (square) and dynamic (circle) yield stress for MR samples MR1 (solid symbol) and MR2 (open symbol) as a function of magnetization  $M$ .

$M$  values calculated from powder magnetization data ( $M$ - $H$  curves, vide Fig. 6.3). It can be seen that while the  $\tau_{yd}$  values fitted reasonably with  $M^2$  for both the concentrations, the static values matched better with  $M^3$ , a higher power than with  $M^2$ . This unexpected behavior may be explained as follows. The fit to  $M^2$  was obtained by assuming simple spherical dipoles arranged linearly in the magnetic field [49]. However, in the present case, because the particles were not fully spherical, we can assume that they were not arranged exactly linearly (i.e. centers lying on top of each other in a line but only in a general direction). This individual direction could also be alternately arranged around the imaginary axis. This distortion would produce multipolar interaction, with  $n > 2$ . It is not unlike three spin correlation, or even Dzyaloshinskii–Moriya type interaction, we cannot specify what. This stronger interaction was operative in the static case only. In the other case, the fluid had already reached plastic limit and the columnar structure was disrupted by then. Therefore interaction among the individual magnetic particles became mostly dipolar type ( $M^2$ ).

### 6.3.1.4 Oscillatory magnetorheology

Oscillatory dynamic measurements are performed to explore the dynamic viscoelastic behavior of the fluids. Both amplitude and frequency sweeps were carried on the two samples under the same three magnetic field values. In case of amplitude sweeps, samples were subjected to constant frequency (10 Hz) sinusoidal deformations and responses were recorded various oscillatory shear regions over a period of time. Linear viscoelastic regime (LVR) was observed at a very small strain amplitude ( $\gamma_0 \approx 10^{-1}$ - $10^{-3}$ ) where the viscoelastic moduli were largely independent of strain amplitudes. However, as stress amplitude was increased beyond a critical strain ( $\gamma_c$ ), these moduli became dependent on strain and drooped [111]. The behaviors are shown in Fig. 6.8 (A) and Fig. 6.8 (B). The dependence of the moduli on magnetic field is obvious.  $G'$  and  $G''$  increased

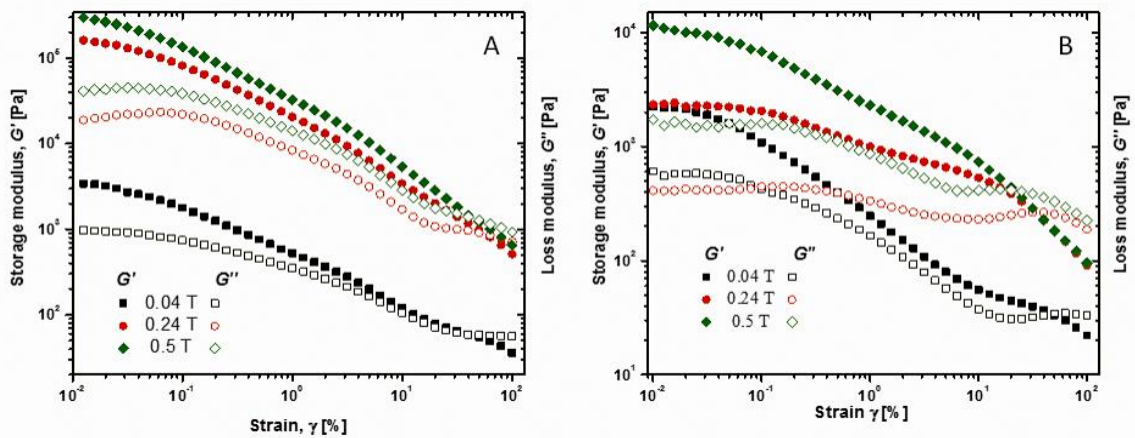


**Figure 6.8** (A) Amplitude sweep of MR1 at a constant frequency of 10 Hz under different magnetic fields. Filled symbol indicates storage modulus ( $G'$ ), whereas open symbol is for loss modulus ( $G''$ ). (B) Amplitude sweep of MR2 at 10 Hz under different magnetic fields.

as the field was increased, however, initially there was an order of magnitude increase in the moduli when the field was varied by 6 fold, but the difference steadily became less as the strain was increased, implying loss of elasticity. One interesting difference between the behaviors of the two liquids is that in case of MR1 (sample with higher concentration), the linear viscoelastic range is not very clear, unlike in case of MR2. This apparent ambiguity can be explained by the fact that the structures formed under higher fields were more prone to be affected by strain amplitude. The plateau at linear regions appeared not because of systematic deformation of particle chain junction, but rather microscopic movements and minor twisting within the chain network [112]. It is

interesting to note that at high strain, second pseudo-plateau regions of  $G''$  appear for both fluids. This quasi-linear viscoelastic region signifies the homogeneous rupture of particle networks and an eventual increment in loss modulus ( $G''$ ). For MR1, second pseudo-plateau appeared to be less prominent with increasing field. Beyond this, a crossover point ( $G' = G''$ ) appeared marking transformation into flow regime. This is akin to glass transition observed for polymer melts and the like. This was where the systems went over from gel like to liquid like structure. A further important observation is the bunching of  $G'$  and  $G''$  in this liquid region. This was only natural, for now the flow behavior is liquid like.

Frequency-dependence of the viscoelastic moduli for MR1 and MR2 was performed at a fixed strain,  $\gamma$  of 0.02% (Fig. 6.9). This was much below the range of critical strain,  $\gamma_c$ . As

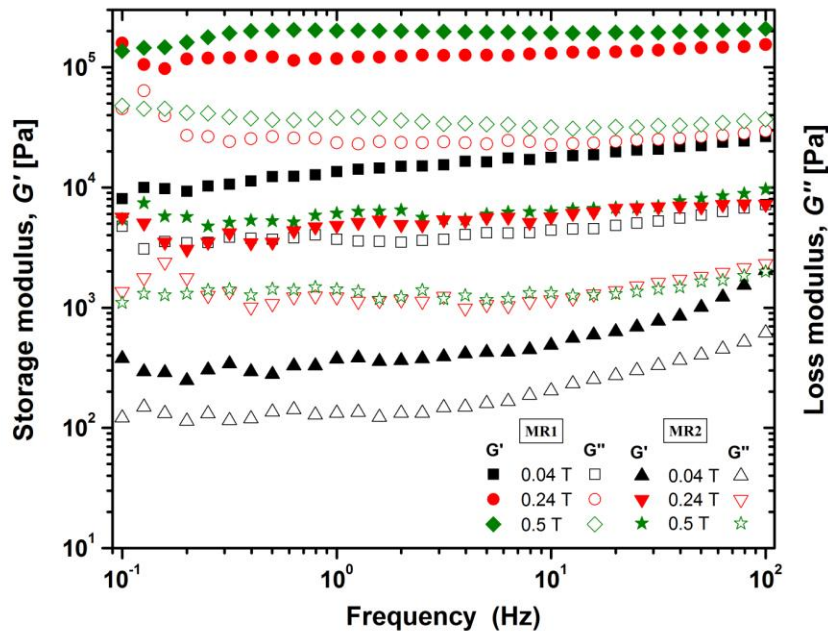


**Figure 6.9** Frequency sweep test at constant strain amplitude of 0.02% for the samples MR1 and MR2 under different magnetic field. Solid symbol indicates storage modulus ( $G'$ ) whereas, open symbol is for loss modulus ( $G''$ ).

found in the previous experiment the range was 0.05 to 0.5%. These measurements provide information about the effect of interactions among particles in the fluid. In linear viscoelastic regime (small deformation,  $\gamma \ll 1$ ), microstructures retain strongly elastic

behavior contributed by percolated and free suspension aggregates. At higher particle concentration (MR1) and field, structural rigidity of percolated aggregates can be explained by cage formation [112], i.e. particles formed rigid cage-like structures which accounts for frequency-independent  $G'$ . The contribution of carrier fluid was also responsible for linear dependence of  $G''$  at higher driving frequency [113]. Coupling these information, we conclude that the system showed behavior expected from a structured or solid-like material.

### 6.3.1.5 Temperature-dependent magnetorheology: introduction to scaling parameters

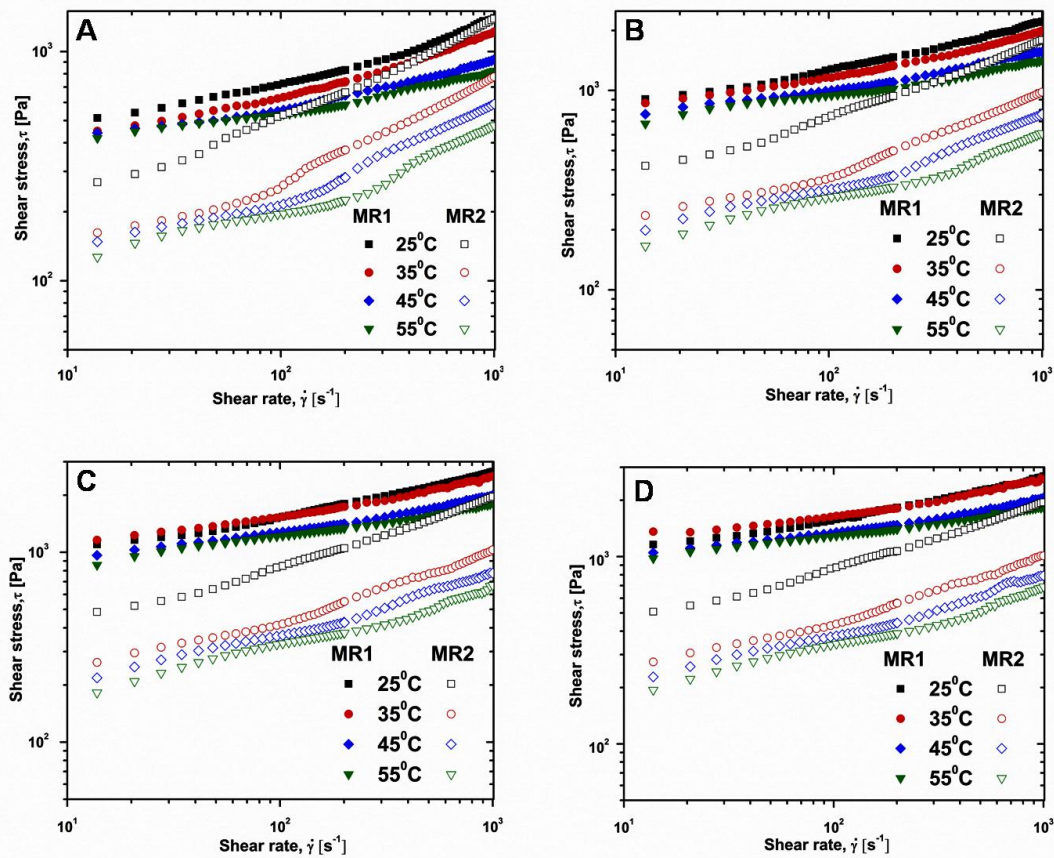


**Figure 6.10** Flow curves of magnetorheological shear stress ( $\tau$ ) as a function of shear rate ( $\dot{\gamma}$ ) and temperature for MR1 (closed symbols) and MR2 (open symbols) under various magnetic fields: (A) 0.125T, (B) 0.24T, (C) 0.4T and (D) 0.6T.

The effect of temperature on shear stress of MR fluids (MR1 and MR2) is presented in Fig. 6.10 for different magnetic fields. The measurements were performed within the temperature range of 25°C-55°C. Shear stress (as a function of shear rate) is observed to

decrease systematically with elevation of temperature and is applicable to all the values of magnetic fields. The dynamic yield stress ( $\tau_{yd}$ ) is calculated by fitting the shear stress vs. shear rate curves with Bingham equation.

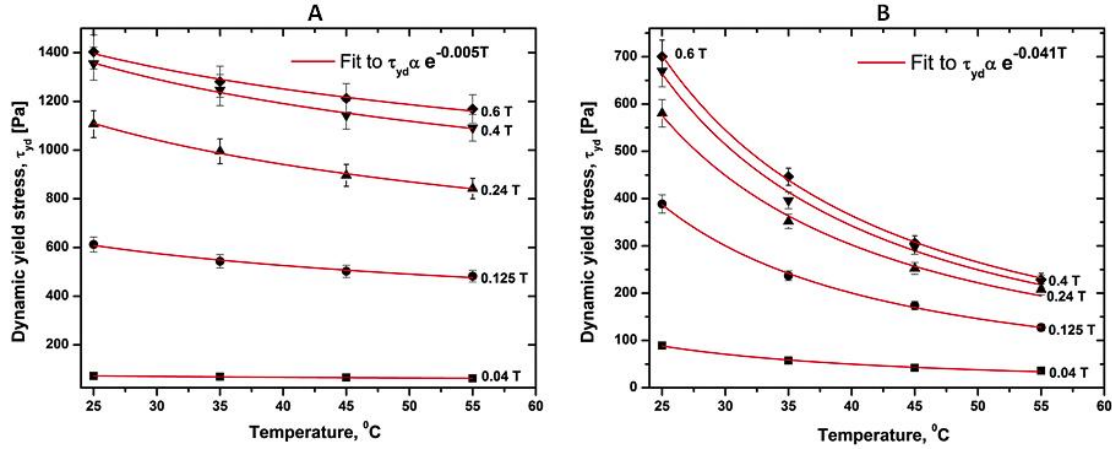


**Figure 6.11** Bingham or dynamic yield stress plotted as a function of temperature (25°C -55°C) under various magnetic fields for (A) MR1 and (B) MR2. Data fitting lines represent exponential decay with temperature.

Since this is the major portion in the stress-shear rate curve in which the MR devices operate, it is a very important parameter. The effect of temperature on magnetorheological yield stress is evaluated for five levels of magnetic fields and shown in Fig. 6.11A and 6.11B for MR1 and MR2, respectively. It is obvious that yield stress depends significantly on temperature. Therefore, an extended form of Bingham equation can be rewritten as follows:

$$\tau(\dot{\gamma}, B, T) = \tau_{yd}(B, T) + \eta_p \dot{\gamma} \quad (6.1)$$

The trend in dynamic yield stress with temperature is explained by an exponential decay function for  $\tau_{yd}$  and the fits are reasonably good with the fitting function  $\tau_{yd} = Ke^{-bT}$  (6.2) where  $K$  and  $b$  are empirical constant,  $T$  is temperature in K. The exponential relationship between yield stress and temperature can be originated from the Arrhenius type relationship between viscosity and temperature:  $\eta = Ae^{-\frac{E_a}{RT}}$  (6.3) where,  $R$  is universal gas constant,  $A$  is a constant,  $T$  is temperature in K and  $E_a$  is activation energy to initiate flow. This relation provides reasonable justification to the observed trend in viscosity with temperature and the fact that viscosity and yield stress are associated with the flow behavior of the material, a similar exponential relationship can also be used for

dynamic yield stress as shown in Fig. 6.11A and 6.11B [114]. The proposed model provides a good agreement with all experimental data for both MR1 and MR2. The change in yield stress with temperature is more pronounced for MR2 with the value of exponential decay constant ( $b$ ) of  $0.041 \text{ K}^{-1}$  whereas, a lesser rapid change in  $\tau_{yd}$  is observed for MR1 with the  $b$  value of  $0.005 \text{ K}^{-1}$ . One possible explanation for a more rapid reduction in yield stress may be the effect of temperature on the volume fraction of ferromagnetic CoNi nanospheres dispersed in carrier fluid. Since castor oil has higher thermal expansion coefficient than dispersed phase, with increasing temperature the effective volume fraction occupied by particles decreases [115]. Using the following relation, one can calculate normalized thermal sensitivity of suspensions:

$$S_{\phi} = \lim_{\Delta T \rightarrow 0} \frac{1}{\phi_0} \frac{\phi_f - \phi_0}{\Delta T} = (1 - \phi_0)(\alpha_p - \alpha_f) \quad (6.4)$$

Where  $\phi_0$ ,  $\phi_f$ ,  $\alpha_p$  and  $\alpha_f$  are initial volume fraction, effective volume fraction, volumetric thermal expansion coefficients for particles and carrier fluid, respectively.

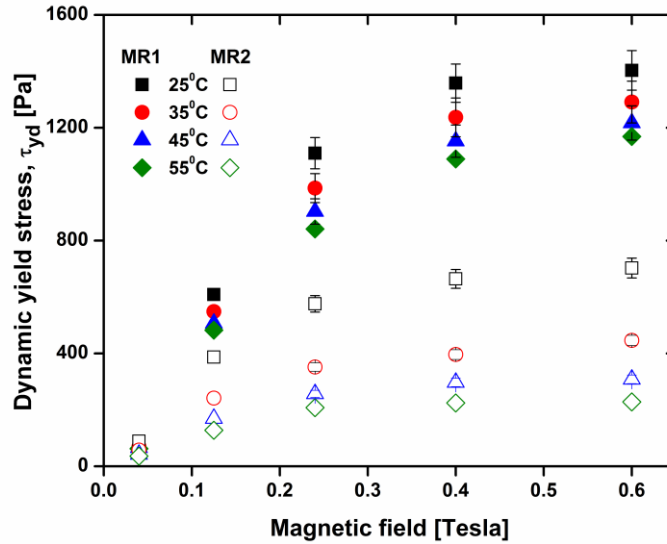


**Figure 6.12** Dynamic yield stresses of MR1 (closed symbols) and MR2 (open symbols) plotted as a function of magnetic field under different temperatures.

The cubic expansion coefficient of castor oil is found to be  $0.0007^{\circ}\text{C}^{-1}$  and for pure Co, it is approximately  $0.000039^{\circ}\text{C}^{-1}$  (calculated using linear expansion coefficient of Co obtained from ref. [116]). From the relation (6.4), we can now estimate the magnitude of

$S_\phi$  for MR1 and MR2 as  $5.3 \times 10^{-4}$  and  $5.6 \times 10^{-4}$ , respectively. It is obvious that MR2 shows higher normalized thermal sensitivity. Below a critical concentration of  $\phi_0 = 0.3$ , a linear variation in yield stress with volume fraction is reported. Therefore, this normalized thermal sensitivity is equal to the sensitivity of yield stress contributed by thermal expansion of carrier fluid. An increment of 5 volume% in concentration means the MR1 is 33% more concentrated than MR2. The recent works by Wereley et al. showed that the thermo-magnetorheological property, i.e. temperature-induced change in viscosity is exclusively a function of the change in viscosity of carrier fluid [117]. This means that if the carrier fluid viscosity-temperature relation is known, then the same relative change in viscosity will be present in a MR fluid made with that carrier liquid. The estimated change in yield stress for MR1 and MR2 can be interpreted in terms of change in viscosity of carrier fluid (castor oil). Since the change in volume fraction is higher in MR2, comparative change in viscosity with temperature can be higher, resulting in stronger temperature-thinning effect. Hence, MR2 with higher thermal sensitivity is expected to demonstrate a relatively stronger decay in temperature-dependent yield stress.

The trend in dynamic yield stress at a particular temperature is also illustrated as a function of magnetic field (Fig. 6.12). In both cases, the trend in viscoelastic parameters with temperature is worth noted. The observations indicate a temperature-thinning effect. This can be qualitatively explained by thermal vibration of the suspended nanoclusters with increasing temperature. According to Li et al. [118], magnetic particles acquire thermal energy at a given temperature. With increasing magnetic field, alignment of particles into chain-like structures decreases randomness. With increasing temperatures, due to increase in thermal energy, structures tended to break up. Therefore, a reduction in magnetorheological parameters followed. Both of these effects can be scaled by a dimensionless quantity  $\lambda$ , defined as a ratio of magnetostatic force to characteristic Brownian force acting on a particle:

$$\lambda = \frac{\pi\mu_0 a^3 M^2}{6k_B T}$$

where  $a$ ,  $M$ ,  $T$  are radius, saturation magnetization of a particle and K,  $\mu_0$  and  $k_B$  are temperature, vacuum permeability and Boltzmann constant respectively. Estimated  $\lambda$

values for these particles of size 450 nm at 55°C are  $\sim O(10^7)$  which implies a very negligible Brownian force contribution to stress. Therefore, thermal vibration of particle chains is insufficient to cause the observed changes in MR parameters. Hence, to understand the effect of temperatures, quantitative studies of the changes in rheological parameters are inevitable. The correlation is a direct output of a number of parameters describing the trend in yield stress, magnetization and carrier fluid viscosity as a function of temperature. Therefore, it is necessary to define those parameters and establish a quantitative analogy for the trends described above.

The reduction in yield stress ( $\tau_{yd}$ ) with temperature is described by introducing an average normal yield stress sensitivity parameter  $\langle S_\tau \rangle$  as following:

$$\langle S_\tau \rangle = \left( \frac{1}{\tau_{yd}^0} \right) \frac{\Delta \tau_{yd}}{\Delta T} \quad (6.5)$$

Where  $\tau_{yd}^0$  is yield stress at a reference temperature (25°C) and reference magnetic field (0.125 T) and  $\Delta \tau_{yd}$  is the change in yield stress correspond to change in temperature ( $\Delta T$ ). The experimentally calculated magnitude of  $\langle S_\tau \rangle$  under different temperatures and magnetic flux are listed in Table 6-1. The determined values for  $\langle S_\tau \rangle$  are observed to be comparable to other experimental results performed previously by Li et al., and Ocalan et al. [118, 115] Another important temperature-dependent parameter is magnetization. For ferromagnetic particles, saturation magnetization is a decreasing function of temperature below Curie point. For  $Co_{0.9}Ni_{0.1}$ , thermal sensitivity is expected to be very small as operating temperature window during magnetorheological studies are far below Curie temperature. Using the relation by Crangle and Goodman [119], the average sensitivity in saturation magnetization for the temperature range 25°C-55°C is calculated to be:

$$S_M = \frac{1}{M_s^0} \frac{\partial M_s}{\partial T} = 1.4 \times 10^{-4} / ^\circ C \quad (6.6)$$

The off-state viscosity of MR fluid is also strongly dependent on temperature and is related to carrier fluid viscosity. In the present study, castor oil was used for the preparation of MR suspensions. The change in carrier fluid viscosity with temperature is described in Fig. 6.13. It is observed that the trend follows Arrhenius relation.

**Table 6-1** Yield stress sensitivity parameter and scaling factor as a function of magnetic field and temperature.

<b>MR1</b>						
<b>B (T)</b>	<b>Average yield stress sensitivity</b>			<b>Yield stress scaling factor, <math>a_Y</math></b>		
	$ \langle S_\tau \rangle /10^3/^\circ\text{C}$					
	<b>25°C-35°C</b>	<b>25°C-45°C</b>	<b>25°C-55°C</b>	<b>25°C-35°C</b>	<b>25°C-45°C</b>	<b>25°C-55°C</b>
0.125	11.27	8.97	7.08	1.113	1.179	1.212
0.24	10.09	9.50	7.96	1.10	1.190	1.239
0.4	7.97	7.81	6.47	1.079	1.156	1.194
0.6	8.70	6.79	5.56	1.087	1.135	1.166

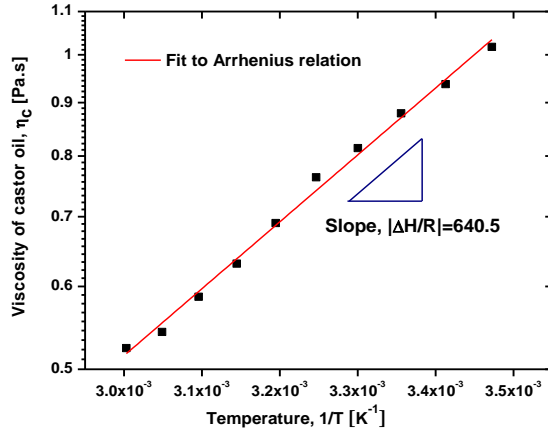
  

<b>MR2</b>						
<b>B(T)</b>	<b>Average yield stress sensitivity</b>			<b>Yield stress scaling factor, <math>a_Y</math></b>		
	$ \langle S_\tau \rangle /10^3/^\circ\text{C}$					
	<b>25°C-35°C</b>	<b>25°C-45°C</b>	<b>25°C-55°C</b>	<b>25°C-35°C</b>	<b>25°C-45°C</b>	<b>25°C-55°C</b>
0.125	39.02	27.64	22.37	1.390	1.553	1.671
0.24	39.38	28.26	21.39	1.394	1.565	1.641
0.4	40.85	27.80	22.15	1.408	1.556	1.664
0.6	36.27	28.14	22.47	1.363	1.563	1.674

The suspension viscosity of MR fluid in absence of magnetic field can also be approximated by Arrhenius equation:

$$\eta_\infty(T) = \eta_\infty(T_0) e^{\frac{\Delta H}{R} \left( \frac{1}{T} - \frac{1}{T_0} \right)} \quad (6.7)$$

Where  $\eta_\infty(T_0)$  and  $\eta_\infty(T)$  define infinite shear viscosity at a reference temperature  $T_0$  and at any arbitrary temperature  $T$ ,  $\Delta H$  is activation energy to flow and  $R$  is universal gas constant. To determine limiting viscosities at infinite shear rates, the experimental data of viscosity as a function of shear rate in absence of field for MR1 and MR2 were fitted



**Figure 6.13** Viscosity of castor oil is plotted as function of inverse absolute temperature ( $K^{-1}$ ). Fitted line represents Arrhenius equation. From the slope of the fitted curve, activation energy for carrier fluid is calculated to be 5.3 kJ/mol.

with Cross model equation (Fig. 6.14A and 6.14B), which describes pseudoplastic flow with asymptotic viscosities at zero ( $\eta_0$ ) and infinite ( $\eta_\infty$ ) shear rates:

$$\eta(\dot{\gamma}) = \eta_\infty + (\eta_0 - \eta_\infty) \frac{1}{1 + (\lambda\dot{\gamma})^m} \quad (6.8)$$

Where,  $\eta(\dot{\gamma})$ ,  $\lambda$  and  $m$  are apparent viscosity, characteristic time constant with unit of time and dimensionless exponent of Cross equation signifying the width of transition between zero-shear viscosity and power-law plateau region of the viscosity curve, respectively [120]. The quantities  $\eta_0$ ,  $\eta_\infty$ ,  $\lambda$  and  $m$  are all fitting parameters and shown in Table 6-2.

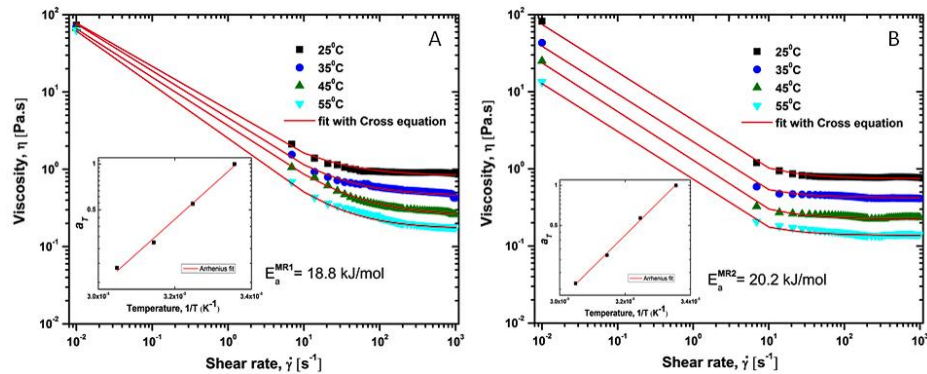


**Figure 6.14** Zero-field apparent viscosities of (A) MR1 and (B) MR2 are plotted as a function of shear rate under different operating temperature. Fitted lines represent the same calculated from Cross rheological model equation. In the inset,  $a_T$  is plotted against inverse of absolute temperature ( $K^{-1}$ ). Fitted line represents Arrhenius equation.

**Table 6-2** Cross equation fitting parameters for off-field viscosities of MR1 and MR2 with increasing temperature.

Temperature	25°C		35°C		45°C		55°C	
	MR1	MR2	MR1	MR2	MR1	MR2	MR1	MR2
<b>Fitting parameter</b>								
$\eta_0$ (Pa.s)	156.4	137.37	150.4	94.4	148.3	65.5	135.7	35.87
$\eta_\infty$ (Pa.s)	0.82	0.745	0.45	0.423	0.25	0.223	0.17	0.137
$\lambda$ (s)	33.5	58.6	35.6	98.24	41.7	107.34	57.8	115.54
<b>m</b>	0.76	0.83	0.78	0.81	0.78	0.8	0.76	0.82

Therefore, all parameters sensitive to temperature and magnetic field collectively account for the significant changes in magnetorheological parameters at high temperatures. In order to generalize the collective response of the fluid systems at high temperature and magnetic field, the data from Fig. 6.10 can be made to collapse into a single master curve. The fact that isothermal curves for shear stress variation with different magnetic field as a function of shear rate can be superimposed implying a dynamically self-similar system response [121]. The rheogram at the temperature 25°C and magnetic field 0.125T was chosen to be the reference curve and other rheograms were scaled with the help of the shift parameters [122]. The yield stress shift parameter ( $a_Y$ ), magnetization shift factor ( $a_M$ ) and thermo-viscous shift parameter ( $a_T$ ) are defined as follows:

1.  $a_Y = 1 + \langle S_\tau \rangle \Delta T$ , where  $\langle S_\tau \rangle$  is average yield stress sensitivity parameter and  $\Delta T$  is change in temperature with respect to reference temperature ( $T_0$ ).
2.  $a_Y = \frac{M}{M_0}$ , where  $M_0$  is reference magnetization at reference magnetic field (0.125T) corresponds to reference obtained from powder magnetization data.
3.  $a_T = \frac{\eta_\infty(T)}{\eta_\infty(T_0)} = e^{\frac{\Delta H}{R} \left( \frac{1}{T} - \frac{1}{T_0} \right)}$ , which is defined as the ratio of fluid viscosity at infinite shear rate ( $\eta_\infty$ ) under a certain temperature to that of the  $\eta_\infty$  at reference temperature ( $T_0$ ).

Since suspension viscosity arises due to the viscous drag on particle chain network, therefore,  $a_T$  is defined by the ratio of viscosity of fluids under flowing condition and not by the ratio of zero shear viscosity.

To generate satisfactory time-temperature-field superposition, the above shift factors should be utilized to calculate the reduced or scaled shear stress and shear rate. Therefore, scaled shear stress ( $\tau_{sc}$ ) and shear rate ( $\dot{\gamma}_{sc}$ ) can be represented as follows:

$$\tau_{sc} = \frac{\tau}{a_T a_M} \quad (6.9)$$

$$\dot{\gamma}_{sc} = \frac{\dot{\gamma}}{a_T a_M} \quad (6.10)$$

Where,  $\tau$  and  $\dot{\gamma}$  represent actual shear stress and shear rate respectively.

The resulting master curves for MR1 and MR2 are shown in Fig. 6.15. The superposition is very well for both MR1 and MR2. It can be concluded that physical processes responsible for changes in temperature-dependent MR behavior can be successfully explained by magnetic and thermal shift parameters. The collapse of the rheograms into a single master curve indicates a better correlation of reference yield stress ( $\tau_{yd}^0$ ) to reference magnetization ( $M_0$ ) and reference temperature ( $T_0$ ).

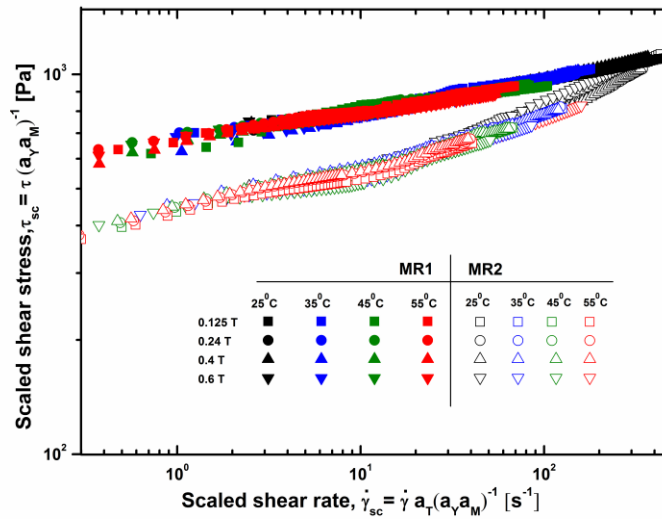


**Figure 6.15** Magnetorheological master curves for MR1 (closed symbols) and MR2 (open symbols) are shown as a function of scaled shear stress ( $\tau_{sc}$ ) and shear rate ( $\dot{\gamma}_{sc}$ ). The scaling parameters were derived considering the dependence of stress parameters on temperature and magnetic field.

Master curves for MR1 and MR2 at reference temperature of represent material function (shear stress) as they would have been calculated at broad ranges of operating shear rates. The collapsing of data points for samples under various magnetic fields and temperature implies the extension of shear rate range which was beyond the experimental scope. Therefore, the reference yield stress at a reference temperature and magnetic field is known, magnetorheological shear stress at any arbitrary temperature and field can be calculated using the master equation:  $\tau(T, M) = \tau_{yd}^0(1 + \langle S_\tau \rangle \Delta T) \left( \frac{M}{M_0} \right)$  (6.11)

The only other parameter that was not taken into account in the above scaling is the concentration of suspension. That is why the data points of the two concentrations lie on two different bands. However, since the major characteristic of the data points have already been taken care of, we leave it at that.

## 6.4 Conclusions

In this chapter, we investigated the structure, morphology and magnetorheology of Co-rich NiCo alloyed microclusters. The behaviors of static and dynamic yield stresses for these MR fluids were found to depend on average particle magnetization, with the static yield stress dependence on  $M$  being stronger of the two. Magnetosweep studies demonstrated an interesting relaxation phenomenon that was interpreted as an effect of local temperature rise within the fluid at high field and at constant shear rate. The temperature-dependent MR characterization has shown a decline in MR properties at elevated temperatures for both samples of Co-rich NiCo microclusters. Considering the thermal sensitivity of yield stress, magnetic saturation of powder  $\text{Co}_{0.9}\text{Ni}_{0.1}$  and matrix fluid viscosity at elevated temperature, it was shown that change in carrier fluid viscosity with temperature significantly affects the overall fluid performance. We have also shown that time-temperature-field superposition method is applicable for the two MR suspensions with different  $\text{Co}_{0.9}\text{Ni}_{0.1}$  volume fractions. The master curves generated for both the fluids with respect to a reference temperature, reference magnetization and reference yield stress, indicated a good correlation between the individual sensitivity parameters that were affected differently with increasing temperature.

# 7

## Chapter 7

### **Investigations on Fe<sub>3</sub>Ni-based systems: structure, morphology and magnetorheology**

*This chapter describes the morphological and structural characterizations of Fe-rich PAA-Fe<sub>3</sub>Ni alloyed microspheres synthesized by polyol reduction with scanning electron microscopy and X-ray diffraction studies. Magnetorheological fluid was made by dispersing the 10 volume% particles in castor oil. The room temperature viscoelastic characterization of the fluid was performed under different magnetic fields. The field-dependent yield stresses were scaled using existing models and it was found that static yield stress was more accurately described by an  $M^3$ -dependence. Temperature-dependent oscillatory rheological studies under various fields were also investigated. This demonstrated a strong temperature-induced thinning effect.*

## 7.1 Introduction

In this chapter we discuss FeNi based microparticles for use in magnetorheology. In addition to FeCo and NiCo, FeNi alloys are of great interest due to diverse magnetic properties dependent on shapes and compositions [123]. Notably, FeNi is a soft magnetic material with high saturation magnetization, low coercivity [123], high magnetic permeability, low thermal expansion [124], and excellent corrosion resistance [125]. It was shown before that for both bulk and nano-size, magnetic properties for FeNi alloys with a specific composition are a function of different combination of *bcc* and *fcc* phases. In practice, when two phases coexist, the relative amount/percentage so obtained appears also to depend on the preparation method [124].

To improve the applicability of FeNi alloyed microparticles in MR fluidic applications, it is necessary to modify and functionalize surfaces of particles so as to increase the soft magnetic properties for custom MR application. These structures are classified as composites microstructures. Composite materials offer distinct multifunctional properties which could be optimized for desired applications. Metal alloy-polymer composites exhibit excellent physical, chemical, and mechanical properties that single phase materials do not possess.

In this chapter, we report the MR preparation and characterization of Fe<sub>3</sub>Ni-based magnetorheological fluids which has not been studied so far. While Fe-rich alloy systems with considerably high saturation magnetization enhance MR effect significantly, PAA-encapsulation offers higher sedimentation stability as well as chemical stabilization from oxidation. Steady shear magnetorheological studies reveal desired MR response under increasing magnetic field. The field-induced stress relaxation measurements provide useful insight into on-field structuration and subsequent relaxation upon removal of field. The temperature dependent oscillatory magnetorheology are also performed with 10 vol% MR fluid containing PAA-Fe<sub>3</sub>Ni. Temperature-induced thinning effect in MR properties is evident for the samples under investigation.

## 7.2 Structure and morphology of particles

### 7.2.1 SEM, x-ray diffraction studies and VSM

The morphology, composition and crystal structures of as-prepared  $\text{Fe}_3\text{Ni}$  are investigated using FESEM, EDAX and XRD. The low and high magnification FESEM images of  $\text{Fe}_3\text{Ni}$  are shown in Fig. 7.1A and 7.1B. Images show well-dispersed spherical  $\text{Fe}_3\text{Ni}$ -nanocomposite particles prepared using PAA polymer. Sub-micron sized  $\text{Fe}_3\text{Ni}$  microparticles are secondary particles formed by nucleation and subsequent growth of primary nanoparticles thus formed. The surface of microspheres appeared to be rough,

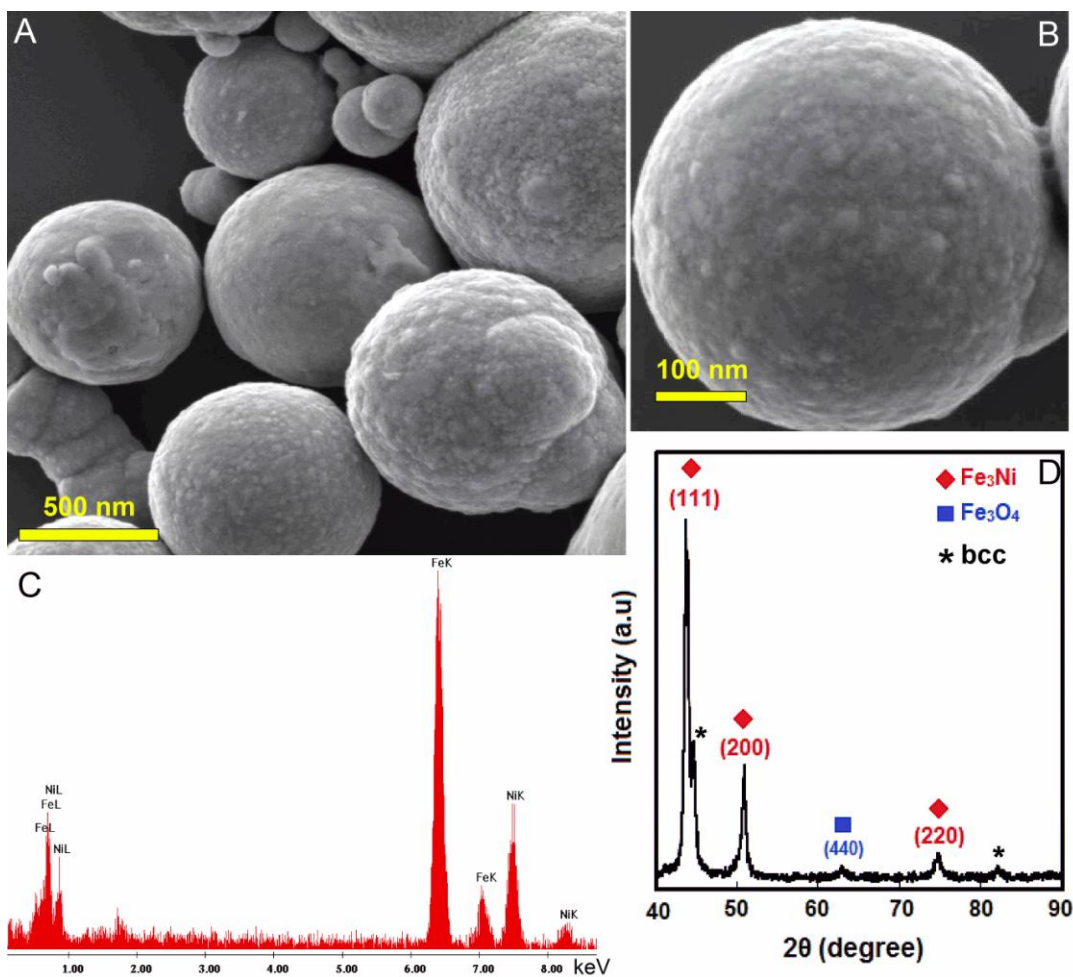


**Figure 7.1** (A,B) Low and high magnification FESEM images of PAA- $\text{Fe}_3\text{Ni}$ , (C) EDAX spectra and (D) X-ray diffraction patterns of  $\text{Fe}_3\text{Ni}$  microspheres.

owing to polymer encapsulation during the growth phase. The average (mean) diameter of  $\text{Fe}_3\text{Ni}$  was found to be 700 nm. The composition of alloyed microparticles were determined by EDAX analysis and shown in Fig. 7.1C. It confirms the final composition

of Fe<sub>3</sub>Ni is consistent with the initial molar concentrations of metal salts. The material is, therefore, nearly uniform Fe<sub>3</sub>Ni solid solution of Ni in Fe with very little deviation in composition for different sized particles. The different of crystal phases of as-synthesized Fe<sub>3</sub>Ni powder is characterized by XRD, and the XRD patterns of sample is shown in Fig. 7.1D. This indicates the alloy formation with mixed *fcc* and *bcc* phases. Three characteristic peaks for *fcc* Fe<sub>3</sub>Ni ( $2\theta = 44.1^\circ, 51.5^\circ, 76.1^\circ$ ), corresponding to Miller indices (111), (200), (220) are observed, whereas, peaks associated to *bcc* structure are also indexed. However, in addition to Fe<sub>3</sub>Ni, peak corresponds to Fe<sub>3</sub>O<sub>4</sub> can also be detected, as unreacted Fe may form oxides during the reaction. This indicates the presence of Fe<sup>2+</sup> and Fe<sup>3+</sup> in the sample. The average size of the crystalline domains (coherently diffracting domains) of the sample is calculated from the broadening of the (111) X-ray diffraction peak using the Scherrer equation [126]:  $\beta_{hkl} = \frac{k \cdot \lambda}{L_{hkl} \cos \theta}$ , where  $\beta_{hkl}$  is the broadening of the diffraction line measured at full width half maximum intensity (FWHM),  $\lambda$  is the X-ray wavelength,  $L_{hkl}$  is the crystal size and  $\theta$  is the diffraction angle,  $k$  is the Scherrer shape factor ( $k = 0.9$  for the calculations). The calculated average crystallite size for the as-prepared Fe<sub>3</sub>Ni is  $38 \pm 5$  nm. The room

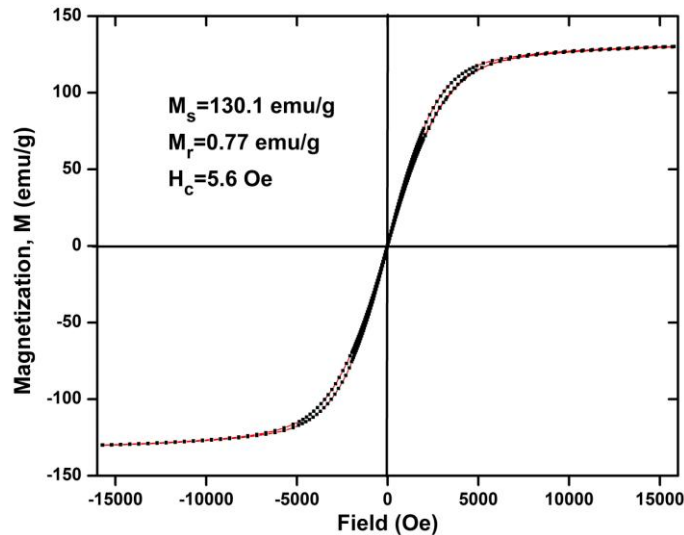


**Figure 7.2** Room temperature M-H hysteresis curve of PAA-Fe<sub>3</sub>Ni sample

temperature magnetization studies (Fig. 7.2) in vibrating sample magnetometry (M-H curve) show that the material is magnetically soft with low coercivity ( $H_c$ ) and remanence

( $M_r$ ) whereas, saturation magnetization ( $M_s$ ) is quite high. The  $H_c$ ,  $M_r$  and  $M_s$  values of the sample were found to be 5.62 Oe, 0.77  $emu/g$  and 130.1  $emu/g$ , respectively.

### 7.3 Magnetorheological studies

#### 7.3.1 Steady shear magnetorheology in PAA-Fe<sub>3</sub>Ni based MR fluid

Rheological measurements were carried out under different magnetic fields, ranging from 0 to 0.5T under steady shear mode. Shear stresses are plotted as a function of shear rate for MRF containing 10 vol% of PAA-FeNi microspheres under different magnetic field as shown in Fig. 7.3. The rheograms show the magnetorheological behavior with shear stress increasing systematically with shear rate. The rheograms show a typical plastic behavior, characterized by field-dependent (dynamic) yield stress. Dynamic or Bingham yield stress is calculated according to Bingham equation,

$$\tau = \tau_{yd} + \eta\dot{\gamma},$$

where  $\tau$ ,  $\tau_{yd}$ ,  $\eta$  and  $\dot{\gamma}$  represent shear stress, dynamic yield stress, viscosity and shear rate, respectively. The data points in the measurements are divided into two different shear rate windows, one at low shear rate (0.001-10  $s^{-1}$ ) and another in the high shear regime, lying in the range of 10-1000  $s^{-1}$ .

These two shear regimes account for two types of yield stresses. The zoomed in section of rheogram in the 0.05-10  $s^{-1}$  is shown in the inset of Fig. 7.3. The dynamic yield stress was estimated from Bingham equation in the high range. In absence of field, MRF possessed non-zero yield stress under low shear rate and it increased with increasing magnitude of the applied field. As polymer (PAA)-assisted growth of microspheres introduced surface roughness, strong chain-like microstructures were formed due to intense particle-particle interaction under shear. Increasing magnetic field strength also facilitated stronger interaction, thus giving rise to higher field-dependent yield stress. In Fig. 7.4, static and dynamic yield stresses of the MRF are shown as a function of particle

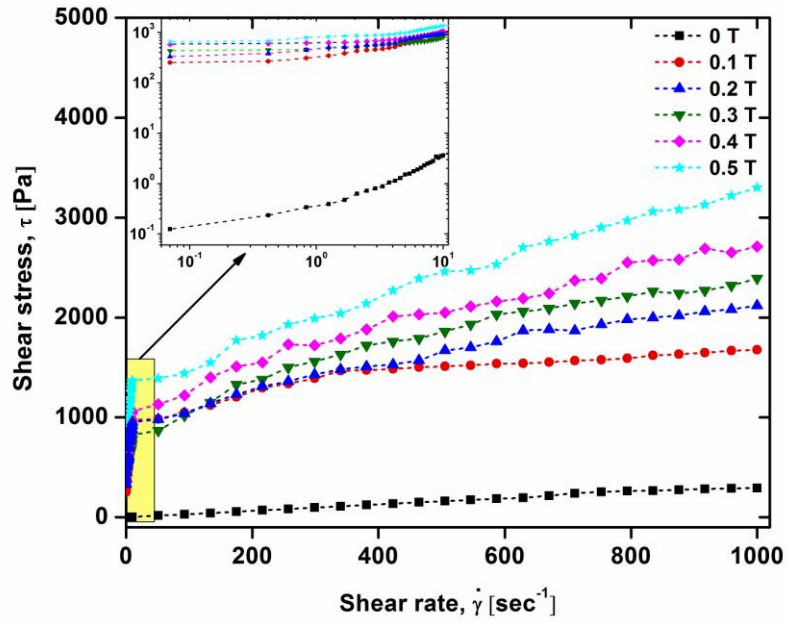


**Figure 7.3** steady shear rheological behaviors of MR fluids for different magnetic fields.

magnetization extracted from powder magnetization data. As before (chapter 6), yield stress correlation was done with the help of particle magnetization ( $M$ ).

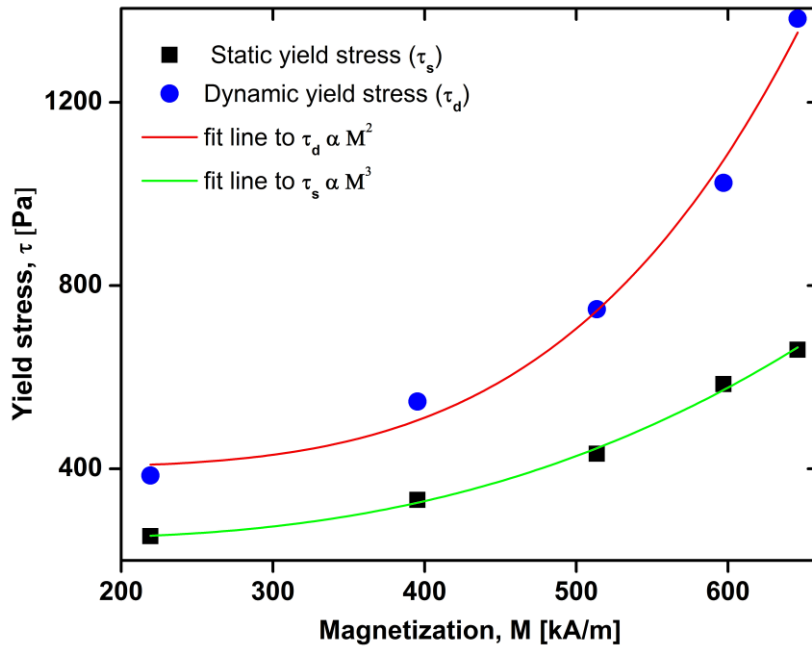


**Figure 7.4** Field-induced static (square) and dynamic (circle) yield stress for MR sample as a function of magnetization  $M$ .

As demonstrated previously (chapter 6), it is again observed that while the  $\tau_{yd}$  values fitted reasonably well with  $M^2$  for both the concentrations, the static values are better scaled with  $\sim M^3$ . The explanation to this behavior was as given previously.

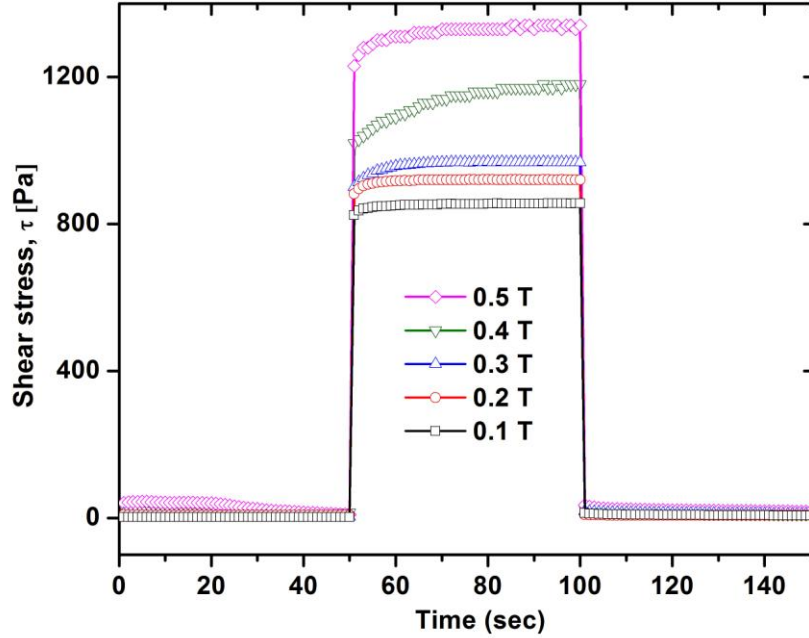


**Figure 7.5** Field-induced shear stress relaxations for MR sample as a function of time.

To test the relaxation effects in the system, which is complimentary to the previously stated experiment, shear stress relaxations with time as a function of magnetic field were carried out and the results are shown in Fig. 7.5. The field-induced relaxation of stress was observed at room temperatures under constant shear rate ( $10 \text{ s}^{-1}$ ). The timescale was divided into three timescale zones; in the first and third zones, field was set to be zero whereas in intermediate zone, magnetic fields in the range  $0.1 \text{ T} - 0.5 \text{ T}$  were applied. Time delays for data acquisition were  $1 \text{ s}$  for all the data points. An obvious trend in field-induced stress was observed in the on-field region as with high field, strongly aggregated particle networks yielded higher stress. As soon as the field was switched on, instantaneous jumps in shear stress occurred owing to field-induced aggregation of microspheres. Since the timescale of data acquisition was much faster than the structural relaxation (relaxation time), we observed an immediate fall after the field was switched off. The characteristic relaxation time increased with increasing magnetic field. This phenomenon also demonstrated the reversibility of the microstructure formation.

### 7.3.2 Temperature-dependent oscillatory rheological studies

In order to evaluate the field-induced viscoelastic behavior of the sample, when subjected to a continuous rise in temperature and magnetic field, an oscillatory temperature ramp test was performed (Fig. 7.6). From this test, the variations of the  $G'$  and  $G''$  moduli (Fig. 7.6A and 7.6B) were obtained, as a function of temperature and field, at a 0.02% strain and at a 10 Hz frequency, with a heating rate of  $2^{\circ}\text{C}\cdot\text{min}^{-1}$ . It is observed from the figures that the fluid retained strongly elastic behavior throughout the ranges of temperature ( $20^{\circ}\text{C}$ - $55^{\circ}\text{C}$ ), i.e.  $G' > G''$  in the temperature range specified for the measurement. The magnitude of  $G'$  and  $G''$  at a particular field was consistent with the idea that stronger field-induced structuration drives the modulus to a higher initial values. The effect of temperature is also obvious, i.e. a significant temperature-induced thinning was observed for all fields. However, magnitude of slopes of moduli versus temperature curves in presence of fields were much higher in magnitude than that of the zero field as aggregated structures tended to be more affected by the changes in temperature. This maybe explained in terms of higher initial field-dependent stresses. The temperature thinning effect could be due to the previously stated reasons, like the change in particle saturation magnetization, effect of change in carrier fluid viscosity with increasing temperature etc. On further examination, it appears that all these effects combined to produce significant temperature thinning effect for moduli under magnetic fields whereas the off-field moduli seem to be affected solely due to the changes in carrier fluid viscosity with temperature. However, in the  $\tan \delta$  ( $G''/G'$ ) versus temperature plot (Fig. 7.6C), we observe no clear trend and no peaks associated to glass-transition like phenomena under the conditions specified. This may be due to the fact that applied strain was in LVR region, so the sample retained its strongly elastic nature ( $G' > G''$ ) throughout the temperature window. Figure 7.6D illustrates the change in complex viscosity as a function of temperature. Similar to storage modulus, complex viscosity too displayed temperature induced softening, i.e. viscosity decreases with increasing temperature.

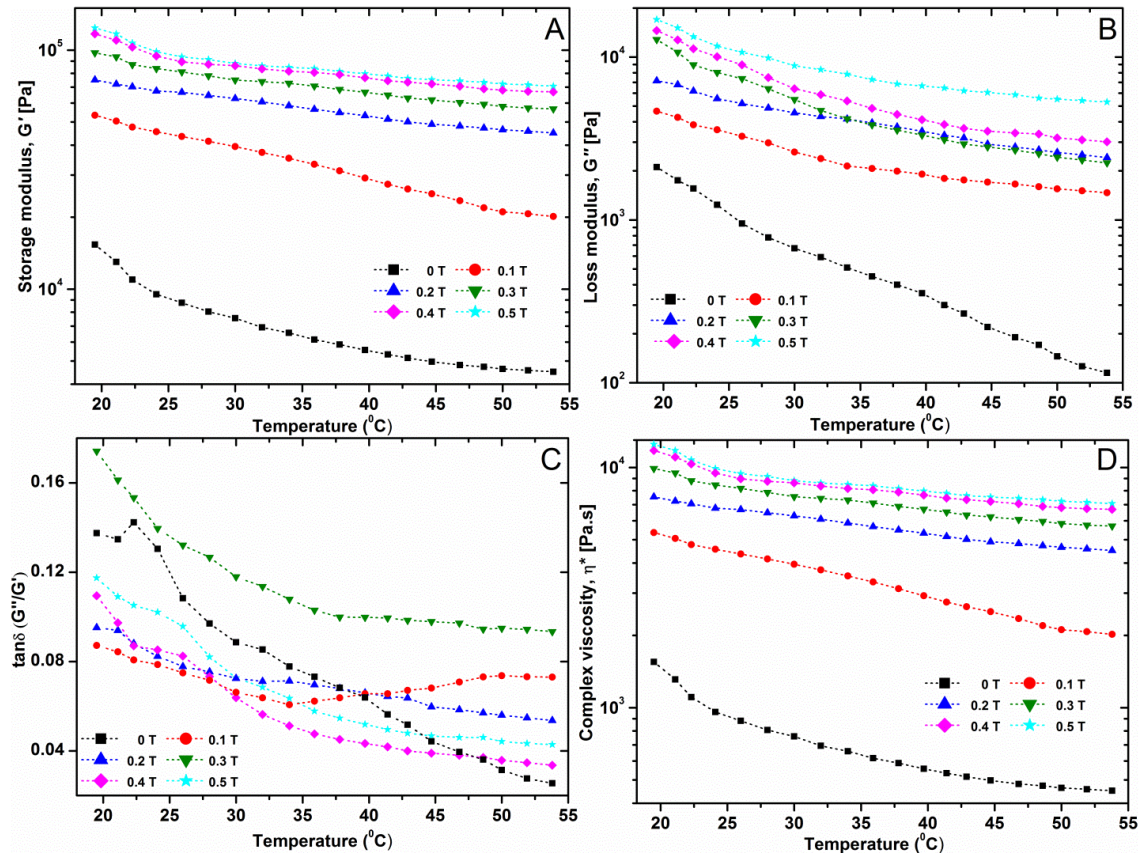


**Figure 7.6** Storage ( $G'$ ) and loss moduli ( $G''$ ) as a function of temperature and magnetic fields (A,B); loss factor versus temperature (C) and complex viscosity as a function of temperature (D) are shown.

However, the decrease in complex viscosity without magnetic field in the temperature range of 20°C-55°C is only 29% whereas a staggering 57% decrease in viscosity is reported for 0.5 T. It is obvious that the systems were more strongly affected by temperature when in external magnetic field.

## 7.4 Conclusion

In this chapter, we described the morphology and structure of Fe-rich PAA-Fe<sub>3</sub>Ni microspheres that were utilized for the fabrication of MR fluids. The enhanced surface properties of the PAA-Fe<sub>3</sub>Ni microparticles were attributed to the polymer functionalization and encapsulation in the extended growth stages. The morphological studies revealed an *fcc* structure with average microsphere size of 700 nm. Soft magnetic PAA-Fe<sub>3</sub>Ni particles were suitable for MR fluidic application. We performed steady shear magnetorheology of 10 vol% MR fluid under varied magnetic fields. Field induced relaxation and stress-shear rate curves followed expected trend, i.e. field-dependent

thickening behavior. The temperature-induced thinning effect was also observed in oscillatory rheology as complex moduli and viscosity both are strong functions of temperature.

# 8

## Chapter 8

### Investigations on $\text{Fe}_3\text{O}_4$ -based MR fluids

*The present chapter reports the synthesis of polyvinylchloride (PVC) encapsulated superparamagnetic magnetite micro-agglomerates. The agglomerates were characterized by SEM, TEM and XRD. Magnetorheological fluids were made by dispersing these particles in various concentrations in castor oil. The room temperature viscoelastic characterizations of these fluids were performed under different shear rates under different magnetic fields. In addition to micro-agglomerates, magnetorheological Payne effect was demonstrated in bidisperse MR fluids containing spherical monodisperse  $\text{Fe}_3\text{O}_4$  microspheres and Fe-microrod. We have also shown that stress softening was more pronounced for MR fluids with higher anisotropic contents, in contrast to isotropic MR fluid. The onset strains for LVR to non-linear region transition for anisotropic fluids were much lower than that of isotropic spherical nanoparticle-containing fluid. The stronger MR response for microrod-containing MR fluids can be explained in terms of enhanced field-induced structuration.*

## 8.1 Introduction

Iron-oxide based magnetic fluids are of importance for number of reasons. Firstly, it is the cheapest and most widely available magnetic material. That makes MRFs made with this the least expensive ones to produce. Despite having low saturation magnetization, Fe oxides display excellent tunability and surface properties in wet-chemical syntheses. That is why most of the commercial magnetic fluids use magnetite ( $\text{Fe}_3\text{O}_4$ ) as dispersed phase. Powders of  $\text{Fe}_3\text{O}_4$  can be prepared in many ways, wide ranges of micro and nanostructures in the form of spheres, rod, urchin-like, platelets etc. were reported [127]. Similar to isotropic spherical particles, these highly anisotropic nano and micro-structured materials can be used in many applications such as imaging and sensing. However, non-spherical particles e.g. rod-like microstructures and irregular micro-aggregates of wide size-distribution can form stronger field-induced structuration due to easy magnetization when the long axes are aligned parallel to magnetic field [128]. This gives rise to stronger MR response. Therefore, for a magnetorheological (MR) fluid to perform desirably, particle's surface morphology as well as shape anisotropy plays very crucial role. Another important aspect for Fe-oxide materials is their excellent affinity towards polymers and surfactants. By careful control of chemical reaction conditions, polymer encapsulation of  $\text{Fe}_3\text{O}_4$ -microstructures can give rise to excellent surface properties. The present work is aimed at characterizing polymer polyvinyl chloride (PVC)-encapsulated  $\text{Fe}_3\text{O}_4$  (magnetite) micro-agglomerates structurally and morphologically, followed by viscoelastic measurements of MR fluids. The synthesized particles had higher yield stress and chemical stability. We used PVC as encapsulating polymer because of its known water repelling action.

An interesting trend in stress-strain behavior of rubber materials is termed as Payne effect [129]. This is manifested as the change in storage and loss modulus with increasing strain amplitude under constant frequency. At some critical amplitude, storage modulus tends to decrease rapidly while loss modulus shows maxima in the same region where  $G'$  falls rapidly under deformation. Loss factor or  $\tan\delta$  ( $G''/G'$ ) also increases rapidly in this region till it gets independent of strain. The term the “magnetic Payne effect” was first coined by An et al. for MR gels to highlight their strain-softening [130]. Recently,

Sorokin et al. also reported magnetic Payne effect in carbonyl iron containing elastomer blends [131]. In this chapter, we have synthesized Bidisperse MRFs by substituting spherical magnetite particles with rod-like Fe-particles to show enhanced magnetorheological Payne effect in oscillatory rheology, in contrast to MRF containing only spherical magnetite particles. In addition to superior magnetic properties of Fe-microrods, shape anisotropy was also a key parameter that justifies the trends..

## 8.2 Structure and morphology of particles

### 8.2.1 SEM and TEM studies

Morphologies were observed using a scanning electron microscope and transmission electron microscope. Fig. 8.1 shows roughly spherical shape of the agglomerates, with an average diameter between 5 and 6  $\mu\text{m}$ . In the inset, transmission electron image of a

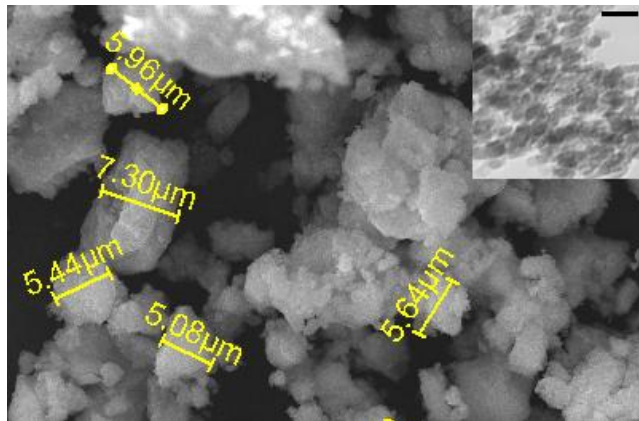


**Figure 8.1** SEM picture of the PVC-Fe<sub>3</sub>O<sub>4</sub> agglomerated composite. Inset shows TEM image of a single agglomerate (scale bar is 20 nm).

single agglomerated particle is shown. The size of this individual nanoparticle was found to be  $\sim 12$  nm.

Morphological characterizations of Fe-microrod and PAA-Fe<sub>3</sub>O<sub>4</sub> performed in ESEM were shown in Fig 8.2 (inset). PAA-Fe<sub>3</sub>O<sub>4</sub> microparticles were nearly spherical with high degree of surface roughness due to polymer-assisted growth in liquid polyol. While PAA-Fe<sub>3</sub>O<sub>4</sub> were mostly monodisperse, Fe-microrods showed high degree of polydispersity. Average diameter for PAA-Fe<sub>3</sub>O<sub>4</sub> was found to be  $\sim 300$  nm. Average length of Fe-rod was 800 nm with standard deviation of 100 nm. Cross-section of microrod was measured

as  $\sim 200$  nm. It can be noted that relative yield of nanorod was less than 50% with significant presence of spherical nanoparticles.

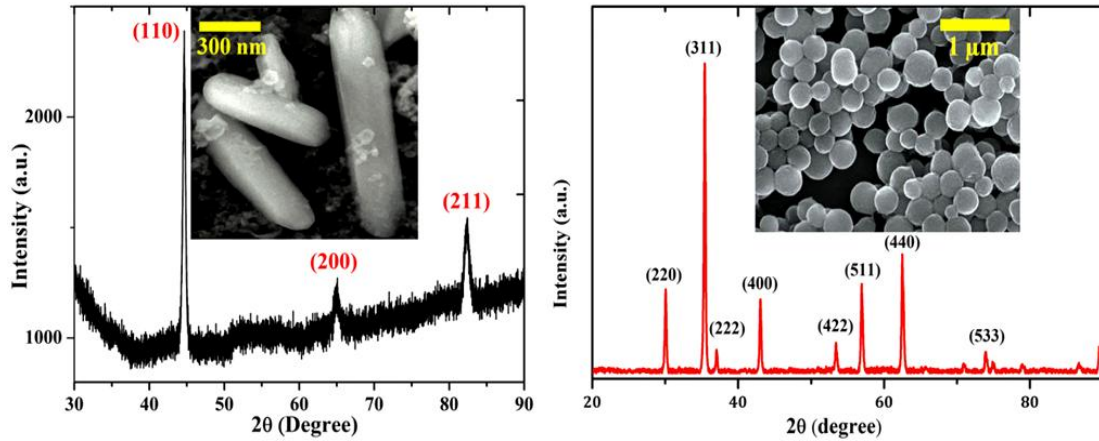


**Figure 8.2** X-ray diffraction patterns of Fe-nanorod (left) and PAA-Fe<sub>3</sub>O<sub>4</sub> nanospheres (right). ESEM images of as-prepared Fe-nanorod (left, inset) and PAA-Fe<sub>3</sub>O<sub>4</sub> nanospheres (right, inset) are also shown.

### 8.2.2 FTIR spectra

Fig. 8.3 shows the FTIR spectra of PVC and PVC-magnetite composite agglomerates. Pure magnetite usually exhibits a band in the region  $570\text{--}590$   $\text{cm}^{-1}$  characteristic to  $\text{Fe} - \text{O}$  stretching vibration associated with magnetite core [132].  $\text{Fe} - \text{O}$  stretching band of magnetite shifted slightly and appeared broad in PVC-magnetite composite, indicating the encapsulation of polymer on magnetite surface. The broad peak further indicated that  $\text{C} - \text{Cl}$  stretching frequency of PVC spotted at  $614$   $\text{cm}^{-1}$  was affected by Fe and Cl vicinity and masked by strong, broad  $\text{Fe} - \text{O}$  vibration of Fe<sub>3</sub>O<sub>4</sub> in the PVC-magnetite composite. The vibration at  $1390$   $\text{cm}^{-1}$  was associated carboxyl vibration of oleic acid. The bending vibration of  $\text{C} - \text{H}$  bond (of PVC) at  $1636$   $\text{cm}^{-1}$  was shifted to  $1624$   $\text{cm}^{-1}$  in polymer-composite due to encapsulation of PVC. PVC was characterized by  $\text{C} - \text{C}$  aliphatic stretching bond appearing at  $1070$   $\text{cm}^{-1}$ , which was slightly shifted to the left, indicating the formation of magnetite-PVC composite structure.

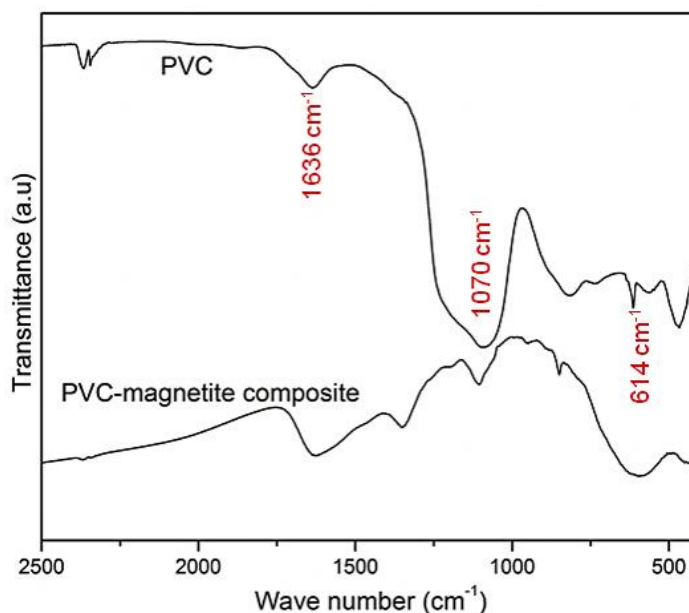


**Figure 8.3** FTIR spectra of PVC and PVC-encapsulated magnetite agglomerate.

### 8.2.3 X-ray diffraction

The crystalline structure of the obtained PVC-magnetite micro-agglomerates was characterized by X-ray diffraction. The X-ray diffraction patterns of the bulk magnetite and PVC-encapsulated magnetite nano-agglomerates were presented in Fig 8.4. All the characteristic peaks were associated to inverse spinel structure of magnetite. The calculated lattice parameter was found to be  $0.837 \text{ nm}$ , close to that of magnetite bulk value ( $0.839 \text{ nm}$ ). The crystal size calculated from the broadening of (311) peak using Scherrer formula and was found to be  $11.2 \text{ nm}$ , near to that found from TEM. X-ray diffraction patterns for PAA-Fe<sub>3</sub>O<sub>4</sub> and Fe-microrods were shown in Fig. 8.2.

For PAA-Fe<sub>3</sub>O<sub>4</sub> microspheres, all peaks are assigned to inverse spinel structure similar to Fe<sub>3</sub>O<sub>4</sub> with crystallite size of  $45 \text{ nm}$  (Fig. 8.2 right) The diffraction peaks at  $30.4^\circ$ ,  $35.88^\circ$ ,  $37.5^\circ$ ,  $43.3^\circ$ ,  $53.1^\circ$ ,  $57^\circ$ ,  $62.73^\circ$  and  $74.2^\circ$  were matched with standard magnetite XRD data (JCPDS No. 89-0691). Crystal structure of as-synthesized Fe-rods has also been confirmed by X-ray analysis. The peaks correspond to (110), (200) and (211) planes were characteristic to body centered cubic (bcc) structure of pure  $\alpha$ -Fe (JCPDS No. 05-0696).

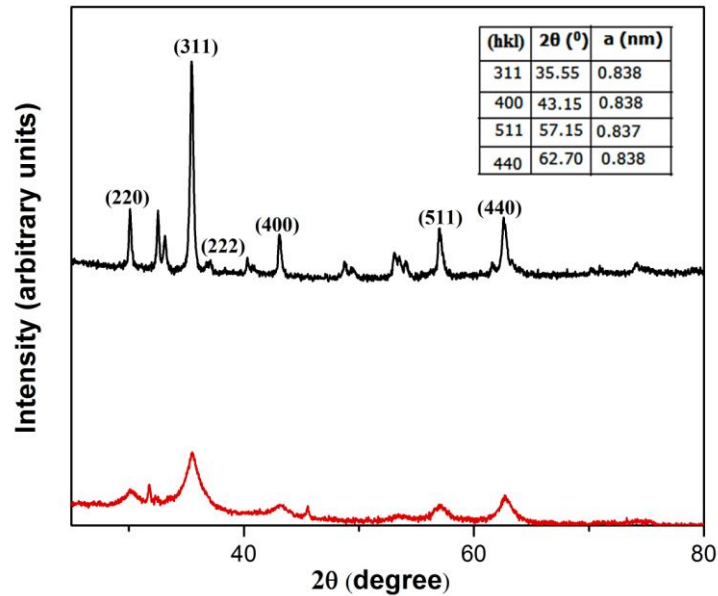


**Figure 8.4** X-Ray Diffraction patterns of the particles. The major peaks were identified. The red diffraction pattern is for PVC-composite agglomerates whereas, the top pattern represents the standard bare  $\text{Fe}_3\text{O}_4$  particles.

Crystallite size calculated using Scherrer formula was  $20.2 \text{ nm}$ . It has been shown previously that the preferential growth in  $\alpha$ -Fe microrod occurred through the (200) plane [133].

### 8.2.4 Magnetic characterization

Magnetic behavior of the microstructures in powder form was investigated at room temperature (Fig. 8.5). The saturation magnetization ( $M_s$ ) and coercivity ( $H_c$ ) for  $\text{Fe}_3\text{O}_4$  were measured to be  $61.7 \text{ emu/g}$  and  $51 \text{ Oe}$  whereas for  $\alpha$ -Fe,  $M_s$  and  $H_c$  were  $120.5 \text{ emu/g}$  and  $541 \text{ Oe}$  respectively were found.  $M_s$  of  $\text{Fe}_3\text{O}_4$  was smaller in magnitude than bulk value for magnetite, but was significantly higher than that reported earlier [134]. Reduction in saturation magnetization in nanoparticles compared to that of bulk value can originate due to number of factors, including association of polymer in composite structures, surface spin canting and presence of magnetic dead layers on surface [135]. Room temperature magnetization curve for Fe-microrod showed ferromagnetic behavior with high  $M_s$ , characteristic to  $\alpha$ -Fe. However, observed  $M_s$  was still much smaller than that of bulk saturation magnetization of pure Fe ( $218 \text{ emu/g}$  at 300K). One of the reasons was the association of surfactant CTAB in the growth of rod particles.

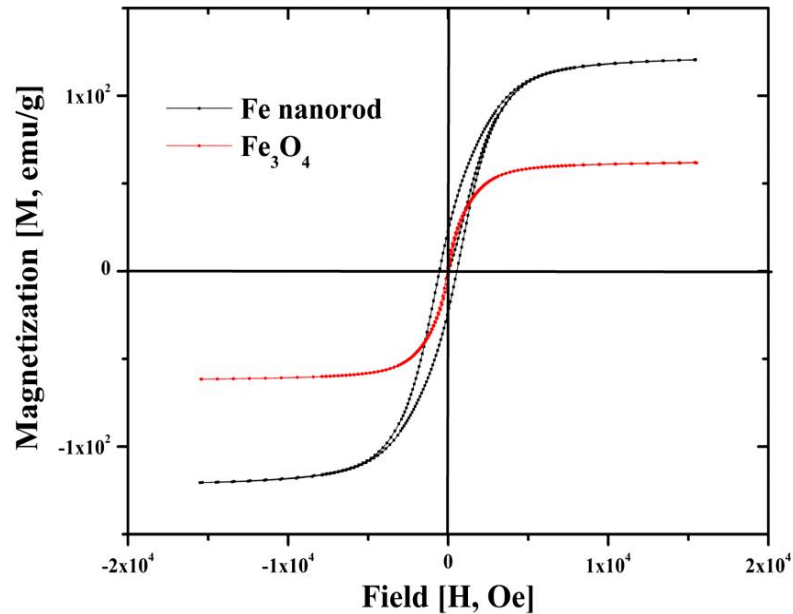


**Figure 8.5** Room temperature magnetization versus field hysteresis curves (M-H) were shown for Fe-microrod (black symbols) and  $\text{Fe}_3\text{O}_4$  microspheres (red symbols), respectively.

## 8.3 Magnetorheological studies

### 8.3.1 Magnetorheology in PVC- $\text{Fe}_3\text{O}_4$ based MR fluids

Fig. 8.6 (A) illustrates the dependence of MR fluid concentrations on the stress produced as a function of shear rates in the absence of magnetic field. It was seen that these shear curves displayed both finite yield stress and shear thinning. Therefore, it was suggested that they behaved as Herschel-Bulkley fluids. The equation is  $\tau = \tau_0 + k\dot{\gamma}^n$  where  $\tau$  = shear stress,  $\tau_0$  = yield stress, the minimum stress needed to start the flow,  $k$  = consistency (basically the viscosity coefficient),  $\dot{\gamma}$  = shear strain rate during the measurement, and  $n$  = the power law exponent, indicates if the flow is shear thinned ( $< 1$ ) or thickened ( $> 1$ ), and at  $n = 1$ , the behavior is Newtonian. Our data were fitted to this equation by least squares method. In Fig. 8.6 (A), the fits were drawn as lines and can be seen to be rather good in all cases. It was seen that increasing particulate concentration increased the plasticity of the flow, from Newtonian to the non-Newtonian behavior.

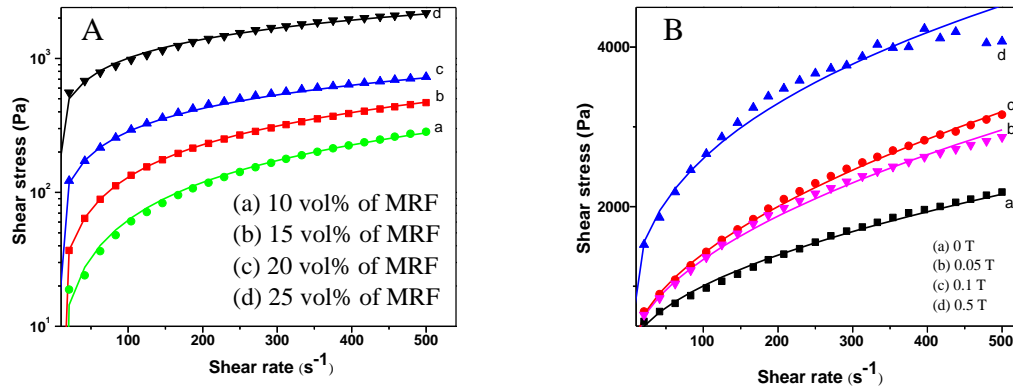


**Figure 8.6** (A) Rheological behavior of MR fluids for different concentrations under zero magnetic field. (B) Magnetorheological response of the 25 vol% MR fluid. In both cases, the lines are the fits to the model

Evidently the system acquired more viscosity and yield stress, and was more easily stress thickened as a result of higher concentration. The occurrence of nonlinear behavior even from the lower concentration must be due to the fact that these particles have non-zero remanence (acquired during magnetic extraction) resulting in bigger agglomeration and thus offer higher resistance to the flow. Table 8-1 shows the fitting parameters.

The consistency  $k$  is the parameter most closely related to apparent viscosity that obtained from Herschel-Bulkley equation. A relative viscosity parameter similar to  $\eta_r$  can also be defined for  $k$  as relative consistency,  $k_r = k/\eta_s$ , where  $\eta_s$  is viscosity of carrier fluid (castor oil).

**Table 8-1** flow behavior of various concentrates at zero field. Parameters derived from Herschel-Bulkley model.

Fitting parameters (HB model)	Concentration of MR fluids (vol %)			
	10	15	20	25
$\tau_0 (Pa)$	0.00	0.03	4.31	78.40
$n$	0.93	0.80	0.58	0.50
$k (Pa.s^n)$	0.86	3.27	19.38	92.68

Fig. 8.7 demonstrates that MR fluid consistency displays a systematic variation with particle volume fraction. The plot also shows the best fits of the Batchelor and Krieger-Dougherty models [33] with  $\phi_m$  and  $B$ ,  $B_l$  as fitting parameters. It was seen that with increasing volume fraction, quadratic relation was no longer valid. Therefore, the

Krieger-Dougherty relationship could more accurately fit the trend at higher volume fractions whereas Batchelor equation is a better fit at low concentration.

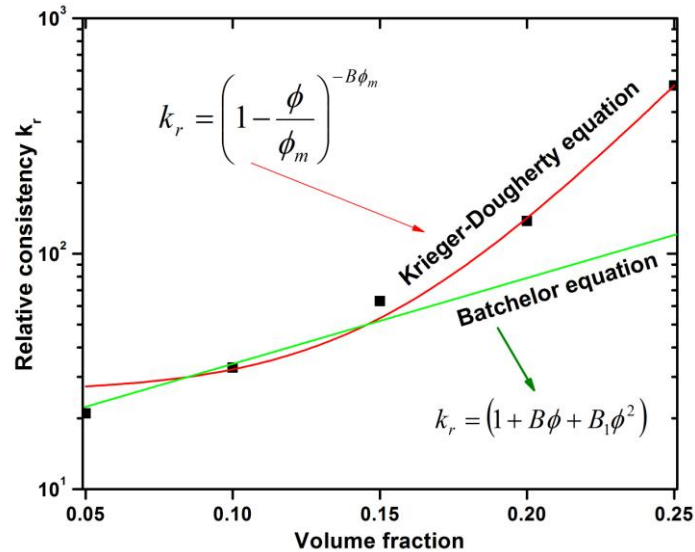


**Figure 8.7** Relative consistency,  $k_r$  plotted as a function of particle volume fraction ( $\phi$ ) for MR fluids in absence of magnetic field. The green and red fitting lines represent the Batchelor and Krieger-Dougherty relationships.

To study the behavior of the system under external magnetic fields, we chose the sample with highest concentration, this system was expected to show the maximum dependence of magnetic field. Fig. 8.6 (B) shows the behavior in this condition, and Table 8-2 displays the resultant fitting parameters. The fitted lines are drawn along with the data points that are shown as symbols. Under magnetic field, the behavior of the fluid was remarkable. While initially the yield stress was a bit reduced and the consistency was somewhat higher, the shear thinning was not unduly affected, but improved slightly. However, in the highest field while yield stress and consistency increased by about a factor of 4, the power index fell by about 30% from zero field value. We assume that this was because of enhanced chain like formation in this case. They were more rigidly held due to higher magnetic field, therefore, though the fall in viscosity was rapid, the value was still higher than any other at any given shear rate. It was also the most non-Newtonian in its behavior. However, it still retained appreciable amount of response under high fields.

**Table 8-2** Flow behavior of 25 vol% fluid at various magnetic fields. Parameters derived from HB model.

Fitting parameters (HB model)	Magnetic field (Tesla)			
	0	0.05	0.1	0.5
$\tau_0 (Pa)$	78.4	52.3	56.6	212.0
$n$	0.50	0.51	0.52	0.36
$K (Pa.s^n)$	92.7	124.6	123.7	445.8

### 8.3.2 Magnetorheological Payne effect in Fe-microrod containing MR fluids

The MR fluids were made by dispersing proper amounts of  $Fe_3O_4$  and Fe powder into castor oil (viscosity  $0.879 Pa.s$  at  $25^\circ C$ ) through mechanical stirring and ultrasonication. In order to study the effect of anisotropic Fe-rod in magnetorheology, we prepared three MR suspensions (MRF1, MRF2 and MRF3) with gradual substitution of  $Fe_3O_4$  spheres with Fe-rod such that the total dispersed phase concentrations maintained at 10 vol% for all suspensions. The amounts of spherical  $Fe_3O_4$  were 10 vol%, 8 vol% and 5 vol% for MRF1, MRF2 and MRF3 respectively. Fig. 8.8 displays the dependence of the storage ( $G'$ ) and loss moduli ( $G''$ ) for MRFs as a function of deformation amplitude at a fixed frequency ( $10 Hz$ ) and magnetic field strength of  $0.33T$ . The loss factor ( $\tan\delta$ ) is also plotted in Fig. 8.8 inset. The MR samples were pre-treated with homogeneous magnetic field for 3 minutes. This was to allow the samples to form equilibrium field-induced microstructures before the strain sweep would take place. In presence of magnetic field, MRFs behaved usually with steady decline in storage modulus as a function of strain amplitude. Characteristic to field-induced  $G'$  for aggregated microstructures, short LVR ( $\sim 0.002$  strain %) was reported for all the suspensions. The trend in initial value of  $G'$  followed the order:  $MRF1 < MRF2 < MRF3$ . This was expected as with higher substitution of Fe-nanorod, magnetic and shape anisotropy ensured stronger structuration. The magnitude of magnetorheological Payne effect ( $G'_0 - G'_\infty$ ) also increased with the increasing Fe-microrod content. At low Fe loading, the observed variation in the amplitude of the Payne effect was weak. But as the vol% of Fe increased, significant and pronounced variation was observed. This was principally due to the breakdown of aggregated networks at higher strains [130, 131]. With increasing strain, unperturbed

chains of magnetic particles started to crumble. The strength of interparticle network is a function of deformation as the dipole-dipole interaction energy between particles decreased with increasing strain. Upon increasing the strain further, steady decline in  $G'$  was reported for all MRFs. This can be explained in terms of magnetorheological Payne effect, where distance between particles in the aggregates was increased with applied strain, implying a drop in magnetic dipole-dipole interaction energy [130]. In presence of field, beyond the critical strain corresponds to LVR, the distribution of interparticle distance was no more uniform, this is to say that response of magnetized clusters would be completely different than what it was in LVR. The destruction of clusters and their reformation and redistribution in presence of field at higher deformation gave rise to nonlinear decrease in storage modulus.

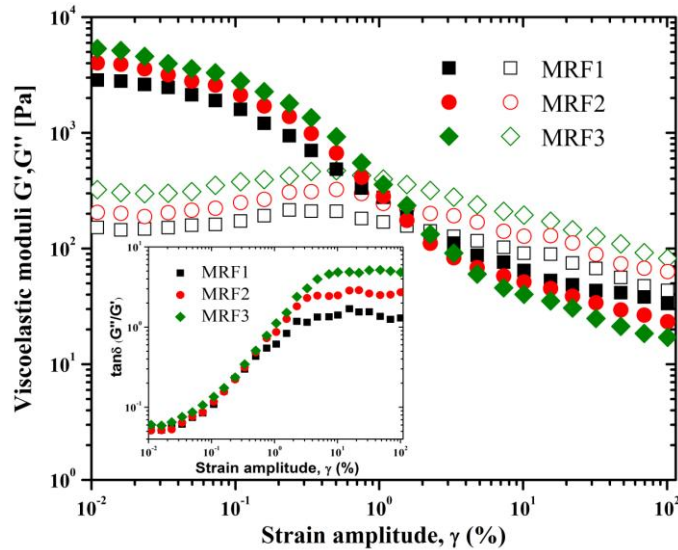


**Figure 8.8** Amplitude sweep oscillatory rheology for MRF1 (black symbols), MRF2 (red symbols) and MRF3 (green symbols) under constant frequency of 10 Hz and constant magnetic field 0.33T. Storage ( $G'$ ) and loss moduli ( $G''$ ) represented by closed and open symbols, respectively. Inset, loss factor ( $G''/G'$ ) was plotted against strain amplitude.

The trend in loss moduli (Fig. 8.8) illustrated three distinct regions: at very low strain (up to 0.03%), both  $G'$  and  $G''$  were practically independent; afterwards  $G''$  increased with increasing strain and  $G'$  fell, to form a maximum at  $\gamma \sim 1\%$ . Following a cross-over point with  $G'$ , long decreasing tails were observed. The initial linear region basically coincided with LVR, following changes in magnitude of  $G'$  and  $G''$  till these reached a point of inflexion and maximum respectively. Increase in the loss modulus can be explained in

terms of dissipation of energy for continuous rupture of the magnetic coupling between magnetized particles with increasing  $\gamma$ . The subsequent moduli decrease occurred when the microstructure already started collapsing at higher  $\gamma$  and the interparticle interactions decreased due to growing distances between particles. Beyond the cross-over strain ( $\gamma_{cr}$ ), flow was almost laminar and therefore, no significant change in  $G'$  and  $G''$  were observed. The loss factor ( $\tan\delta$ ) curves for the MRFs showed the same behavior.

All these changes in the elastic moduli can be thought of as occurring due to the dynamic breakdown and reformation of aggregated network comprised of nanospheres and nanorods with increasing deformation gave rise to magnetorheological Payne effect, similar to that of original carbon-filler containing rubber matrix [129]. Similarly the interplay between magnetostatic interaction of aggregated networks and hydrodynamic forces arising from mechanical strain gave rise to magnetorheological Payne effect. A few mathematical models were derived subsequently in order to explain the Payne effect, of which the one proposed by Kraus comes first [136]. Kraus constructed a phenomenological model which has often been applied for the fitting of experimental data. The model is based on the assumption that the filler aggregates break and recombine under different rates, which depend on amplitude of deformation and on rate constants. In this model, however, the interaction between filler network and matrix fluid was ignored. Since there is little or no chemical interaction between magnetic particles and carrier fluid in a typical MRF, the magnetostatic interaction clearly dominated over all other interactions. The result showed that the excess storage modulus  $\left(\frac{G' - G'_\infty}{G'_0 - G'_\infty}\right)$  with increasing deformation amplitude had the following characteristic form:

$$\frac{G' - G'_\infty}{G'_0 - G'_\infty} = \frac{1}{1 + \left(\frac{\gamma}{k}\right)^{2m}} \quad (8.1)$$

Where,  $k$  and  $m$  are fitting parameters; since Kraus model equation was based on some arbitrary assumptions, the fitting parameters did not possess any direct obvious physical significance [141]. The quantification of Payne effect was based on agglomeration and de-agglomeration of particle networks, the parameter  $k$  represents a rate constant of structural aggregation and subsequent rupture. It is expressed as,  $k = \left(\frac{k_a}{k_b}\right)^{\frac{1}{2m}}$  (8.2)

where,  $k_a$  and  $k_b$  are rate constants for agglomeration and de-agglomeration, respectively. The parameter  $m$  is considered to be universal for carbon filler-rubber composite materials. Both the parameters are empirical and can't be evaluated from direct measurements. The fitting of  $G'$  versus  $\gamma$  plots with Kraus model is shown in Fig. 8.9. The fitting parameters are listed in Table 8-3. One can see that the fittings were remarkably good. It can be seen that the values of  $k$  and  $m$  are correlated and quite strongly depend on the shape anisotropy of the suspensions. So we find that in contrast to only matrix-filler interaction, magnetorheological fluids demonstrated both short and long range magnetostatic interaction. Even when the strain was sufficiently high, there was long-range interaction between particles. This was probably the reason that our reported values of  $m$  were significantly higher than that reported by previous authors. Therefore, there is nothing universal in the value of  $m$ , rather it can actually be used to find the anisotropy of the agglomerates.

**Table 8-3** fitting parameters of Kraus fit for  $G'$  versus strain% ( $\gamma$ ) for MRFs

Fitting parameters (Krauss model)	MR samples		
	MRF1	MRF2	MRF3
<b>k</b>	0.181	0.212	0.232
<b>m</b>	0.75	0.76	0.77

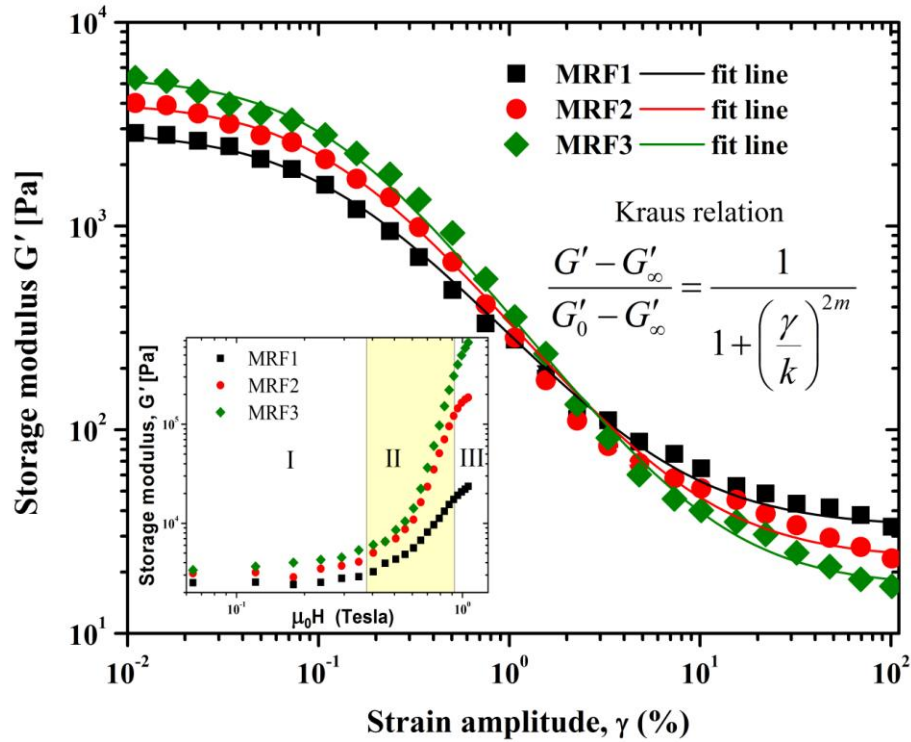


**Figure 8.9** Storage modulus ( $G'$ ) is plotted as a function of strain in amplitude sweep oscillatory measurement under constant frequency of 10 Hz and constant magnetic field 0.33T. Fit lines represent Kraus equation relating the change in  $G'$  with strain ( $\gamma$ );  $k$  and  $m$  are fitting parameters. Inset, magnetic field sweep of storage modulus ( $G'$ ) at constant strain amplitude of 0.02%.

Magnetsweep studies under oscillation were performed at very low constant strain amplitude of 0.02%. Unlike rotational rheometry, oscillatory tests at sufficiently low deformation did not cause irreversible rupture of aggregates. As observed in amplitude sweep test, MRFs possessed very narrow LVR. For magnetsweep study, a constant angular frequency of 10 Hz was applied while increasing magnetic field continuously. The plots of  $G'$  of MRFs as a function of field are shown in Fig. 8.9 inset. As expected, MRF3 with highest nanorod concentration exhibited highest percent increase in  $G'$  when field swept from 0 to 1 T, followed by MRF2 and MRF1. The overall behavior was generalized in terms of three distinct regions: (I) in the first zone, increment in  $G'$  value was very small with increasing field. At low field, conglomerates of magnetic structures were more evenly distributed, giving rise to less steeper response. In region (II) of intermediate field range, a linear increase was found owing to the formation of more robust aggregates. Beyond the intermediate field range, region (III) showed a flattening

tendency, it was where the sample became almost resistant to flow. This happened because particles and aggregates were fully aligned along the field lines.

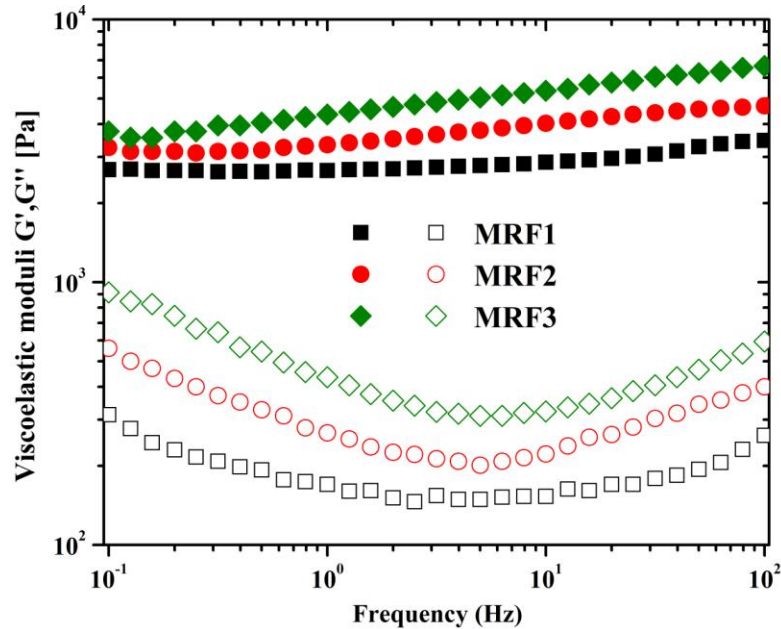


**Figure 8.10** Frequency sweep oscillatory rheological curves were shown for MRF1 (black squares), MRF2 (red circles) and MRF3 (green diamonds) under constant strain amplitude ( $\gamma$ ) of 0.02% and constant magnetic field of 0.33T. Storage ( $G'$ ) and loss modulus ( $G''$ ) represented by closed and open symbols, respectively.

Frequency-dependent oscillatory measurements were recorded under very low constant amplitude of deformation (0.02%) and the frequency was varied in the range of 0.1 – 100 Hz. Frequency-dependence of storage and loss modulus measured in presence of magnetic field (0.33 T) is shown in Fig. 8.10. Under small angle oscillatory strain (SAOS), MRFs showed no significant critical behavior. As expected,  $G'$  of the anisotropic MRFs displayed stronger frequency dependence owing to stronger aggregate formation under small strain. The slope of  $G'$  versus frequency curves showed regular increase for the samples in this order: MRF3>MRF2>MRF1. For SAOS, no significant change in rheology was expected except the redistribution of microstructural aggregates under increasing frequency. In anisotropic samples (MRF2 and MRF3), some pre-ordering of the particle aggregates in absence of magnetic field resulted in strengthening of the field induced chain-structures, therefore, giving rise to an increase in the mechanical modulus ( $G'$ ). However, behavior of loss modulus was difficult to explain. Finally, the origin of trough in  $G''$  curves in the frequency region 2 – 10 Hz was unclear.

The viscous dissipation of energy was associated to hydrodynamic effect which was attributed to internal movement of aggregates with increasing frequency [137]. But it was not yet clear which mechanism influenced the magnitude and frequency-dependent trend of  $G''$ .

## **8.4 Conclusion**

In this chapter, we discussed the morphological characterization of PVC-magnetite agglomerates and the magnetorheological response both in off-state and on-state steady shear modes. The higher structural anisotropy of agglomerates resulted in enhanced MR effect. The structure-rheology correlation was also studied in bidisperse MR fluids containing magnetite microspheres and Fe-microrods. We performed magnetorheological properties of three MR fluids (10 vol %) containing isotropic  $\text{Fe}_3\text{O}_4$  and anisotropic Fe-microrods under both small and large amplitude oscillatory deformations. We have shown that stress softening became more pronounced as the anisotropic contents increased. The threshold strains for LVR to non-linear region transition for MRF2 and MRF3 were smaller in magnitude than that of isotropic spherical nanoparticle-containing fluid (MRF1). This was interpreted in terms of stronger microstructure formation in anisotropic fluids and formed a demonstration of magnetorheological Payne effect.

# 9

## **Chapter 9**

### **Summary and conclusions**

*In this chapter we summarized all the findings in the previous chapters and concluded. We also discussed some of the areas where further research work could also be performed.*

## 9.1 Summary

Magnetorheological (MR) fluids are a special class of smart materials in which external magnetic field directly couples with the change in mechanical properties, i.e. field-induced viscosity and shear stress. The wide range of applications of MR fluid brings about a number of operational requirements including the fast response and large amplitude change in magneto-mechanical and thermo-magnetorheological stress. The research described in this thesis was based on two important considerations: (a) the design and functionalization of sub-microstructures of novel binary magnetic systems, and (b) investigation of magnetically and thermally induced changes in rheological properties of the fluid systems based on these materials. An MR fluid is characterized by high mechanical stress, durability, temperature stability and dispersibility against settling. It was shown how the particle volume fraction, shape and interactions between particles, spatial arrangement of particles and nature of bulk fluid flow affected the performance of an MR fluid. Particle anisotropy offers stronger MR effect compared to that of spherical counterparts as non-spherical particles are orientable and inter-particle interaction among the anisotropic particles are higher than that of spherical particles, owing to stronger field-induced structuration. We have demonstrated that particle volume fraction and magnetic saturation significantly influenced the magnetorheological properties of MRFs. The thesis also addressed the role of shape anisotropy of dispersed magnetic phase containing FeCo, FeNi, NiCo and Fe-oxides in MR suspensions. We also investigated the mechanism that governs non-equilibrium size distribution of internal chain structures with increasing temperature.

We prepared the micro and nanostructures of binary magnetic systems using the bottom-up approaches, i.e. applying wet-chemical reduction routes. Various reducing agents were employed in the fabrication such as polyol, hydrazine, borohydride etc. as mentioned in chapter 3.

In chapter 4, we described the structure and morphology of micron-sized  $\text{Fe}_{55}\text{Co}_{45}$  particles with variable shape and surface morphology. The cubic and spherical FeCo-alloy systems were synthesized for the first time by modified aqueous borohydride reduction of metal salts in the presence of electrostatic stabilizers (sodium citrate and

sodium acetate) and polymer (PEG 6000). Two systems of MR fluids were prepared using these particles and effects of sizes and shapes of alloyed particles on magnetorheology were investigated. It was found that MR fluid containing acetate-polymer capped FeCo produced lower yield stress under magnetic field, whereas citrate-capped FeCo-based MR fluid displayed much higher magnetorheological response owing to its higher magnetic permeability and cubic and rigid morphology. These materials are thus found to have good rheological properties and suitable for some practical use.

In chapter 5, we investigated the structure and morphology of NiCo nanoflowers and nanoplatelets. The bidisperse MR fluids containing NiCo nanoflowers in ferrofluidic suspensions displayed stronger MR effect in steady shear rheology, as compared to monodispersed one. The stronger microstructure formation in bidisperse fluids further reflected in higher off-state viscosity, compared to that of other fluid. For the MR suspensions containing nanoplatelets, strain-dependent hardening of  $G'$  was explained in terms of short range interaction and reduction of effective interparticle distance when fluid volume% was increased.

In chapter 6, we studied the structure, morphology and magnetorheology of Co-rich NiCo alloyed microclusters. The behaviors of static and dynamic yield stresses for these MR fluids were found to depend on average particle magnetization, with the static yield stress dependence on  $M$  being stronger of the two. Magnetosweep studies demonstrated an interesting relaxation phenomenon that was interpreted as an effect of local temperature rise within the fluid at high field and at constant shear rate. The temperature-dependent MR characterization has shown a decline in MR properties at elevated temperatures for both samples of Co-rich NiCo microclusters. Considering the thermal sensitivity of yield stress, magnetic saturation of powder  $\text{Co}_{0.9}\text{Ni}_{0.1}$  and matrix fluid viscosity at elevated temperature, it was shown that change in carrier fluid viscosity with temperature significantly affects the overall fluid performance. We have also shown that time-temperature-field superposition method is applicable for the two MR suspensions with different  $\text{Co}_{0.9}\text{Ni}_{0.1}$  volume fractions. The master curves generated for both the fluids with respect to a reference temperature, reference magnetization and reference yield stress,

indicated a good correlation between the individual sensitivity parameters that were affected differently with increasing temperature.

In chapter 7, we described the morphology and structure of Fe-rich PAA-Fe<sub>3</sub>Ni microspheres that were utilized for the fabrication of MR fluids. The enhanced surface properties of the PAA-Fe<sub>3</sub>Ni microparticles were attributed to the polymer functionalization and encapsulation in the extended growth stages. The morphological studies revealed an *fcc* structure with average microsphere size of 700 nm. Soft magnetic PAA-Fe<sub>3</sub>Ni particles were suitable for MR fluidic application. We performed steady shear magnetorheology of 10 vol% MR fluid under varied magnetic fields. Field induced relaxation and stress-shear rate curves followed expected trend, i.e. field-dependent thickening behavior. The temperature-induced thinning effect was also observed in oscillatory rheology as complex moduli and viscosity both are strong functions of temperature.

In chapter 8 we discussed the morphological characterization of PVC-magnetite agglomerates and the magnetorheological response both in off-state and on-state steady shear modes. The higher structural anisotropy of agglomerates resulted in enhanced MR effect. The structure-rheology correlation was also studied in bidisperse MR fluids containing magnetite microspheres and Fe-microrod. We performed magnetorheological studies of three MR fluids (10 vol %) containing isotropic Fe<sub>3</sub>O<sub>4</sub> and anisotropic Fe-microrods under both small (SAOS) and large angle oscillatory strain (LAOS). The MR fluids demonstrated rapid stress relaxation under increasing deformation and uniform magnetic field beyond linear viscoelastic region (LVR), which has not been studied in conventional MR fluids. We have also shown that stress softening was more pronounced for MR fluids with higher anisotropic contents (MRF2 and MRF3), in contrast to isotropic MR fluid. The threshold strains for LVR to non-linear region transition for MRF2 and MRF3 were smaller in magnitude than that of isotropic spherical nanoparticle-containing fluid (MRF1). The fixed strain magnetosweep experiment in oscillatory flow displayed three distinct regions in field-dependent curves. This is characteristic to magnetorheological fluids and was interpreted in terms of field-induced structural inhomogeneity within the fluid.

## 9.2 Future works

The results and discussion in the thesis lay the groundwork for a good understanding of the behavior of the MR fluids under steady shear and oscillatory rheology. The focus of the study involves the systematic and interdisciplinary approach to fabricate and analyze the flow aspects of MR fluids. Advanced modeling of the experimental fluid data is very important. The existing models are largely phenomenological and material-specific. The goal is to be able to predict MR properties of fluid compositions without needing to use expensive experimental evaluations. Secondly, a combined device-fluid optimization is also an important extension of the present study. A unified model can work both in fluid systems and in devices. This would make a combined optimization possible that includes geometric parameters, particle volume fractions, compositions etc. However, the next step towards the utilization of MR fluids in various application fields is crucial in terms of operability. Although we developed novel MR fluid systems and thoroughly investigated the rheology, design and operational suitability of the devices utilizing these MRFs was not verified. Future studies should involve specific design aspects for dampers and clutches in terms of durability and reliable performance in extreme conditions. Furthermore, temperature-induced changes in MR effect were not performed for FeCo and Fe-oxide systems. Therefore, detailed thermo-magnetorheological characterization for the specified systems will also be performed in future.

## Bibliography

- [1] J. Rabinow, *AIEE Trans.* **67** (1308) 1948.
- [2] J. Rabinow, Magnetic Fluid Torque and Force Transmitting Device, U.S. Patent. 1951. (USA).
- [3] S. Odenbach (Ed.) *Ferrofluids: Magnetically Controllable Fluids and Their Applications*, Springer 2002.
- [4] Y. F. Duan, W. Q. Ni, J. M. Ko, *J. Intell. Mat. Syst. Struct.* **17** (321) 2006.
- [5] P. Grad, *Engineering and Technology* **1** (34) 2006.
- [6] W. Kordonsky, A. Shorey, *J. Intell. Mat. Syst. Struct.* **18** (1127) 2007.
- [7] G. M. Kamath, N. M. Wereley, M. R. Jolly, *J. Am. Helicopter Soc.* **44** (234) 1999.
- [8] W. Kordonski, D. Golini, *J. Intell. Mater. Syst. Struct.*, **13** (401) 2002.
- [9] M. E. Cobern, C. A. Perry, J. A. Barbely, D. E. Burgess, M. E. Wassell, *SPE/IADC Drilling Conference*, **1** (339) 2007.
- [10] Y. M. Shkel, D. J. Klingenberg, *J. Rheol.* **45** (351) 2001.
- [11] G. Bossis, E. Lemaire, O. Volkova, H. Clercx, *J. Rheol.* **41** (687) 1997.
- [12] R. Tao, *J. Phys. Condens. Mat.* **13** (R979) 2001.
- [13] B. J. de Gans, *Magnetorheology of an Inverse Ferrofluid*, University of Twente (135) 2000.
- [14] W. H. Li, G. Chen, S. H. Yeo, *Smart Mater. Struct.* **8** (1999) 460.
- [15] I. Jonkkari, E. Kostamo, J. Kostamo, S. Syrjala, M. Pietola, *Smart Mater. Struct.* **21** (2012) 075030.
- [16] O. Volkova, G. Bossis, M. Guyot, V. Bashtovoi and A. Reks, *J. Rheol.* **44** (91) 2000.
- [17] R. E. Rosensweig, *Ferrohydrodynamics*, Dover, New York, 1997.
- [18] S. Chikazumi, *The Physics of Magnetism*, Wiley, New York, 1964.
- [19] C. Chen, *Magnetism and Metallurgy of Soft Magnetic Materials*. Dover, New York (2<sup>nd</sup> ed.) 1986.
- [20] K. H. J. Buschow, F. R. de Boer, *Physics of Magnetism and Magnetic Materials*, Kluwer Academic Publishers, New York (112) 2004.
- [21] P. P. Phulé, *Smart Materials Bulletin* **2001-2** (7) 2001.
- [22] R. M. Bozorth, *Ferromagnetism*, IEEE Press, New York, 1978.
- [23] R. C. Bell, J. O. Karli, A. N. Vavreck, D. T. Zimmerman, G. T. Ngatu, N. M. Wereley, *Smart Mater. Struct.* **17** (015028) 2008.

- [24] J. L. Viota, J. D. G. Duran, F. Gonzalez-Caballero, A.V. Delgado, *J. Magn. Magn. Mater.* **314** (80) 2007.
- [25] S. Mueller, E. W. Llewellyn, H. M. Mader, *Proc. R. Soc. A* **466** (1201) 2010.
- [26] W. H. Li, G. Chen, S. H. Yeo, H. Du, *Int. J. Mod. Phys. B* **16** (2725) 2002.
- [27] H. A. Barnes, *J. Non-Newtonian Fluid Mech.* **70** (1-33) 1997.
- [28] N. J. Wagner, J. F. Brady, *Phys. Today* **62** (27) 2009.
- [29] H. Markovitz, *Polymer Rheology*, Carnegie Mellon University, Pittsburgh, 1980.
- [30] R. Rutgers, *Rheol. Acta* **2** (202) 1962.
- [31] A. Einstein, *Ann. Phys.* **34** (591) 1911.
- [32] H. Brenner, *Annu. Rev. Fluid Mech.* **2** (137) 1970.
- [33] G. K. Batchelor, *J. Non-Newton. Fluid* **83** (97) 1977.
- [34] T. Kitano, T. Kataoka, T. Shirota, *Rheol. Acta* **20** (207) 1981.
- [35] I. M. Krieger, T. J. Dougherty, *T. Soc. Rheol.* **3** (137) 1959.
- [36] S. H. Maron, P. E. Pierce, *J. Colloid Sci.* **11** (80) 1956.
- [37] J. J. Stickel R. L. Powell, *Annu. Rev. Fluid Mech.* **37** (129) 2005.
- [38] J. S. Chong, E. B. Christiansen, A. D. Baer, *J. Appl. Polym. Sci.* **15** (2007) 1971.
- [39] G. B. Jeffery, *Proc. R. Soc. Lond. A* **102** (161) 1922.
- [40] J. D. Ferry, *Viscoelastic Properties of Polymers*, John Wiley & Sons, Inc., 1961.
- [41] E. C. Bingham, *Fluidity and plasticity*, McGraw-Hill, New York, 1922.
- [42] W. H. Herschel, R. Bulkley, 1926 *Kolloid Z.* **39** (291) 1926.
- [43] N. Casson, *Rheology of disperse systems (Ed. C. C. Mill)*, Pergamon Press, Oxford, 1959.
- [44] M. M. Cross, *J. Colloid Sci.* **20** (417) 1965.
- [45] K. Yasuda, R. C. Armstrong, R. E. Cohen, *Rheol. Acta* **20** (163) 1981.
- [46] E. Lemaire, G. Bossis, Y. Grasselli, *J. Magn. Magn. Mater.* **122** (51) 1993.
- [47] G. Bossis, E. Lemaire, *J. Rheol.* **35** (1345) 1991.
- [48] R. E. Rosensweig, *J. Rheol.* **39** (179) 1995.
- [49] J. M. Ginder, L.C. Davis, *Appl. Phys. Lett.* 1994. **65** (3410) 1994.
- [50] D. J. Klingenberg, J. C. Ulicny, M. A. Golden, *J. Rheol.* **51** (883) 2007.
- [51] P. J. Rankin, A. T. Horvarth, D.J. Klingenberg, *Rheol. Acta* **38** (471) 1999.
- [52] V. K. LaMer, R. H. Dinegar, *J. Am. Chem. Soc.* **72** (4847) 1950.
- [53] Aslam Khan et al., *Polym. Int.* **59** (1690) 2010.

- [54] <http://www.ammr.org.au/myscope/sem/practice/principles/layout.php>
- [55] [http://en.wikipedia.org/wiki/Transmission\\_electron\\_microscopy](http://en.wikipedia.org/wiki/Transmission_electron_microscopy)
- [56] [http://en.wikipedia.org/wiki/Vibrating\\_sample\\_magnetometer](http://en.wikipedia.org/wiki/Vibrating_sample_magnetometer).
- [57] B. D. Cullity, C. D. Graham, *Introduction to Magnetic Materials*, Wiley, 2009.
- [58] S. Genç, *Synthesis and properties of magnetorheological (MR) fluids*, University of Pittsburg, 2002 (PhD dissertation).
- [59] A. J. Margida, K. D. Weiss, J. D. Carlson, *Int. J. Mod. Phys. B* **10** (3335) 1996.
- [60] M. Sedlacik, V. Pavlinek, R. Vyroubal, P. Peer, P. Filip, *Smart Mater. Struct.* **22** (035011) 2013.
- [61] S. W. Ko, M. K. Hong, H. J. Choi, B. H. Ryu, *IEEE Trans. Magn.* **45** (2503) 2009.
- [62] X. B. Su, H. G. Zheng, Z. P. Yang, Y. C. Zhu, A. L. Pan, *J. Mater. Sci.* **38** (4581) 2003.
- [63] X.W. Wei, G. X. Zhu, Y. J. Liu, Y.H. Ni, Y. Song, Z. Xu, *Chem. Mater.* **20** (6248) 2008.
- [64] M. Ethayaraja, R. Bandyopadhyaya, *J. Am. Chem. Soc.* **128** (17102) 2006.
- [65] A. Shokuhfar, S. S. S. Afghahi, *Advances in Materials Science and Engineering* **2014** (295390) 2013.
- [66] Y. Xia, Y. Xiong, B. Lim, S.E. Skrabalak, *Angew. Chem. Int. Ed.* **48** (60) 2009.
- [67] I. B. Jang, H. B. Kim, J. Y. Lee, J. L. You, H. J. Choi, M. S. Jhon, *J. Appl. Phys.* **97** (10Q912) 2005.
- [68] R. W. Chantrell, J. Popplewell, S. W. Charles, *IEEE Trans. Magn.* **Mag-14** (975) 1978.
- [69] G. S. Chaubey, C. Barcena, N. Poudyal, C. Rong, J. Gao, S. Sun, J. P. Liu, *J. Am. Chem. Soc.* **129** (7214) 2007.
- [70] F. F. Fang, H. J. Choi, Y. Seo, *ACS Appl. Mater. & Interfaces.* **2** (54) 2010.
- [71] I. Arief, P. K. Mukhopadhyay, *Magnetohydrodynamics* **49** (479) 2013.
- [72] S. Genç, P. P. Phulé, *Smart Mater. Struct.* **11** (140) 2002.
- [73] G. V. Kurlyandskaya, S. M. Bhagat, C. Luna, M. Vazquez, *J. Appl. Phys.* **99** (104308) 2006.
- [74] M. J. Hu, Y. Lu, S. Zhang, S.R. Guo, B. Lin, M. Zhang, S. H. Yu, *J. Am. Chem. Soc.* **130** (11606) 2008.
- [75] L. Zhang, J. A. Bain, J. Zhu, L. Abelman, T. Onoue, *J. Appl. Phys.* **100** (053901) 2006.
- [76] A. Gomez-Ramirez, M. T. Lopez-Lopez, J. D. G. Duran, F. Gonzalez-Caballero, *Soft Matter* **5** (3888) 2009.
- [77] S. I. Cha, C. B. Mo, K. T. Kim, S. H. Hong, *J. Mater. Res.* **20** (2148) 2005.

- [78] H. Yang, T. Ogawa, D. Hasegawa, M. Takahashi, *J. Appl. Phys.* **103** (07D526) 2008.
- [79] H. Colfen, S. Mann, *Angew. Chem. Int. Ed.* **42** (2350) 2003.
- [80] K. Yao, X. Yin, T. Wang, H. Zeng, *J. Am. Chem. Soc.* **132** (6131) 2010.
- [81] R. Qiao, X. L. Zhang, R. Qiu, J. C. Kim, Y. S. Kang, *Chem. Eur. J* **15** (1886) 2009.
- [82] M. Y. Rafique, L. Pan, W. S. Khan, M. Z. Iqbal, H. Qiu, M. H. Farooq, M. Ellahid, Z. Guo, *Cryst. Eng. Comm.* **15** (5314) 2014.
- [83] S. B. Darling, S. D. Bader, *J. Mater. Chem.* **15** (4189) 2005.
- [84] G. Viau, F. Fiévet-Vincent, F. Fiévet, *Solid State Ionics* **84** (259) 1996.
- [85] P. Toneguzzo, G. Viau, O. Acher, F. Guilet, E. Bruneton, F. Fievet-Vincent, F. Fievet, *J. Mater. Sci.* **35** (3767) 2000.
- [86] X. Wei, X. Zhou, K. Wu, Y. Chen, *Cryst. Eng. Comm.* **13** (1328) 2011.
- [87] S. Zhou, M. Wen, N. Wang, Q. Wu, Q. Wu, L. Cheng, *J. Mater. Chem.* **22** (16858) 2012.
- [88] N. Chakroune, G. Viau, C. Ricolleau, F. Fievet-Vincent, F. Fievet, *J. Mater. Chem.* **13** (312) 2003.
- [89] X. T. Tang, G. C. Wang, M. Shima, *J. Magn. Magn. Mater.* **309** (188) 2007.
- [90] Y. Xia, Y. Xiong, B. Lim, S. E. Skrabalak, *Angew. Chem. Int. Ed.* **48** (60) 2009.
- [91] M. Cheng, M. Wen, S. Zhou, Q. Wu, B. Sun, *Inorg. Chem.* **51** (1495) 2012.
- [92] L. Li, Y. Cheah, Y. Ko, P. Teh, G. Wee, C. Wong, S. Peng, M. Srinivasan, *J. Mater. Chem. A* **1** (10935) 2013.
- [93] A. I. Kirkland, D. A. Jefferson, D. G. Duff, P. P. Edwards, I. Gameson, B. F. G. Johnson, D. J. Smith, *Proc. R. Soc. London, Ser. A* **440** (589) 1993.
- [94] Y. Xiong, H. Cai, Y. Yin, Y. Xia, *Chem. Phys. Lett.* **440** (273) 2007.
- [95] X. Yan, H. Liu, K. Yong Liew, *J. Mater. Chem.* **11** (3387) 2001.
- [96] C. M. Liu, L. Guo, R. M. Wang, Y. Deng, H. B. Xu, S. H. Yang, *Chem. Comm.* **23** (2726) 2004.
- [97] Y. C. Zhu, H. G. Zheng, Q. Yang, A. L. Pan, Z. P. Yang and Y. T. Qian, *J. Crys. Growth* **260** (427) 2004.
- [98] A. E. Berkowitz, W. J. Schuele, P. J. Flanders, *J. Appl. Phys.* **39** (1261) 1968.
- [99] J. P. Chen, C. M. Sorensen, K. J. Klabunde, G. C. Hadjipanayis, E. Devlin, A. Kostikas, *Phys. Rev. B: Condens. Matter* **54** (9288) 1996.
- [100] J. M. D. Coey, *Phys. Rev. Lett.* **27** (1140) 1971.

- [101] A. E. Berkowitz, J. L. Walter, *Mater. Sci. Eng.* **55** (275) 1982.
- [102] F. Bossard, M. Moan, T. Aubry, *J. Rheol.* **51** (1253) 2007.
- [103] X. Wei, X. Zhou, K. Wu, Y. Chen, *Cryst. Eng. Comm.* **13** (1328) 2011.
- [104] S. Bai, X. Shen, G. Zhu, M. Li, H. Xi, K. Chen, *ACS Appl. Mater. Interfaces* **4** (2378) 2012.
- [105] K. Shah, J. Oh, S. Choi, R. V. Upadhyay, *J. Appl. Phys.* **114** (213904) 2013.
- [106] M. T. López-López, A. Gómez-Ramírez, L. Rodríguez-Arco, J. D. G. Durán, L. Iskakova, A. Zubarev, *Langmuir* **28** (6232) 2012.
- [107] C. R. Lin, C. L. Yeh, S. Z. Lu, I. S. Lyubutin, S. C. Wang, I. P. Suzdalev, *Nanotechnology* **21** (235603) 2010.
- [108] L. J. Felicia, J. Philip, *Langmuir* **29** (110) 2013.
- [109] J. S. Choi, B. J. Park, M. S. Cho, H. J. Choi, *J. Magn. Magn. Mater.* **304** (e374) 2006.
- [110] I. Arief, P. K. Mukhopadhyay, *J. Magn. Magn. Mater.* **360** (104) 2014.
- [111] X. Gong, Y. Xu, S. Xuan, C. Guo, L. Zong, *J. Rheol.* **56** (1375) 2012.
- [112] T. G. Mason, D. A. Weitz, *Phys. Rev. Lett.* **75** (2770) 1995.
- [113] P. Kuzhir, A. Gómez-Ramírez, M. T. López-López, G. Bossis, A. Zubarev, *J. Nonnewton. Fluid Mech.* **166** (373) 2011.
- [114] H. Sahin, X. Wang, F. Gordaninejad, *J. Intel. Mat. Syst. Str.* **20** (2215) 2009.
- [115] M. Ocalan, G. H. McKinley, *Rheol. Acta* **52** (623) 2013.
- [116] D. R. Lide (ed.), *CRC Handbook of Chemistry and Physics (Internet Version)*, CRC Press, Boca Raton, FL (12/219) 2005.
- [117] S. G. Sherman, L. A. Powell, A. C. Becnel, N. M. Wereley, *J. Appl. Phys.* **117** (17C751) 2015.
- [118] W. H. Li, G. Chen, S. H. Yeo, H. Du, *Int. J. Mod. Phys. B* **16** (2725) 2002.
- [119] J. Crangle, G. M. Goodman, *Proc. R. Soc. London, Ser. A* **321** (477) 1971.
- [120] D. Susan-Resiga, D. Bica, L. Vékás, *J. Magn. Magn. Mater.* **322** (3166) 2010.
- [121] J. P. Rich, P. S. Doyle, G. H. McKinley, *Rheol. Acta* **51** (579) 2012.
- [122] P. Fischer, H. Rehage, *Langmuir* **13** (7012) 1997.
- [123] H. Wu, C. Qian, Y. Cao, P. Cao, W. Li, X. Zhang, X. Wei, *J. Phys. Chem. Solids* **71** (290) 2010.
- [124] M. van Schilfgaarde, I. A. Abrikosov, B. Johansson, *Nature* **46** (400) 1999.

- [125] R. Bolsoni, V. Drago, E. Lima Jr., *J. Metastable and Nanocryst. Mater.* **14** (51) 2002.
- [126] P. Scherrer, *Bestimmung der Grosse und der inneren Struktur von Kolloidteilchen mittels Rontgenstrahlen*, *Nachr Ges Wiss Gottingen* **26** (98) 1918.
- [127] F. N. Sayed, V. Polshettiwar, *Nature Scientific Reports* **5** (9733) 2015.
- [128] J. de Vicente, J. P. Segovia-Gutiérrez, E. Andablo-Reyes, F. Vereda, R. Hidalgo-Álvarez, *J. App. Phys.* **131** (194902) 2009.
- [129] A. R. Payne, *J. Appl. Polym. Sci.* **6** (57) 1962.
- [130] H. An, S. J. Picken, E. Mendes, *Polymer* **53** (4164e4170) 2012.
- [131] V. V. Sorokin, E. Ecker, G. V. Stepanov, M. Shamonin, G. J. Monkman, E.Y. Kramarenko, A. R. Khokhlov, *Soft Matter* **10** (8765) 2014.
- [132] F. Márquez, T. Campo, M. Cotto, R. Polanco, R. Roque, P. Fierro, J. M. Sanz, E. Elizalde, C. Morant, *Soft Nanoscience Letters* **1** (25) 2011.
- [133] T. Fujita, M. Chen, X. Wang, B. Xu, K. Inoke, K. Yamamoto, *J. App. Phys.* **101** (014323) 2007.
- [134] F. Márquez, T. Campo, M. Cotto, R. Polanco, R. Roque, P. Fierro, J. M. Sanz, E. Elizalde, C. Morant, *Soft Nanoscience Letters* **1** (25) 2011.
- [135] I. Arief, P. K. Mukhopadhyay, *J. Magn. Magn. Mater.* **372** (214) 2014.
- [136] G. Kraus, *J. Appl. Polym. Symp.* **39** (75) 1984.
- [137] G. Hubery, T. A. Vilgisy, G. Heinrich, *J. Phys.: Condens. Matter* **8** (L409) 1996.